# SUPPORTING SPACE DOMAIN AWARENESS THROUGH THE DEVELOPMENT AND ANALYSIS OF SPACE OBJECT DETECTION ALGORITHMS EMPLOYED BY GROUND-BASED TELESCOPES

THESIS

Connor A. Paw, Second Lieutenant, USAF

AFIT-ENG-MS-21-M-071

**DEPARTMENT OF THE AIR FORCE**
**AIR UNIVERSITY**

**AIR FORCE INSTITUTE OF TECHNOLOGY**

**Wright-Patterson Air Force Base, Ohio**

AFIT-ENG-MS-21-M-071

# SUPPORTING SPACE DOMAIN AWARENESS THROUGH THE DEVELOPMENT AND ANALYSIS OF SPACE OBJECT DETECTION ALGORITHMS EMPLOYED BY GROUND-BASED TELESCOPES

THESIS

Presented to the Faculty
Department of Electrical and Computer Engineering
Graduate School of Engineering and Management
Air Force Institute of Technology
Air University
Air Education and Training Command
In Partial Fulfillment of the Requirements for the
Degree of Master of Science in Electrical Engineering

Connor A. Paw, B.S.E.E
Second Lieutenant, USAF

March 2021

**DISTRIBUTION STATEMENT A.**
APPROVED FOR PUBLIC RELEASE; DISTRIBUTION UNLIMITED.

AFIT-ENG-MS-21-M-071

# SUPPORTING SPACE DOMAIN AWARENESS THROUGH THE DEVELOPMENT AND ANALYSIS OF SPACE OBJECT DETECTION ALGORITHMS EMPLOYED BY GROUND-BASED TELESCOPES

THESIS

Connor A. Paw, B.S.E.E.

Second Lieutenant, USAF

Committee Membership:

Dr. Stephen C. Cain
Chair

Maj David J. Becker, PhD
Member

Maj Tyler J. Hardy, PhD
Member

## Abstract

Detection algorithms are instrumental in maintaining space domain awareness, specifically in the observation, monitoring, and categorization of unknown space objects. State of the art detection algorithms utilize a matched filter or a spatial correlator on long exposure image data to make pixel-wise detection decisions. This thesis investigates the advantages and practical potential of two different post-processing detection algorithms that can be employed by ground-based telescopes. The first algorithm explored is based on a long exposure Fourier domain processing technique, while the second is centered around frame selection from a series of short exposure images.

The results of the experiments performed in this thesis ultimately showed that the Fourier point detector algorithm did outperform a traditional point detector algorithm but had significantly lower probability of detection across all false alarm rates when compared to a spatial correlator algorithm over a series of test scenarios.

The novel frame selection algorithm was found in the simulated experiment to outperform both the old frame selection algorithm and the spatial correlator in all testing environments at low false alarm rates. The experimental data results confirmed the increased performance of the new frame selection algorithm against its' counterparts.

# Acknowledgments

I would like to express my appreciation to my faculty advisor, Dr. Stephen Cain, for his guidance and support during this thesis effort. The wealth of knowledge and experience was invaluable. Additionally, I would like to thank my wife for all the encouragement she has provided me throughout the process.

Connor A. Paw

## Table of Contents

Page

## List of Figures

# List of Tables

## List of Acronyms

| | |
|---|---|
| **AFIT** | Air Force Institute of Technology |
| **AFSPACECOM** | Air Force Space Command |
| **AMOS** | Air Force Maui Optical Station |
| **BHT** | binary hypothesis test |
| **CCD** | charge-coupled device |
| **CDF** | cumulative distribution function |
| **DoD** | Department of Defense |
| **FOV** | field of view |
| **FPD** | Fourier point detector |
| **GEO** | geostationary Earth orbit |
| **GEODSS** | Ground-Based Electro-Optical Deep Space Surveillance |
| **CSpOC** | Combined Space Operations Center |
| **LINEAR** | Lincoln Near Earth Asteroid Research |
| **LROC** | logarithmic receiver operating characteristic |
| **LRT** | likelihood ratio test |
| **MHT** | multi-hypothesis test |
| **MIT** | Massachusetts Institute of Technology |
| **NASA** | National Aeronautics and Space Administration |
| **NEA** | near-Earth asteroid |
| **NEO** | near-Earth object |
| **OTF** | optical transfer function |

| | |
|---|---|
| **$P_D$** | probability of detection |
| **$P_{FA}$** | probability of false alarm |
| **PDF** | probability density function |
| **PMF** | probability mass function |
| **PSF** | point spread function |
| **ROC** | receiver operating characteristic |
| **SNR** | signal-to-noise ratio |
| **SDA** | Space Domain Awareness |
| **SSN** | Space Surveillance Network |
| **SST** | Space Surveillance Telescope |
| **U.S.** | United States |
| **USSF** | United States Space Force |
| **WISE** | Wide-field Infrared Survey Explorer |

# SUPPORTING SPACE DOMAIN AWARENESS THROUGH THE DEVELOPMENT AND ANALYSIS OF SPACE OBJECT DETECTION ALGORITHMS EMPLOYED BY GROUND-BASED TELESCOPES

## I. Introduction

### 1.1 Motivation

Reliable and effective operations in space are integral to the national security of the United States (U.S.) . According to the United States National Space Policy, an important goal is to "Develop, maintain, and use SSA information from commercial, civil, and national security sources in an open architecture data repository to detect, identify, and attribute actions in space that are inconsistent with the safety, stability, security, and the long-term sustainability of space activities..."[1]. Additionally, to emphasize the increasing importance of control in the space domain, the United States Space Force (USSF), formerly established as Air Force Space Command (AFSPACECOM), was established as its own department in December 2019 [2].

The ability to detect and track space objects is integral to the nation's ability to conduct effective operations in space. Numerous organizations have been tasked with space monitoring and detection-based missions, including AFSPACECOM, National Aeronautics and Space Administration (NASA), the Combined Space Operations Center (CSpOC), and other space organizations.

The National Aeronautics and Space Administration Authorization Act of 2010 reaffirmed a key mission of the organization's original mission – to pursue "detecting, tracking, cataloguing, and characterizing near-Earth asteroids and comets" [3, 4]. Throughout its history, NASA has been issued several U.S. Congressional mandates in the realm of near-Earth object (NEO) detection. Their original 1998 mandate of finding 90% of existing NEOs greater than 1km in diameter was completed and superseded by the 2005 NASA Authorization Act mandate to find and catalog 90% of NEOs "larger than 140m that are within close trajectory of Earth" with the help of the Department of Defense (DoD) and other organizations by the year 2020 [5, 6]. The latest NASA NEO program office data of the number of cataloged NEAs is seen in Figure 1 [7].

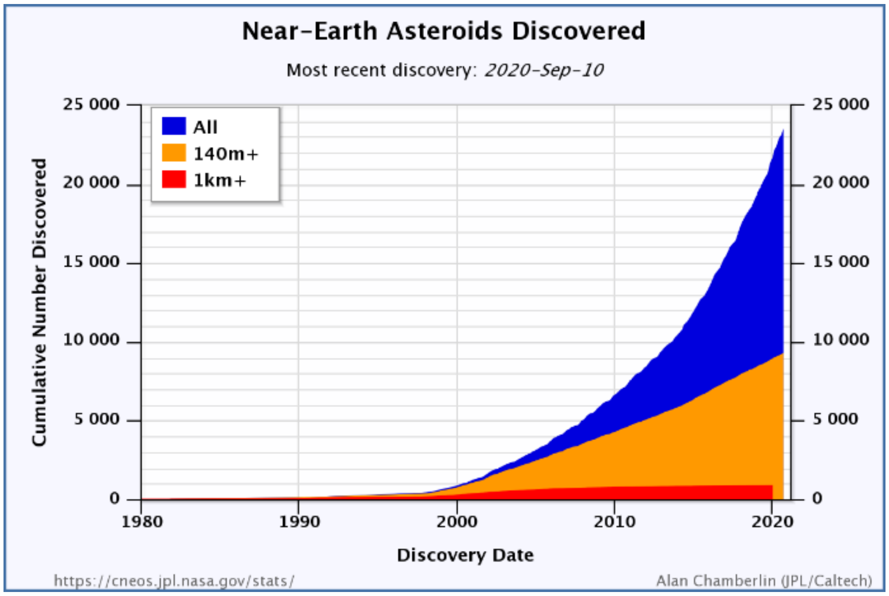

Figure 1. NEO program office number of cataloged NEAs

NASA has been able to make drastic revisions to their original inflated estimates of existing NEAs, which is due to their implementation of a telescope called the Wide-field Infrared Survey Explorer (WISE). These more accurate estimations of the NEA population ultimately led to the completion of the original Congressionally-mandated NEO detection mission. However, NASA has since sidelined their NEO mission and has only cataloged approximately 40% of NEOs greater than 140m – the “end of 2020” mandate deadline will need to be extended for completion. The data on the number of asteroids that NASA has cataloged, the number of asteroids NASA predicts are in orbit, and a comparison to their initial estimates pre-WISE launch is shown in Figure 2 [5].

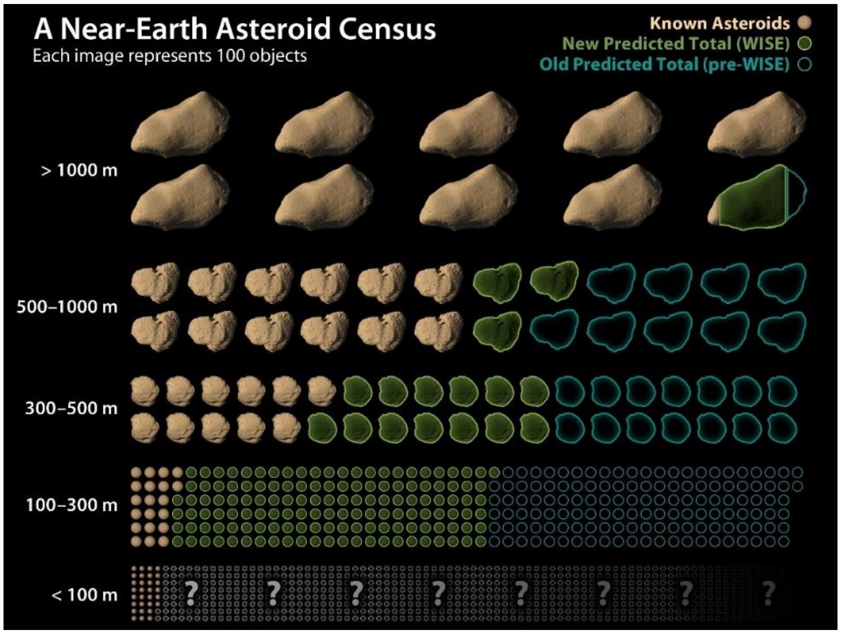

Figure 2. Known asteroids cataloged by NASA compared to population estimates before and after launch of WISE

Within the DoD specifically, the importance of detecting and tracking space objects including space debris and microsatellites is paramount due to the risk they constitute to existing space assets [8]. The JSpOC currently manages the tracking of known man-made objects in space. Many of these objects were originally found by the Space Surveillance Network (SSN), which is composed of a worldwide network of 30 civilian and military sensors dedicated to detecting and providing tracking information to other organizations such as JSpOC. The objects that JSpOC tracks and their relative distance to Earth, as well as the rise in their prevalence is shown in Figure 3 [9].

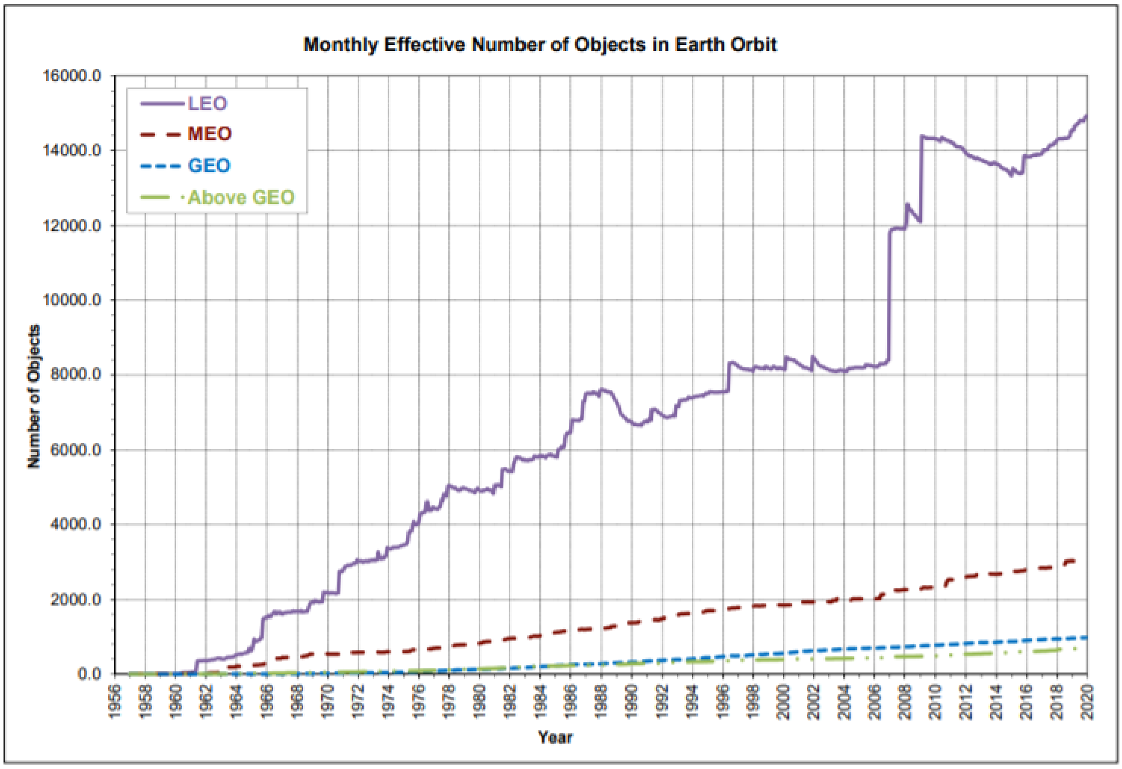

Figure 3. Objects tracked by JSpOC from 1956-2020 categorized by Earth orbit

In addition to the assets of JSpOC, the USSF, formerly AFSPACECOM, manages the Ground-Based Electro-Optical Deep Space Surveillance (GEODSS) sites which include the Space Surveillance Telescope (SST) located in Australia, the Air Force Maui Optical Station (AMOS) in Hawaii, and a site at Diego Garcia in the Indian Ocean [10]. These sites focus on gathering and processing data to further the space domain awareness (SDA) mission.

## 1.2 Research Goals and Objectives

The primary goal of this research is to improve existing ground-based telescopes' abilities to detect small or dim space objects. Due to the miniscule size of space objects when viewed from ground-based telescopes, they are essentially unresolvable points sources in the image captured by the CCD. When the objective is to look for smaller asteroids or objects, the intensity received by the telescope is likely to approach the level of background noise and become virtually indistinguishable without statistical analysis.

As will be further covered in Chapter II, current detection algorithms employed by ground-based telescopes with an SDA mission utilize a correlation-based approach on the spatial image received by the optical system's CCD array. The overall intent of this research is to improve the detection performance of current optical systems by analyzing multiple different detection algorithms and novel methodologies. The following research questions outline the emphases of the research in this thesis.

*1. Will a Fourier domain point detector, as opposed to a traditional spatial point detector, yield detection performance advantages when compared to correlation-based algorithms?*

*2. In detection scenarios where short exposure imaging is used, will frame selection increase the ability of detecting objects over a simple summation of multiple frames?*

*3. What variables or constraints should be explored to optimize this frame selection algorithm?*

The first research question examines a Fourier domain point source detector algorithm published in a previous dissertation to decide if the algorithm is viable when compared against currently employed correlator algorithms [11]. Research questions two and three address a frame selection algorithm which aims to beat the performance of a simple summed frame approach. Additionally, a key data distribution assumption in previous frame selection research is challenged.

## 1.3 Assumptions and Limitations

The following assumptions serve to manage the scope of this research.

- Space objects within the experimental and simulated images are considered unresolvable and are treated as point sources to the imaging system. Due to the optical aberrations from the atmosphere and telescope optics, the intensity of this point source is not limited to a single pixel but will likely be spread across multiple pixels.
- Background noise present in an image follows a Poisson distribution.
- Detection decisions are made using a single frame of long exposure data or multiple summed short exposure images taken in the same time frame as a single long exposure image. Algorithms that utilize multiple long exposure frames of

data to reduce the number of false alarms, such as streak or blur detection, are not studied in this research.

- In a current daylight imaging scenario, an imaging system's CCD pixel wells are limited in depth and require short exposure imaging to circumvent saturation.
- A common metric for object detection relies on crafting receiver operating characteristic (ROC) curves based on a Gaussian assumption for the data. This method is not utilized unless the histogram of the data truly follows a normal distribution.

## 1.4 Document Outline

This thesis is organized into five chapters that contain the necessary background information to understand the motivation and methods behind this research and address the goals and questions found in Section 1.2.

A literature review, along with a primer for the key concepts and methodologies behind space object detection algorithms are contained in Chapter II. This chapter delves into past and present object detection algorithms, as well as the theory behind and formulation of the atmospheric turbulence, noise sources, and optical models used in this research.

Chapter III reconstructs a Fourier point detector (FPD) algorithm that was derived and tested in a recent dissertation. This chapter compares the true performance of this algorithm against two traditional space detection algorithms, a spatial matched filter or correlator and a spatial point detector, in order to determine its viability.

In Chapter IV, a novel frame selection algorithm is utilized to improve the detection performance of the spatial correlator through statistical analysis and outlier reduction of the multiple short exposure frames that comprise a single long exposure image. The performance of this new algorithm is compared to two other algorithms: a previously employed frame selection algorithm [11], and a standard summed frames algorithm. The prior frame selection algorithm operated under the assumption that the detection algorithm data followed a Gaussian distribution. A portion of this chapter investigates the limitations and potential overestimations of performance that can arise from this fallible assumption.

Chapter V serves as a conclusion to this thesis that summarizes each research goal, the impact of the research, and continuation efforts that can be tackled to further this research.

# II. Background and Literature Review

## 2.1 Chapter Overview

This chapter introduces the key concepts and methodologies related to the research explored in this thesis. An overview of the current space object detection environment is discussed, along with the relevance of improving object detection algorithms. This chapter delves into past and present object detection techniques used by the SDA community, as well as the theory behind and formulation of the algorithms relevant to this research. The final section of this chapter reviews the atmospheric turbulence, noise sources, and optical models used in this research, and the effects these have on the imaging system.

## 2.2 Space Object Detection Basis

There exist two major classes of space objects: naturally occurring objects such as asteroids, or man-made objects such as satellites or debris. There are intrinsic differences in the characteristics of these objects such as the size, shape, and reflectivity that affect the ability to detect and categorize them. One common example of these physical differences is that objects with surfaces that have higher reflectivity will appear brighter in images. The location of an object relative to the telescope and the sun also affects its appearance in images. For most ground-based telescopes with a SDA detection mission focus, there is an assumption that is ordinarily true that all objects in the field of view (FOV) appear optically similar [11]. A detection system with a wide FOV, on the order of 3-6 degrees of the sky per collection, is used to image large sections of the sky [12].

Conversely, imaging systems designed for high resolution imaging of known objects have a much narrower FOV.

Astronomers and scientists have been observing the skies for hundreds of years to find naturally occurring NEOs, such as asteroids and comets. Early space object detection was performed through studies with rudimentary observatories and the human eye to notice the location change of visible objects within time increments. These searches continue, but the focus has more recently shifted to objects that may pose a threat to Earth.

### 2.2.1 Current Space Surveillance Practices

Relatively recent developments in optics, sensors such as low-noise and curved CCDs, along with improvements to detection algorithms fueled by cheaper and more complex computing power have led to considerable improvements in the ability to detect NEOs [11]. As discussed in Chapter I, there is also still the ongoing NEO detection mission assigned to NASA by the 2005 U.S. Congressional mandate.

Aside from naturally occurring objects, man-made objects pose the greatest risk to assets in space. These objects and debris in space are the product of decades of space exploration, infrastructure, and research. Included in these objects are discarded satellites, depleted space launch vehicles, and debris created from a handful of documented explosions and collisions of space objects [13]. Early space exploration and utilization largely overlooked the future complications of ubiquitous debris, but as the number of assets in space grew, the need to track and limit the creation of new debris became apparent. The density of the currently tracked man-made space debris in the GEO and LEO region is seen in Figure 4 from NASA’s Orbital Debris Program Office [14]. This debris poses many risks in the form of physical collisions and critical component damage to functional satellites.

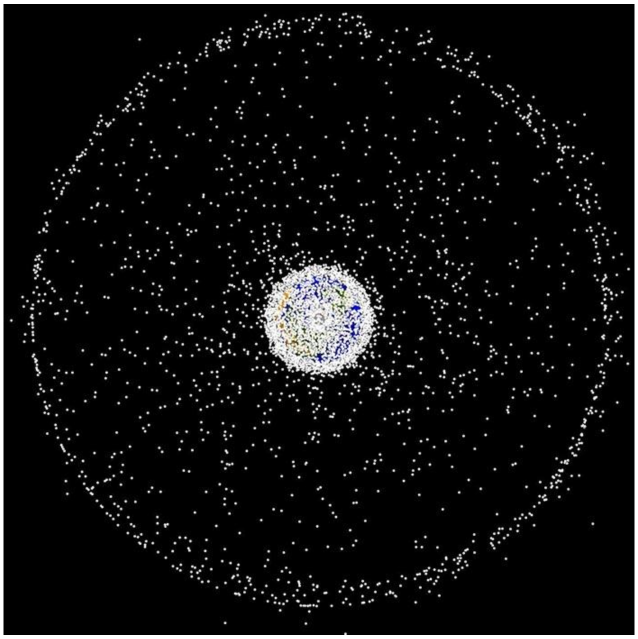

Figure 4. Debris population in the LEO and GEO regions from a vantage point above Earth’s north pole

Utilizing the SSN sensors, the JSpOC maintains the space catalog used to track objects and provide collision avoidance guidance. However, there are still many existing space objects that have either not been accounted for, or have not been discovered yet, and have resulted in unplanned collisions. The first known collision of man-made space objects occurred in 1991 between two retired Russian satellites, Cosmos 1934 and Cosmos 926 [9]. Nearly one-third of the cataloged orbital debris in the GEO region is a result of a combination of China’s intentional destruction of their Fengyun-1C weather satellite in 2007 and the accidental collision of American and Russian communication satellites in 2009. NASA estimated that the demolition of Fengyun-1C resulted in the creation of approximately 35,000 debris fragments larger than 1 cm, and it is postulated that the debris created by this event impacted and destroyed a Russian satellite in 2013 [15]. NASA predicts there are approximately 500,000 bits of debris that are larger than 1 cm, and 100 million pieces smaller than 1cm [15, 16]. If NASA's estimates are correct then there are many unaccounted for and therefore potentially hazardous objects present in Earth's orbit.

The pursuit to catalog new space objects involves multiple areas of research including imaging, processing, detecting, tracking and characterizing. The work in this thesis focuses on the post-processing of ground-based telescope images to detect space objects. This research is intended for use with the SSN sensors to conduct follow-up observations to establish tracking, characterize the objects, and catalog them.

### 2.2.2 Daylight Imaging

Traditional space imaging operations are limited to only night or dark twilight imaging. This is due to a combination of the higher background light and the more turbulent and highly variable atmosphere present during daylight conditions [17, 18]. The brighter background in daylight imaging also results in the CCD reaching saturation much faster. These conditions disallow long exposure imaging, limiting the sensor integration time to short exposure time frames of significantly less than 100ms [18]. Traditional nighttime space imaging greatly restricts the amount of telescope time available for operators to collect data for the detection mission. One of the greatest benefits of daylight imaging is the additional operating time. Under traditional night imaging, a NEO is detectable during terminator conditions, which are periods of a few hours most nights when an object is both illuminated by the sun and the telescope site is dark [17]. Developing effective daylight imaging methods would vastly increase the amount of telescope operation time and could have a major impact on various imaging and detection missions.

Smaller aperture telescopes have the capacity to image during twilight and even daylight conditions, but current detection algorithms are not adapted for low SNR, high background light data. Currently, the only techniques used for daylight conditions are forms of high-resolution speckle imaging, which capture many short exposure frames, average them together, and run the result through a deconvolution algorithm [19, 20, 21, 22, 23]. The purpose of these methods is primarily for increased space imaging resolution, not detection, since they are largely employed on telescopes with a limited FOV that are trained on already detected objects. A portion of this research tests algorithms in not only traditional nighttime imaging scenarios, but also twilight and daylight conditions to further the SDA mission by allowing for more telescope operation time.

### 2.3 Detection Algorithm Foundations and Techniques

Spacewatch, the first program devoted to detecting, tracking, and cataloging objects in space, was established in 1984 by the University of Arizona. This program marked the earliest use of a CCD array to actively survey the sky, which proved to be a monumental breakthrough for the astronomical community. Prior to this invention, photographic plates were the norm for imaging and object detection. The usage of CCDs allowed the program to develop the first software-based space object detection algorithms in 1990 [13].

Since the initial algorithm development, CCDs have allowed for the discovery of many smaller and fainter objects, in part due to the advancements in computer processing power and memory. Spacewatch served as the launching point for future research programs dedicated to the detection of faint space objects. To illustrate the progression of detection in the past several decades, Figure 5 depicts the latest data from NASA on the number of NEAs detected each year by each space survey platform [7].

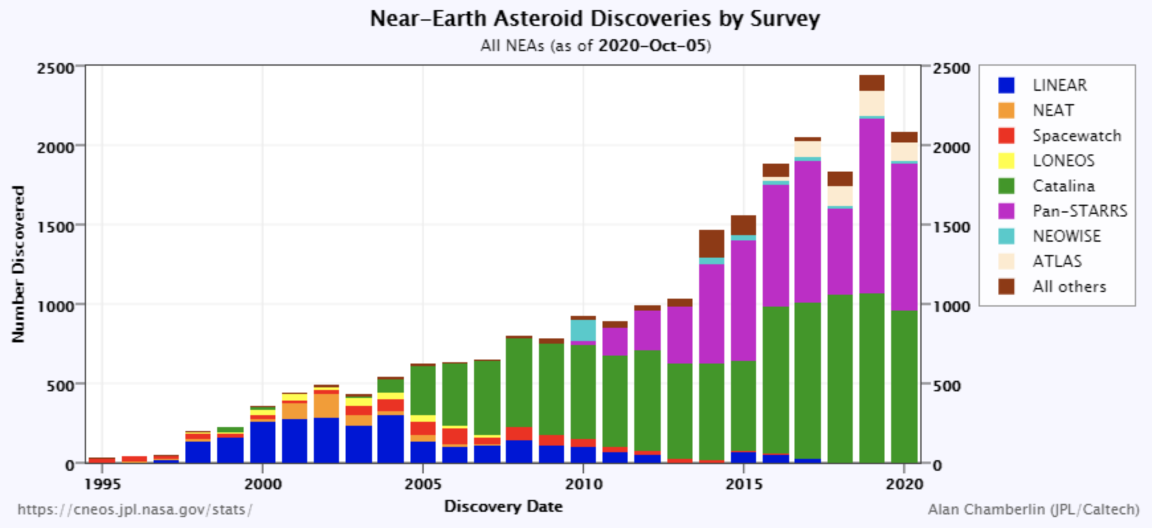

Figure 5. Number of detected NEAs by survey platform as of 5 Oct 2020

Each survey platform utilizes a detection method most suited to the capabilities of the sensor. Space object detection algorithms generally use single and multiple images obtained from ground-based telescopes. Many different types of detection techniques are broken down in Figure 6 according to frame number requirements and length of exposure.

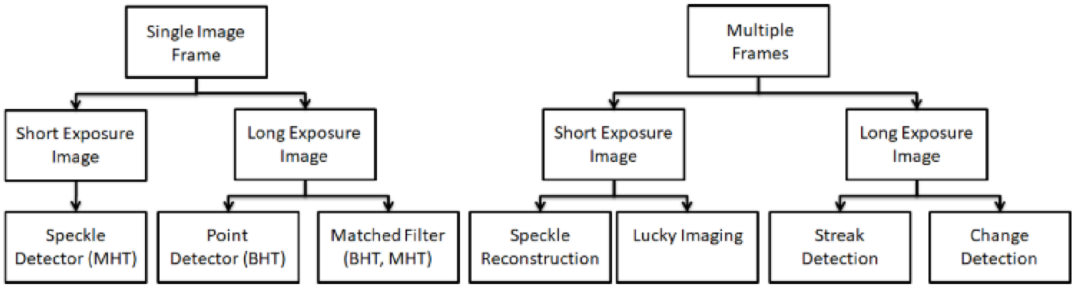

Figure 6. Generalized space surveillance techniques organized by frames and integration times [11]

In order to narrow the scope and justify the detection technique used in this research, some of the relevant assumptions listed in Section 1.3 are reiterated and explained in more detail below.

The first notable assumption is that space objects within the experimental and simulated images used in this research are considered unresolvable and are treated as point sources to the imaging system. The implication of this assumption is that the system cannot distinguish man-made objects from asteroids. This thesis is focused on space object detection, so the characterization of the detected objects is not a topic of interest. The idea behind this research is that after an object has been detected, the information can be passed on for multiple frame analysis techniques and further sensor observations. Many of the SSN platforms use multiple frames in their processing chain, but they begin with single frame detection, and follow-up with additional frames to confirm or reject that detection [11].

Following from the first assumption, detection decisions in this research are made using a single frame of long exposure data or multiple summed short exposure images taken in the same time frame as a single long exposure image. Algorithms that utilize multiple long exposure frames of data to reduce the number of false alarms, such as streak or blur detection, are not studied in this research. Referencing Figure 6, this assumption limits the possible algorithms that can be used to a point detector (including the FPD), a matched filter, speckle reconstruction, and lucky imaging. Lucky imaging techniques are not typically used for detection, but a modified lucky imaging detection algorithm was explored by Becker and results showed that a matched filter algorithm yielded notably higher detection performance [11]. In the interest of publishing novel research, lucky imaging techniques will not be reexamined in this thesis. Additionally, as briefly discussed in Section 2.3.5, speckle reconstruction is a high-resolution imaging technique, and is not designed for detection purposes. Despite its lack of applicability to this research, this technique will be further explored in Section 2.3.7 for completeness since it is a common short exposure imaging technique.

The next assumption that dictates some of the choices made in this research is related to the integration times used. The assumption is that in a daylight imaging scenario, an imaging system's CCD pixel wells are limited in depth and require short exposure imaging to circumvent saturation. This is true based on the current construction of CCD arrays. A portion of the simulated and experimental data in this research is performed in an environment with high background light levels, so in a truly accurate experiment based on current capabilities, long exposure integration times would saturate the CCD pixel wells.

The reassessment of the FPD in Chapter III uses a single long exposure data frame to analyze the detection performance. Similarly, the frame selection algorithm explored in Chapter IV utilizes multiple short exposure frames with an integration time between 10 and 25ms, which are summed to form a single long exposure data frame. For reference, long exposure integration times are defined as greater than 100ms by Goodman [24]. The short integration time is needed due to the high background light conditions present in a daylight imaging environment. The integration time in both scenarios is not long enough for objects to form streaks, therefore the images are optimized for point source detection.

Having narrowed the scope to only single frame long exposure images, there are two common detection methods discussed in literature and utilized by the various optical telescopes within the SSN: a point detector and a matched filter or correlator. Each of these are techniques are further described in Section 2.3.2, and Section 2.3.3, respectively, along with the FPD, a more recent offshoot of the point detector, in Section 2.3.4. Section 2.3.5 discusses a predecessor to the new frame selection algorithm in Chapter IV of this thesis. Some foundational concepts required to understand the derivation, utility, and analysis of these algorithms are included in Sections 2.3.1 and 2.3.6. Lastly, a few short exposure imaging techniques are discussed in Section 2.3.7. Although these short exposure imaging techniques are not the most effective for object detection purposes, they have been included for thoroughness.

### 2.3.1 Likelihood Ratio Test (LRT)

A LRT provides the foundation for each space object detection algorithm examined in this thesis. LRTs are utilized to build a binary mask which indicates pixels where an object is detected [25, 26, 27]. Using a ratio and thresholding, the LRT decides whether there is an object present in the data. This process, outlined in Figure 7, was determined by the developers of the SST and Lincoln Near Earth Asteroid Research (LINEAR) algorithm [8].

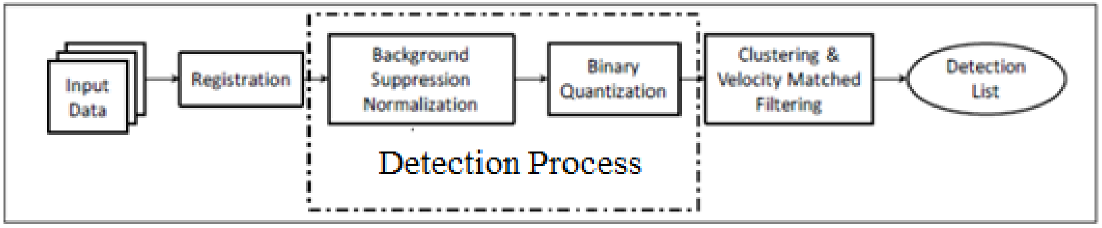

Figure 7. LINEAR & SST system detection diagram [26]

A generic LRT, $\Lambda$, with an equal cost, equal prior model, is defined as a ratio of joint conditional probabilities on the received data, *d(x, y)*, given each hypothesis, $H_1$ and $H_0$ [26].

$$\Lambda = \frac{P(d(x-x_0, y-y_0))\forall(x,y)\in[1,N] \mid H_1}{P(d(x-x_0, y-y_0))\forall(x,y)\in[1,N] \mid H_0} \underset{H_0}{\overset{H_1}{\gtrless}} \tau \tag{1}$$

In Equation (1), $x$ and $y$ are the possible pixel locations, $x_0$ and $y_0$ are the pixel coordinates that are currently being tested among all the pixel locations $(x, y)$, and $N$ is the number of pixels in each dimension of the windowed image. The two joint probabilities of the data in the LRT are conditioned on the $H_1$ (object present) and $H_0$ (object absent) hypotheses, which is when the data, $d$, contains and does not contain an object at the specific pixel coordinate $(x_0, y_0)$, respectively.

An object is detected when the ratio of the conditional probabilities in Equation (1) yields a value greater than the threshold, $\tau$. Inversely, a ratio of less than $\tau$ indicates there is no object present at the tested pixel. Space object detection methods have conventionally employed a LRT combined with a binary hypothesis test (BHT). A BHT indicates that the result will be chosen between two different outcomes: $H_1$, when an object is present, or $H_0$, when there is no object present.

A multi-hypothesis test (MHT) approach has been explored by Zingarelli and Hardy at the Air Force Institute of Technology (AFIT) [25, 26]. This approach, which essentially aims to increase the $P_D$ (probability of detection) by examining the effects of sub-pixels shifts in the point spread function (PSF), can increase performance under select detection scenarios. The results of these studies revealed that a MHT yielded increased detection performance over a BHT when multiple PSF variants based on sub-pixel shifts were tested for each coordinate [28].

LRT algorithm performance is determined by the $P_D$ and $P_{FA}$ (probability of false alarm), which are discussed in Section 2.3.1. Adjusting the $P_{FA}$ changes the threshold value in the LRT, $\tau$, and can be modified to meet the task and resource constraints. Generally, the $P_{FA}$ is assigned a low value in the range of $10^{-9}$ so the number of spurious detections is kept to a minimum.

### 2.3.2 Point Detector

One of the earlier efforts to advance object detection algorithms was spearheaded by the LINEAR program in 1995. Their research produced an algorithm that utilizes images gathered from a ground-based electro-optics telescope to detect objects with a BHT spatial point detector [29]. The SST and other SSN assets currently employ a modified version of LINEAR's point detector.

The preprocessing steps of the LINEAR and SST detection process involve reading multiple frames of data, registering this data using known reference objects within the frame, and averaging to a single frame. These steps remove pointing error associated with the imaging system, thereby increasing the overall SNR of the image data.

The point detection algorithm creates a binary mask that identifies pixels with an SNR that exceeds a predetermined threshold. The SNR of the point detector is calculated by examining the intensity at a pixel, *d(x - x0, y - y0)*, subtracting the background, *B*, and dividing by the standard deviation of the noise, $\sigma_n$, as shown in Equation (2). This detection method hinges on the data following a Gaussian distribution. With this assumption in place, the result of the calculation is the number of standard deviations that the pixel intensity is away from the background intensity of the received image.

$$SNR_{PD} = \frac{(d(x - x_0, y - y_0) - B)}{\sigma_n} \underset{H_0}{\overset{H_1}{\gtrless}} \tau \tag{2}$$

In Equation (2), B is the background intensity present in the image, $\sigma_n$ represents the localized standard of the background noise, and τ is the set threshold that is used in conjunction with the LRT to determine if there is an object detected. The background value is calculated as the median of all *N* pixels surrounding the $(x_0, y_0)$ pixel coordinate, as shown in Equation (3).

$$B = median(d(x - x_0, y - y_0)) \forall (x, y) \in [1 : N]) \tag{3}$$

Using the median rather than another method of finding an average background level is advantageous because it will automatically reject outliers in the image that may exist due to the presence of other known objects or noise spikes [11, 30]. The localized standard deviation of the background noise is calculated using Equation (4).

$$\sigma_n = \sqrt{\frac{\sum_{x=1}^{N}\sum_{y=1}^{N} d^2(x-x_0, y-y_0)}{N^2} - B^2} \tag{4}$$

The SST program primarily uses a value of six as the detection threshold, $\tau$, which roughly equates to a $P_{FA} \approx 10^{-9}$. A single frame in the SST imaging system's CCD array is 6,144 x 4,086 pixels, containing over 25 million pixels, so this extremely low $P_{FA}$ is justified [8]. To meet or exceed this high threshold, the intensity from the space object would ideally be contained within a single pixel. When the PSF or size of the object is spread across multiple pixels on the CCD detector, the SNR decreases, and the likelihood of exceeding the detection threshold is greatly diminished. This is the case for many telescopes, including the SST.

### 2.3.3 Matched Filter

The matched filter, also known as the spatial correlator, is an algorithm that involves utilizing correlation to achieve greater detection performance in space object searches than the spatial point detector algorithm discussed in the preceding section [29]. The matched filter algorithm correlates (or "matches") the observed image data with the expected PSF. The size and shape of the PSF is needed for reliable results from the matched filter. For a long exposure PSF, this can generally be determined from measurable statistical parameters of the atmosphere using methods discussed in Section 2.4.3.

Assuming a Gaussian distribution for CCD camera noise, a matched filter detection program known as SExtractor was created [30]. Variants of the original

SExtractor software is still in use by multiple SDA programs, and is defined by Equation (5).

$$SNR_{MF} = \frac{\sum_{x=1}^{N}\sum_{y=1}^{N}(d(x,y)-B)h_L(x-x_0,y-y_0)}{\sigma_n\sqrt{\sum_{x=1}^{N}\sum_{y=1}^{N}{h_L}^2(x,y)}} \underset{H_0}{\overset{H_1}{\gtrless}} \tau \tag{5}$$

In Equation (5), $d(x, y)$ refers to a single image frame, $(x_0, y_0)$ is the current pixel location being tested, $N$ is the square window size in pixels along each side, $h_L(x, y)$ is the expected long exposure PSF, $B$ is the median background photon noise level, and $\sigma_n$ is the standard deviation of the noise. This equation was derived by constructing an LRT, and it compares the result to a threshold, $\tau$, to determine whether it falls into the $H_1$ or $H_0$ category.

The matched filter is highly dependent on knowledge of the long exposure PSF, $h_L(x, y)$, since the PSF is the known input that is correlated with the received image data to determine the degree to which they match. As previously mentioned, many SDA ground-based telescopes improperly sample their image data, resulting in an asymmetric PSF in the CCD plane, which decreases the performance of the matched filter algorithm [28].

### 2.3.4 Fourier Point Detector (FPD)

The FPD is an object detection algorithm derived by Becker that stems from the idea that analyzing the frequency domain information of a spatial image may result in increased detection performance [11]. This algorithm was designed to be utilized in a long exposure scenario, and the significance of its derivation, as explored in Becker’s research, is that there is no reliance on the PSF of the optical system.

In order to realize the FPD, the background must be subtracted from the spatial data as a pre-processing setup, as shown in Equation (6)

$$d'(x,y) \triangleq d(x,y) - B \tag{6}$$

The background-removed data, *d'(x, y)*, is then Fourier transformed, as defined in Equation (7), to develop a statistical model in the frequency domain.

$$D(f_x, f_y) \triangleq \Im\{d'(x,y)\} = \frac{1}{N}\sum_{x=1}^{N}\sum_{y=1}^{N} d'(x,y) e^{-j\frac{2\pi}{N}(xf_x + yf_y)} \tag{7}$$

In this equation, $D(f_x, f_y)$ is defined as the Fourier transform of the background-removed data, *N* is the number of pixels in the window and $f_x$ and $f_y$ are the spatial frequency locations in the transformed image. The form of Equation (7) is similar to a random phasor sum which consists of a random amplitude and phase as defined by Goodman [31].

The real and imaginary components of the Fourier transformed data can be divided using Euler's formula as defined in Equations (8) and (9).

$$D_r(f_x, f_y) \triangleq \mathrm{Re}\{D(f_x, f_y)\} = \frac{1}{N}\sum_{x=1}^{N}\sum_{y=1}^{N} d'(x,y)\cos\left(\frac{2\pi}{N}(xf_x + yf_y)\right) \tag{8}$$

$$D_i(f_x, f_y) \triangleq \mathrm{Im}\{D(f_x, f_y)\} = \frac{1}{N}\sum_{x=1}^{N}\sum_{y=1}^{N} d'(x,y)\sin\left(\frac{2\pi}{N}(xf_x + yf_y)\right) \tag{9}$$

The real component is used in this algorithm's development since long exposure PSFs are on average are real and symmetric, which means that the Fourier transform of the object is contained only in the real component. The imaginary component theoretically contains only noise and contributes no other useful information.

For a large frame size, separated data should be approximately Gaussian distributed due to the central limit theorem. Working with the real component of the Fourier transformed data, Becker derives the Fourier domain LRT as shown in Equation (10) [11].

$$\Lambda = \frac{P(D_r(f_x, f_y) \mid H_1)}{P(D_r(f_x, f_y) \mid H_0)} \underset{H_0}{\overset{H_1}{\gtrless}} \tau \tag{10}$$

In this equation, the conditional PDFs are Gaussian random variables with some mean and variance. In order to test the data against the derived LRT, the data is isolated and compared that to a threshold value, as shown in Equations (11) and (12) [11].

$$D_r(f_x, f_y) \underset{H_0}{\overset{H_1}{\gtrless}} \frac{\theta H(f_x, f_y)}{2} \tag{11}$$

$$\frac{\theta H(f_x, f_y)}{2} \triangleq \tau \tag{12}$$

The term on the right-hand side of Equation (12) is defined as the threshold value, $\tau$. Overall, this is a simple BHT comparing the real component at an individual pixel next to the DC component of the Fourier transformed telescope data to a threshold. Predefining a simple threshold value allows the $P_{FA}$ to be set at the desired level based on the threshold. The viability of this algorithm is reexplored against a BHT matched filter algorithm to determine if it should be further developed.

### 2.3.5 Basic Frame Selector

The idea of a frame selection algorithm of this nature was first explored by Becker in his dissertation [11]. The foundation lies in a matched filter algorithm, as described in Section 2.3.3. The research develops 10 short exposure image frames with a simulated faint source in the center pixel. These sources are designed to be statistically accurate according to optical and atmospheric aberrations. The individual image frames are summed together to simulate a single long exposure image and the result is supplied to a matched filter algorithm.

The key focus of the work delves into the potential detection performance increases possible from utilizing only a subset of the total frames and rerunning the algorithm. This frame selection algorithm performs recursively, first removing one frame individually, testing the correlation of the simulated summed PSF against the expected PSF, and ranking the 10 frames by the calculated correlation coefficient when they are removed. Assuming the removal of a frame increases the correlation, more frames are continuously removed using the same technique until the correlation does not improve.

To analyze the $P_D$ and $P_{FA}$ and compare performance against the baseline matched filter algorithm, a Gaussian assumption is made for the data, and a ROC curve is plotted. The methodology behind this will be discussed in the following section. Unfortunately, upon reexamination of this work, the data appears to deviate from a normal distribution, making the Gaussian-assumed ROC curve invalid. This faulty assumption will be further explained later in this thesis, as it serves as the starting point for the new frame selector algorithm pursued in Chapter IV.

### 2.3.6 Algorithm Comparison Metric

For this research, detection and false alarm rates will be compared in order to evaluate the performance of each different space object detection algorithm. This is a common metric used in numerous SDA-related studies [11, 25, 27]. The detection rate, $P_D$, is the probability that an object is detected when an object truly exists at the specified test location. The false alarm rate, $P_{FA}$, is the probability that the algorithm erroneously detects an object where no object exists. A receiver operating characteristic (ROC) curve is used to plot of the probability of detection versus the probability of false alarm [26].

In this research, the algorithms implemented in software make the detection decisions, and the employment of a ROC curve allows the performance to be tested at a desired range of threshold values, $\tau$. The advantage of the ROC curve comparison is that it allows detection algorithms to be compared independent of a predefined threshold value.

In order to implement a ROC curve, the $P_D$ and $P_{FA}$ for the desired threshold range are plotted on a linear-linear axis. To capture the results of algorithms at very low false alarms rates, a semi-log plot is realized, which plots the base 10 log of the $P_{FA}$ data on the x-axis. This method is referred to by Becker as a semi-log receiver operating characteristic (LROC) curve and will be used for this research in lieu of the traditional ROC curve due to its advantages at low $P_{FA}$ rates [11]. There are multiple methods that can be used, and assumptions that can be made to calculate the $P_D$ and $P_{FA}$, all of which are based on a large simulated data set of separate $H_1$ and $H_0$ data. A few of these methods are detailed in the following subsections, along with their benefits and limitations.

### *Gaussian ROC*

The approach used to produce an LROC curve for many of the algorithms discussed in this thesis, including the basic frame selector algorithm discussed in Section 2.3.5, requires that the image data follows a Gaussian distribution. The SNR of each data set is computed using their respective algorithm methods, and with this reduced sample of data points, the mean and variance of the SNR can be found. Using a Gaussian cumulative distribution function (CDF) with the calculated SNR mean and variance, the $P_D$ and $P_{FA}$ can be calculated using Equations (13) and (14) with the $H_1$ and $H_0$ data, respectively, since the noise is also Gaussian distributed [26].

$$P_D = \int_{\tau}^{\infty} \frac{e^{\frac{-(\Lambda-\mu_\Lambda)^2}{2\sigma_\Lambda^2}}}{\sqrt{2\pi\sigma_\Lambda^2}} d\Lambda \tag{13}$$

$$P_{FA} = \int_{\tau}^{\infty} \frac{e^{\frac{-(\Lambda-\mu_\Lambda)^2}{2\sigma_\Lambda^2}}}{\sqrt{2\pi\sigma_\Lambda^2}} d\Lambda \tag{14}$$

In Equation (14), $\mu_\Lambda$ and $\sigma^2_\Lambda$ represent the mean and the variance, respectively, of the LRT outputs from the 1,000 trials performed. The LROC curve plots the calculated $P_D$ and $P_{FA}$ for both algorithms across their separate selected threshold values to show the performance of the two algorithms across numerous false alarm rates.

***True ROC***

The method behind generating a "true" ROC curve, or LROC curve, is the same as the Gaussian assumption, aside from the calculation of the $P_D$ and $P_{FA}$ values. The true ROC involves an exact measurement of the $P_D$ and $P_{FA}$, rather than the estimation based on the mean and variance of the data that occurs for the Gaussian case. For example, if there are 1,000 image frames generated for both the $H_1$ and $H_0$ cases, then the $P_D$ is calculated as the number of detections out of the 1,000 $H_1$ frames, and the $P_{FA}$ is the number of spurious detections in the 1,000 $H_0$ frames. These values are computed across a discrete number of thresholds, and the result is plotted as the ROC curve. The major limitation of this method lies in the data generation. In the 1,000-frame example, the lowest $P_{FA}$ that can be observed is $10^{-3}$, which is too high for most SDA mission requirements. To be able to generate a LROC curve that extended to a $P_{FA}$ of $10^{-9}$, one billion frames would need to be generated, which would break all time and resource constraints of our project timeline. Because of the exorbitant computing power and time needed, the alternative of a Gaussian assumption for the calculation of the $P_D$ and $P_{FA}$ is widely accepted, supposing that the data indeed follows a normal distribution.

### 2.3.7 Short Exposure Imaging Techniques

In ground-based space imaging, atmospheric turbulence induces random phase errors in the light during the propagation from the source to the detector. During short exposure image gathering, the limited integration times combined with these random phase fluctuations result in scintillation or speckle at the receiver. However, there are some benefits to short exposure imaging that researchers have been able to utilize to improve detection and imaging. One advantage is that the long exposure atmospheric optical transfer function (OTF) does not maintain high spatial frequency content which limits the resolution of imaging through turbulence. Additionally, short exposure imaging removes the uncertainties in multiple frame image registration when viewing the intensity. This is due to the Fourier shift theorem, which states that a registration error or tilt in the image is the result of a phase shift in the Fourier domain. By viewing the magnitude of the Fourier transformed image, the spatial tilt error has theoretically been removed [24]. There are a few common documented imaging techniques that take advantage of these benefits that accompany short exposure imaging. These methods are briefly discussed in the following subsections.

### *Speckle Detection and Interferometry*

Speckle imaging and interferometry entails gathering typically between 10 and multiple thousand short exposure images and analyzing or combining them to achieve higher resolution images [18, 32]. Fortunately, hundreds of short exposure frames can be captured in same amount of time as a single long exposure frame. A speckle interferometry technique has been implemented at the AMOS telescope to improve the resolution and imaging capability of their 1.6 and 3.5-meter ground-based telescopes. This technique converts short exposure scintillate image data to the Fourier domain to extract the magnitude and phase information and improve the resolution to near the system’s diffraction limit.

Space object detection with short exposure images dominated by scintillation has been explored by Cain and Hardy [33, 34]. Their research involved constructing a LRT based on the probability distribution of the intensity fluctuations present in the image frames.

The PSF in short exposure cases will have atmospheric tilt that necessitates the use of a MHT to accurately detect objects in the frame. Preliminary research on this method has demonstrated, under select conditions, the potential to increase detection performance against the same space object in a long exposure scenario [25, 26, 35].

### *Lucky Imaging*

Lucky imaging is another similar short exposure frame selection imaging technique within the astronomical community that is used predominantly for image reconstruction [36, 37]. The most common application of this method involves taking thousands of short exposure images of the same known object, selecting a predetermined percentage of them, and combining them to craft an improved, high-resolution image. The ranking to determine which frames to accept is typically based on the Strehl ratio, which relates to the extent of phase aberrations from turbulence present in the image. This method requires viewing an object with a precise known location, or at a minimum a guide star to measure the quality of the image. Due to this constraint, the main function of this method is to improve the resolution of images containing a clearly visible object. In a blind scan and survey detection method with no apparent object, it becomes difficult to register and combine frames while avoiding registration errors due to noise spikes in the data [11]. A detection algorithm version of lucky imaging was implemented by Becker but was ultimately found to not perform as well as a spatial correlator algorithm for the purpose of object detection. Therefore, this technique will not be pursued further in this research.

## 2.4 Optical Effects Modeling

Optical aberrations are anomalies that occur in optical systems that cause light to spread out into a region of space, or converge into multiple focal points, instead of converging to a single focal point. There are numerous causes of aberrations, including mismatched phase/lens transformation, defects in the optical surfaces, and atmospheric aberrations. The effect of aberrations without the appropriate correction is typically a blurry, or distorted image in the receiver plane. To properly model this system, four models are needed: an imaging system model, a telescope model, an atmospheric model, and a noise model.

### 2.4.1 Imaging System Model

The primary function of modern telescopes is to capture the intensity from distant objects and map them as an image to the CCD detector array of the system. This process is typically modeled with a Rayleigh-Sommerfeld propagation, which is derived directly from Maxwell's equations and describes the travel of electromagnetic waves from one emitting object to a detector [24]. In this research, the propagation distance between the detector and the space objects is adequately large to instead utilize a Fraunhofer propagation, which is far less computationally complex. This procedure is known as Fourier optics, and the process of capturing and mapping the intensity from objects can be performed with a convolution between the object and the PSF, as shown in Equation (15) [24].

$$d(x,y) = \int_{-\infty}^{\infty}\int_{-\infty}^{\infty} o(u,v)h(x-u,y-v)\,du\,dv \tag{15}$$

In Equation (15), *d(x, y)* is the data of the captured image at the pixel coordinate *(x, y)* in the detector plane, *u* and *v* are pixels in the object plane, *h(x, y)* represents the PSF, and *o(u, v)* is a point source object.

As previously discussed in this chapter as well as in Chapter I, a key assumption in this research is that every space object of interest is unresolvable and is therefore considered a point source, or spatial impulse at the detector. Therefore, because of the Dirac sifting property and the fact that telescopes can be modeled as linear shift invariant systems over small fields of view, the image mapped onto the detector when viewing a space object is equivalent to the PSF. As shown in Equation (16), the total PSF of the imaging system, $h(m)$, is determined with the atmospheric PSF, $H_{atm}(u_2)$, and optical system PSF, $H_{opt}(u_2)$, and is calculated as their combined inverse Fourier transform [24, 31]. The PSF and OTF are inverse Fourier pairs, and describe a system's spatial and frequency domain responses, respectively.

$$h(m) = \mathfrak{I}^{-1}\left\{H_{opt}(u_2)H_{atm}(u_2)\right\} \tag{16}$$

In this equation, $m$ is a corresponding $(x, y)$ coordinate, and $u_2$ is spatial frequency. It should be noted that due to their focal length, some SDA ground-based telescopes' ability to sample at or above Nyquist is hindered for long range imaging situations. For these situations, another term, $H_{pixel}(u_2)$, may need to be included in Equation (16) to accurately reproduce the long exposure PSF. The methodology behind determining these transfer functions are detailed in the following sections.

### 2.4.2 Telescope Optical System Model

The effects on the PSF of the system due to optical aberrations present in the telescope optics make up the optical system OTF, $H_{opt}(u_2)$. For Chapter III of this research, the telescope parameters from the HST's Faint Object Camera were used for simulation. The Faint Object Camera was a survey instrument installed on the HST until 2002 but remains a good example of a telescope primed for detection. Because this telescope was chosen, the "physical" optical aberrations are ignored for the cases of this report. The effects of atmospheric aberrations are still accounted for, as they are not determined by the physical characteristics of the lens. The reasoning behind this omission is due to the scope of this research, as well as the lack of measured coefficients to properly model the HST's current optical aberrations. Before the installation of COSTAR, the HST had many physical aberrations, especially from the spherical aberration, Zernike 11. These aberrations greatly hindered the HST from capturing quality images, so a study was performed to estimate the coefficients of the aberrations. However, the installation of COSTAR significantly negated the aberrations due to wave front error, making their exclusion in the study relatively inconsequential.

In Chapter IV of this research, which utilizes short exposure image gathering, the simulated telescope as well as the telescope used to capture the experimental image data both have a small aperture and focal length ($f_l$) . The telescope is advertised as nearly aberration-free, which is not unreasonable for a small optical system. The basic parameters of the two telescopes used in this research are shown in Table 1. In ideal simulations, more exact physical aberration coefficients would be accounted for, so the concepts behind modeling these physical aberrations are still discussed.

Table 1. Basic parameters for the telescopes used in this research [38]

| **Telescope** | **$f_l$ (m)** | **Aperture Diameter (m)** | **Obstruction Diameter (m)** |
|---|---|---|---|
| Small Aperture Telescope | 2 | 0.05 | N/A |
| HST Faint Object Camera | 230 | 2.4 | 0.66 |

Zernike polynomials are a useful tool for modeling aberrations, as their polynomials have the same form as many optical wave fronts. These polynomials form a complete orthogonal set of basis functions, given that the footprint of the surface or wave front is a circular region, as is the case with many optical systems, especially those involving lenses. In Equation (17), the $i$ denotes the index of the Zernike, where $C_i$ is the coefficient associated with the $i^{th}$ Zernike and $Z_i(u, v)$ is the $i^{th}$ Zernike polynomial [24].

$$\Theta(u,v) = \sum_i C_i Z_i(u,v) \tag{17}$$

In this research, each Zernike coefficient used to model the telescope aberrations are assigned values of 0, meaning the aberration surface of the simulation is a plane. Equation (18), which describes the creation of the pupil function, stems from the result of Equation (17).

A pupil function defines how light waves are affected upon transmission through an optical system. It is a complex function of the position in the aperture that indicates the relative change in amplitude and phase of the light waves.

$$P(u,v) = A(u,v)e^{i\Theta(u,v)} \tag{18}$$

In Equation (18), $u$ and $v$ represent spatial locations, $\Theta(u, v)$ describes the phase changes that capture the effects of all optical aberrations, and $A(u, v)$ is a function that defines the aperture, which is simply the opening through which light travels [24]. In this research, it is defined by the known size and shape of the HST and its obstruction for Chapter III, or the size of the smaller aperture telescope for Chapter IV. The $\Theta(u, v)$ term is equivalent to a plane in this realization, so in this case, the pupil function is equal to the aperture of the simulated telescope. The aperture functions for each telescope scenario in this research is shown in Figure 8 on a scale of pixels.

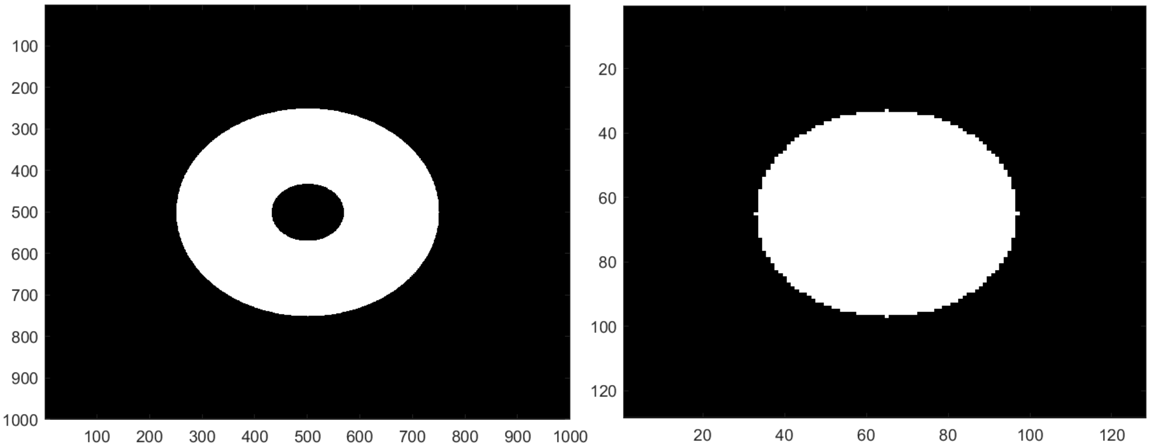

Figure 8. Aperture/pupil functions for HST telescope (left) and small aperture telescope (right)

The PSF is a focused system's response to a point source or impulse input (i.e. the impulse response) and is defined as the Fourier transform of the pupil function. The OTF is the Fourier transform of the PSF or, in calculation, the autocorrelation of the pupil function, and essentially specifies how different spatial frequencies are handled by the system. The calculations behind the PSF and OTF are described in Equations (19) and (20).

$$\tilde{h}(x,y) \triangleq \int_{-\infty}^{\infty}\int_{-\infty}^{\infty} P(u,v) e^{-\frac{j2\pi(xu+yv)}{\lambda z}} dudv \qquad (19)$$

In Equation (19), $u$, $v$, $x$, and $y$ denote spatial locations, $\lambda$ is the wavelength of the concerned light, and $z$ is the propagation distance. This equation is the formal definition of the field impulse response, $\tilde{h}(x,y)$, for an infinite aperture for the pupil function, $P(u, v)$, which in practical applications is impossible. For the purposes of simulation, the upper and lower bounds of the integral are replaced by the maximum and minimum $x$ and $y$ values of the aperture. Additionally, this is a scaled Fourier transform of the pupil function due to the denominator of the exponential.

$$\tilde{H}(x,y)=\int_{-\infty}^{\infty}\int_{-\infty}^{\infty}\left|\tilde{h}(x,y)\right|^{2}e^{-j2\pi(xf_x+yf_y)}dxdy$$

$$=\frac{\int_{-\infty}^{\infty}\int_{-\infty}^{\infty}P\left(x+\frac{f_x\lambda z}{2},y+\frac{f_y\lambda z}{2}\right)P^{*}\left(x-\frac{f_x\lambda z}{2},y-\frac{f_y\lambda z}{2}\right)dxdy}{\int_{-\infty}^{\infty}\int_{-\infty}^{\infty}\left|P\left(x,y\right)\right|^{2}dxdy}=H_{opt}(u_2) \qquad (20)$$

In Equation (20), $x$ and $y$ denote spatial locations, $f_x$ and $f_y$ represent frequency locations, $\lambda$ is the wavelength of the concerned light, and $z$ is the propagation distance. This equation describes the normalized OTF, $\tilde{H}(f_x, f_y)$, or $H_{opt}(u_2)$, the optical transfer function for our purposes, in terms of both the PSF and the pupil function. This also illustrates the fact that the OTF is defined as either the Fourier transform of the PSF or the autocorrelation of the scaled pupil function. Additionally, this equation is also shown for an OTF with infinite aperture, and the same method can be used to account for a finite aperture.

### 2.4.3 Atmospheric Model

The effects of random atmospheric turbulence on a system's PSF is a highly researched topic and can be effectively modeled a variety of ways. As seen in Figure 9, the process begins with a light emitting source. The light propagation from this source can be practically visualized as a plane wave because of its distance from the receiver. However, the random fluctuations in the refractive index of air between the ground-based telescope and the source, known as atmospheric turbulence, result in phase distortions in the propagating light field. This distorted wavefront is focused on the detector, and the aberrations due to the atmosphere can be seen in the resulting image.

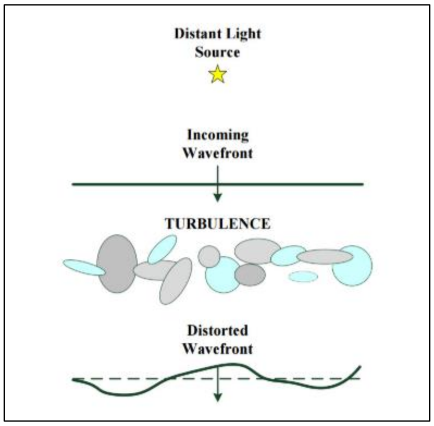

Figure 9. Visual illustration of wavefront distortion due to atmospheric turbulence [25]

In this thesis, there are two different atmospheric models utilized to determine the effects on the optical system. These are long and short exposure models, which are differentiated based on their integration time, which is the length of time they accumulate light for each image frame. Short exposure integration times are generally kept to 10ms or less and are modeled with a short exposure OTF [31]. Long exposure regimes are defined by Goodman as exposure periods much greater than 10ms and are modeled with a long exposure OTF [24]. Details of both models are discussed in the following subsections, along with how they specifically assimilate into this research.

### *Long Exposure Model*

In the reexamination of the FPD algorithm in Chapter III of this research, perfect long-term averages of the atmosphere are used, simulating ideal long exposure operation. The FPD was developed using long exposure statistics, and under short exposure conditions, the PSF can no longer be considered both real and symmetric, invalidating many of the key math simplifications performed during derivation [11]. Therefore, a long exposure scenario must be used. Using this long exposure assumption, the expected atmosphere at different time intervals is not random but can be defined using the long exposure OTF given in Equation (21). Due to the averaging nature of turbulence in a long exposure scenario, the PSF can be presumed to be even and symmetric [31].

$$H_L(f_x, f_y) = \exp\left[-3.44\left(\frac{\bar{\lambda} z\sqrt{f_x^{\,2} + f_y^{\,2}}}{r_0}\right)^{\frac{5}{3}}\right] = H_{atm}(u_2) \tag{21}$$

In Equation (21), $\bar{\lambda}$ is the mean wavelength, $z$ is the focal length of the telescope, $f_x$ and $f_y$ are spatial frequencies, and $r_0$ is the Fried parameter. The Fried parameter, or seeing parameter, is a metric of optical transmission quality through the atmosphere due to random inhomogeneities (typically caused by temperature fluctuations) that affect the atmosphere's refractive index [31]. The seeing parameter is typically a measure of length and can be defined by Equation (22).

$$r_0 = 0.185\left(\frac{\bar{\lambda}^2}{zC_n^{\,2}}\right)^{\frac{3}{5}} \tag{22}$$

In this equation, $C_n^2$ is the atmospheric turbulence strength, $\bar{\lambda}$ is again the average wavelength of the light source, and $z$ is the distance between the source and the telescope aperture. For Chapter III of this research, an average $r_0$ value is used in conjunction with Equation (21) to simulate atmosphere.

### *Short Exposure Model*

As mentioned in the introduction of Section 2.4.2, a short exposure OTF model is commonly used when operating with integration times of approximately 10ms or less [18]. Like the long exposure case, the short exposure PSF is the inverse Fourier transform of the short exposure OTF. The short integration time limits the intensity gathered by the optical system, making imaging and detecting faint space objects more difficult. Due to the erratic nature of the atmosphere especially in short periods of time, modelling the short exposure OTF compels the use of a set of Zernike polynomials at each individual time instance. Past AFIT research by Putnam built accurate individual Zernike phase screens with true temporal correlation statistics [38, 39]. The detection simulation used in Chapter IV of this research exploits the results of this modelling research to create many statistically-correct short exposure PSFs and test multiple frame selection algorithms. Since the model for individual frame creation is short exposure and the frames are analyzed individually before summation, the research in Chapter IV is considered a short exposure technique.

### 2.4.4 Noise Sources

Noise sources impede the ability of optical systems to detect dim objects. The sources of noise in most optical system environments include: photon counting noise, background light, readout noise, dark current and thermal noise. Manufacturers and operators attempt to minimize readout noise, dark current, and thermal noise using more effective cooling methods and higher quality components [27]. For Chapter III of this research, these three sources of noise are considered insignificant, and are therefore ignored. The effects of thermal noise and dark current are normally small, and vary significantly between telescopes, so there is no robust method to simulate them. The read noise is known to be generally insignificant for long exposure scenarios. However, readout noise is a more impactful source of noise for nighttime short exposure studies, so an explanation is included for the purposes of Chapter IV. A discussion of photon counting noise and background light and their relevance in this research is deliberated in the following sections, along with a mention of readout noise.

### *Photon Counting Noise*

Photon noise results from the usage of a CCD array as a detector, and the theorized Poisson nature of light [24]. A CCD array counts the arrival of each photon in each of its separate bins, and because the distribution of light is a random Poisson process, the same object imaged at two separate times could appear to have different intensities. Ideally, a CCD would capture every photon and convert it into a digital count, but this is rarely the case. The probability of $k$ photons, $P(k)$, being counted at each pixel spot is given by the Poisson probability mass function (PMF) shown in Equation (23) where $\bar{k}$ is the mean number of photons expected in the measurement [31].

$$P(k) = \frac{\bar{k}^{k} e^{-\bar{k}}}{k!}, k = 0,1,2,3... \tag{23}$$

### *Background Noise*

Background noise consists of all light present that does not originate from the object measured by the image detector. Numerous sources of background noise exist including: the sun, other stars, and reflections from other objects into the telescope's mirror. Viewing and collecting data from a dark spot of the sky during calibration is one method to estimate the background illumination. For this research, a post-processing technique of subtracting the median value of all pixels in the image data is used, as shown in Equation (6). Removing the median value instead of another statistical average is generally more robust in practice, since it protects against outliers in the data.

### *Readout Noise*

Each CCD pixel captures photons and converts them to electrons based on the assigned gain of the camera. These electrons travel through the circuitry to an analog to digital converter, which translates them into a digital signal. Depending on the camera's hardware, this digital transformation process can result in what is known as readout noise. Under conditional space imaging, read noise is relatively insignificant since the variance of the Gaussian distributed read noise is far outweighed by the noise from photon counting variance [11].

Likewise, the high photon count in short exposure daylight imaging drives the read noise to insignificant levels. However, in short exposure night imaging, read noise has the potential to degrade the SNR of the images comprising dim objects, especially when many short exposure frames are averaged together. This is shown in Equation (24), since the variance for each pixel is related to the Poisson rate parameter, $\overline{K}$, the number of frames being averaged, $F$, and the read noise variance, $\sigma^2_{rn}$.

$$\operatorname{var}\left\{d(x,y)\right\} = F\overline{K} + F\sigma_{rn}^2 \tag{24}$$

## 2.5 Chapter Conclusion

The research in this thesis prioritizes improving currently used object detection algorithms through the improvement of post-processing techniques. This chapter discussed the precursors to this new research and introduced the concepts and methodologies that form the basis of this work. Realistic long and short exposure atmospheric turbulence models and accurate optics and noise models are utilized to ensure the validity of the produced data, and subsequently the results. The FPD algorithm that is reanalyzed in this research is compared against approaches such as a spatial point detector and a matched filter. A newly developed frame selector algorithm is compared against a summed frames correlator and the original frame selector algorithm devised by Becker. The purpose of the reanalysis of the FPD algorithm is to reexamine its viability against high and low-performing iterations of presently used long exposure algorithms. The goal of the new frame selector algorithm development is to improve detection and achieve greater $P_D$ across each given false alarm rate. The $P_D$ and $P_{FA}$ rates are contrasted by viewing an LROC plot with the curves of multiple algorithms plotted on the same axis.

# III. Fourier Point Detection Algorithm

## 3.1 Chapter Overview

This chapter investigates the results from a previously derived space object detection algorithm designed to function with existing ground-based telescopes to improve detection performance. This algorithm was devised by Becker, and later published in his dissertation in 2017 [11]. The distinct facet of this research is that unlike other documented detection algorithms, this algorithm utilizes data in the Fourier domain to make a detection decision. The foundation of the research originates from some of the assumptions of traditional algorithms such as the point detector, specifically that there is a developed LRT that observes Gaussian or Poisson-distributed image data and detects using a BHT. For these reasons, this algorithm was named the Fourier point detector. The LRT for this algorithm hinges on the assumption that the real part of the Fourier transformed observed data will appear different when there is an existing space object in the frame versus when there is solely background noise. The goal of the original research was to examine the statistical distributions of the Fourier transformed data and achieve superior detection performance when the FPD is compared against point detector and spatial correlator algorithms.

## 3.2 Data Modeling

This section communicates the formulation of the expected data received from the real or simulated optical system. The algorithms analyzed in this chapter rely on spatial images, which are captured as a signal from a telescope’s CCD array. These images are later transformed and analyzed according to the requirements of the processing algorithm.

The matched filter and point detector algorithms in this chapter utilize the baseline spatial data received by the optical system, while the FPD algorithm utilizes Fourier transformed image data to analyze the frequency content of the image for detection.

### 3.2.1 Simulated Spatial Data

A model for the expected signal received from a CCD on the detector can be realized by first referencing the imaging system model in Equation (15). To reiterate, this equation outlines that telescope data can be modeled as a Fraunhofer propagation from the source to the detector, which means that the image data can be expressed as a convolution of the object and the PSF at each pixel. Because the PSF is an input, this equation is valid for both short and long exposure data scenarios.

The model for a point source object with no noise or optical aberrations is shown in Equation (25). This simple model for a space object scales a Dirac function at some spatial location *(u, v)* by the space object's intensity, $\bar{K}$.

$$o(u,v) = \bar{K}\delta(u,v) \tag{25}$$

Under the $H_1$ hypothesis, there exists an object with intensity, $\bar{K}$, which varies based on orbit position, orientation, reflectivity, observation angle, and other relevant factors. For the $H_0$ hypothesis, the model in Equation (25) is still accurate because there is no object present, therefore resulting in an intensity value of zero. The expected received image, as shown in Equation (26), is formed using both the model for the expected data, Equation (15), and the point source space object model, Equation (25). There is also background noise, *B*, associated with the image, which arises due to the factors discussed in Section 2.4.

$$E[d(x,y)] = E\left[\int_{-\infty}^{\infty}\int_{-\infty}^{\infty}\bar{K}\delta(u,v)h(x-u,y-v)dudv\right] \tag{26}$$

This expression can be simplified using the sifting property of the Dirac function, resulting in Equation (27) [24].

$$E[d(x,y)] = \bar{K}h(x,y) + B \tag{27}$$

Using this data model and the requirements for received intensities in each case, conditional expected values for the data under each hypothesis can be surmised, as shown in Equations (28) and (29).

$$E[d(x,y) \mid H_0] = B \tag{28}$$

$$E[d(x,y) \mid H_1] = \bar{K}h(x,y) + B \tag{29}$$

As discussed in Section 2.4, the background noise is considered to be a Gaussian distributed random variable whose mean and variance can be measured directly from the image. This research simplifies the data model by subtracting the background data prior to processing. The same pre-processing step is utilized by Becker in his dissertation [11]. The background subtracted data is defined as *d'(x,y)* in Equation (30).

$$d'(x,y) \triangleq d(x,y) - B \tag{30}$$

Substituting *d'(x,y)* into Equations (28) and (29) yields a simplified version of the conditional expected data model, shown in Equations (31) and (32), which streamlines analysis.

$$E[d'(x,y) \mid H_0] = 0 \tag{31}$$

$$E[d'(x,y) \mid H_1] = \bar{K}h(x,y) \tag{32}$$

To summarize, the finalized expected data model with the background subtracted will generally result in no signal when there is no object present and produce a signal according to the PSF scaled by the intensity when there is an object present. This spatial domain data is used directly with the spatial point detector and matched filter algorithms but requires further transformation before use with the FPD.

### 3.2.2 Fourier Domain Data

As previously mentioned, the FPD requires Fourier domain data for analysis, as opposed to the matched filter and spatial point detector which accept spatial data. The fundamental ideas behind transforming the data to the Fourier domain for this research are contained in Chapter II. The key aspects of this process are reiterated in this section.

The procedure used to transform the background-subtracted spatial data is effectively a discrete Fourier transform of the full received image frame. This conversion is shown in Equation (7). The FPD utilizes solely the real component of the Fourier transformed data, because long exposure PSFs are generally real and symmetric, meaning practically no object information is stored in the imaginary component. Utilizing Euler's formula, the data is split into the two components, as shown in Equations (8) and (9). The real component of the data is used directly with the FPD algorithm for detection.

### 3.2.3 Telescope Model

As discussed in Section 2.4.2, the telescope model used in this chapter follows the same parameters as the HST. Specific parameters and a visual example of the aperture of the telescope are included in this section, as well. Although the HST is a space telescope, the parameters are representative of a typical large optical system and are widely available. Because of this, no parameter estimation is required, and modeling is straightforward.

### 3.2.4 Atmospheric Effects

To generate accurate telescope images, the simulated atmosphere must create phase screens that imitate long exposure statistics. The atmospheric turbulence in this research is created utilizing a combination of a seeing parameter, $r_{0,}$ and Equation (21), which creates a real, symmetric PSF due to the averaging nature of long exposure imaging. This equation simulates a long exposure OTF with an infinite integration time, therefore creating the ideal scenario. Although this would be theoretically impossible in an experimental sense, a similar OTF and respective PSF can be achieved by keeping telescope integration times greater than 100ms.

The $r_0$ values used to create the PSFs used in this research are all constants, with the values themselves decided based on the time of day that telescope operation is simulated to occur. Although uncommon, observing near-constant seeing parameters in a physical experiment under long exposure integration times is possible when the wind speed is zero, which is another assumption made for this atmospheric model. Table 2 shows the $r_0$ values used in this chapter to simulate atmosphere, varying by the time of day of telescope operation.

Table 2. Seeing parameters for PSF generation based on time of day

| **Time of Day** | **Seeing Parameter $r_0$ Range** (cm) |
|---|---|
| Night | 3-6 |
| Dusk/Dawn | 2-5 |
| Day | 1-4 |

The values shown in Table 2 are expected parameters based on several studies and collections performed during each of the different daylight scenarios. They do not represent all possible seeing parameters that may be seen, but rather a reasonable range of values that are considered likely for each situation.

### 3.2.5 Noise Sources

A discussion of the sources of noise typically present in imaging scenarios was contained in Section 2.4.4. Aside from dark current and thermal noise, which are considered negated by improved manufacturing processes, the main noise sources include photon counting noise, background noise, and readout noise. In this portion of the research, the imaging telescope operates in a long exposure regime, therefore additionally nullifying the relevance of readout noise.

Photon counting noise is added to the simulation during the generation of the atmospheric PSFs in the form of random Poisson-distributed fluctuations throughout the entire image. This is due to the previously discussed Poisson nature of light. Background noise is considered to arise from this process as well, although this source is subtracted during windowing and pre-processing steps, as mentioned in 3.2.1 and 3.2.3 as well as Chapter II.

## 3.3 FPD Algorithm Development

The FPD and its generalized derivation was discussed in Section 2.3.4. To reiterate, the FPD was designed by Becker as an object detection algorithm based on a LRT design [11]. The foundation of this research centered around the idea that frequency domain analysis of spatial images could result in increased detection performance over traditional spatial detection methods, such as the point detector or matched filter. The FPD algorithm also does not depend on a PSF input to function, like the spatial point detector. Therefore, in situations where the PSF is not known or hard to measure, the FPD algorithm theoretically has an advantage over the spatial correlator.

The intricacies behind the derivation of the algorithm are detailed in Becker's dissertation [11], but are not listed or explored further in this thesis. Overall, the key assumption of the work is that the PSF must be both real and symmetric, which indicates that the optical system must operate in a long exposure regime. The proofs and math simplifications made in the derivation rely on this assumption. The final stage of the algorithm development results in the LRT shown in Equation (12), which is what is tested in this chapter.

### 3.4 Experiment Description

Both simulated and experimental data sets are used to test the detection performance of the FPD algorithm against the spatial matched filter and point detector algorithms. Each data set is simulated or collected with the techniques and considerations discussed in Section 3.2. An explanation of each data set, their underlying purposes, and sample image frames are all included in Section 3.4.1. Lastly, the methods behind applying each algorithm in code using the given image frames, and the foundational equations that were discussed in Chapter II are recapped in Section 3.4.2.

### 3.4.1 Simulated Image Data

Simulated data is used to test the FPD against other algorithms across a range of scenarios. This section outlines the specifics behind the data used in this portion of the research and includes sample frames for each different circumstance.

The main goal of the simulated data is to closely model statistically realistic data that may be received from a ground-based telescope performing long exposure space object detection. Using the approaches outlined in Sections 3.2.1, 1,000 frames of background-subtracted image data for both the $H_1$ and $H_0$ cases were created. Each frame of $H_1$ data in this research generates a realistic dim object in the center of a 1,000 by 1,000-pixel frame, while the $H_0$ data contains only background noise. The Fourier domain data is created using the methods discussed in Section 3.2.2. This frame formation is repeated for each object SNR, and across three times of day: night, dusk/dawn, and day. In this chapter, CCD well depth is ignored, and long exposure integration times are used even during higher light conditions. Statistics to determine the detection performance are generated using a windowed version of the full frame.

Table 3. Assumed average background photon levels based on simulated time of day

| **Time of Day** | **Background** B (photons) |
|---|---|
| Night | 10 |
| Dusk/Dawn | 100 |
| Day | 1000 |

Each photon number in Table 3 represents the average photon level assigned to the background prior to frame creation, but due to the various noise sources incorporated, each data frame will not hold these exact values. The photon values used to simulate the objects of different SNRs are calculated by rearranging Equation (33), where $\bar{K}$ is the average number of photons in the object, $h_{max}$ is the maximum value of the PSF, and $B$ is the mean and variance of the background, since light is generally Poisson [31]. This equation is based on point detector SNR, which is defined as the signal mean divided by the standard deviation of the noise [41].

$$SNR_{Object} = \frac{\bar{K}h_{\max}}{\sqrt{B}} \tag{33}$$

Three different object SNRs were chosen to test the algorithms across a range of differing brightness objects. The $\bar{K}$ values for each of these objects were calculated with this equation using the parameters found during a nighttime simulation with an $r_0$ equal to 6cm. These calculated values are shown in Table 4. The $\bar{K}$ values are held constant during each test iteration to compare across the changing $r_0$ and $B$ values.

Table 4. $\bar{K}$ values associated with each simulated object's point detector SNR

| **SNR** | **$\bar{K}$** (photons) |
|---|---|
| 0.1 | 2600 |
| 0.2 | 5300 |
| 0.4 | 10500 |

In total, 18 tests are performed – the combinations stemming from the three background photon levels based on the different times of day, the three object SNRs and the two different $r_0$ values, chosen as the lowest and highest values from the ranges provided in Table 2. Figure 10 provides a visual of a $H_1$ and $H_0$ sample image frame from the best-case scenario, a nighttime scenario with the highest seeing parameter and SNR value. Figure 11 includes the Fourier transform of each sample frame of data presented in Figure 10.

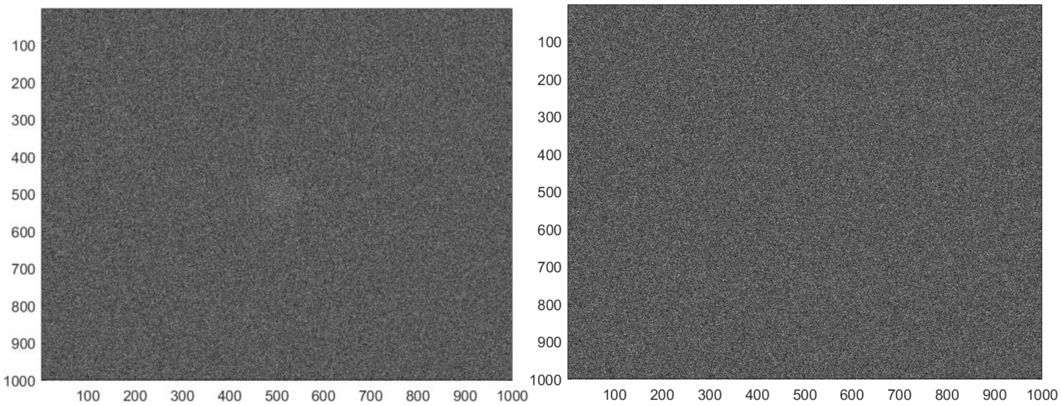

Figure 10. Night background light – simulated data frame with $r_0$ = 6cm, SNR 0.4 for $H_1$ (left) and $H_0$ (right)

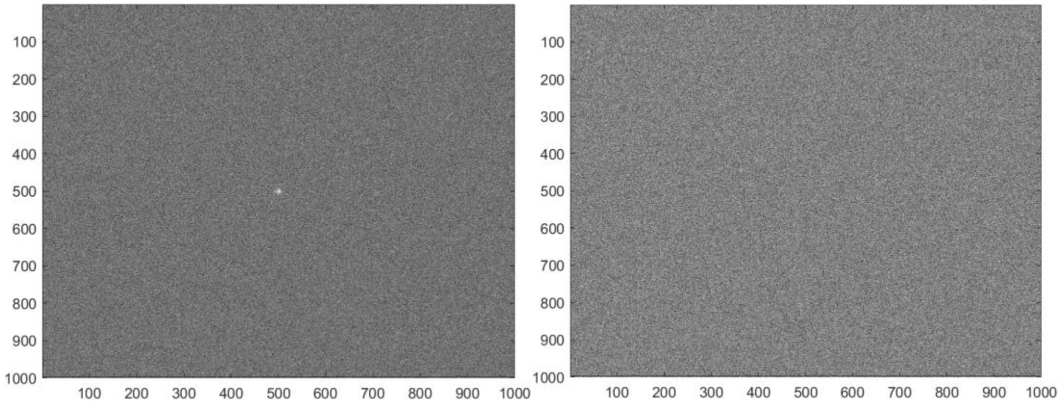

Figure 11. Fourier transform of Figure 10 data frames for $H_1$ (left) and $H_0$ (right)

### 3.4.2 Algorithm Application

The three algorithms tested in this chapter, the point detector, matched filter, and FPD are implemented in MATLAB following Equations (2), (5), and (11), respectively. All algorithms utilize the same data set to protect against bias. Data formulation and transformation, as well as noise and atmospheric turbulence are implemented in the data according to the techniques outlined in Section 3.2. Additionally, each detection scheme has no prior knowledge about the existence or absence of space objects in the supplied image frames. Aside from basic implementation, there are a few details concerning inputs to the matched filter algorithm, along with a key data distribution assumption that are discussed in the following subsections.

#### ***Matched Filter Algorithm Input***

The matched filter algorithm requires an input of the estimated system PSF, so in order to fully determine a reasonable range of detection performance yields, both true and incorrect PSFs are supplied to the algorithm. The true PSF is considered to generate the best-case results, and the incorrect PSFs will help visualize the performance decreases possible from poorly estimating the PSF. Each PSF is created using the concepts reiterated in Section 3.2.4. The average $r_0$ values used to simulate the incorrect PSFs are a factor of 1.5 and 2 away from the original, true PSF.  A PSF estimation whose $r_0$ is a factor of 2 away from the true value is considered the worst-case scenario, as this would be a gross miscalculation in a real-world experiment. However, a factor of 1.5 may be a more reasonable error. Figure 12 illustrates an example of the true PSF compared to the incorrect PSFs on an identical pixel scale that may be supplied to the matched filter algorithm during testing. Both the standard and Fourier point detector algorithms do not require the input of a PSF, so their performance is not theoretically affected by poorly estimated system PSFs.

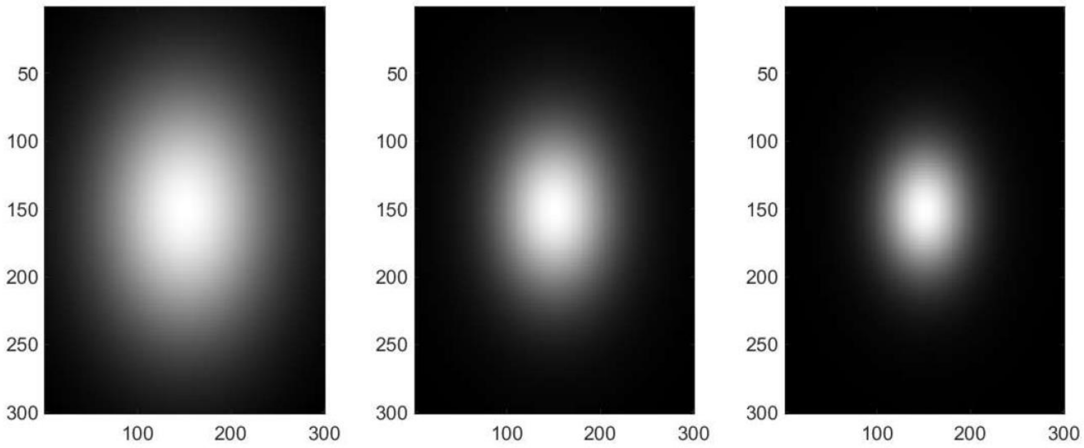

Figure 12. Sample long exposure PSFs supplied to correlator algorithm: true PSF, $r_0$: 3cm (left), incorrect PSFs, $r_0$: 4.5cm (center) and $r_0$: 6cm (right)

### *Gaussian Data Assumption*

The detection performance of each of the algorithms compared in this chapter are determined using an LROC curve with a Gaussian assumption for the data. The methodology behind this technique is discussed in Section 2.3.6 with key Equations (13) and (14), which are used to calculate the $P_D$ and $P_{FA}$ across all desired threshold values. This is a common method used to determine the performance of space object detection algorithms, and for the purpose of confirming model validity, histograms of each of the $H_1$ and $H_0$ data outputs across all scenarios described in Section 3.4.1 were examined.

Figure 13 is one sample histogram for the FPD output data from a test in a nighttime collection setting where the object SNR was 0.1, and the selected $r_0$ value was 6cm. This single figure is indicative of the histograms retrieved from each other algorithm under the different scenarios.

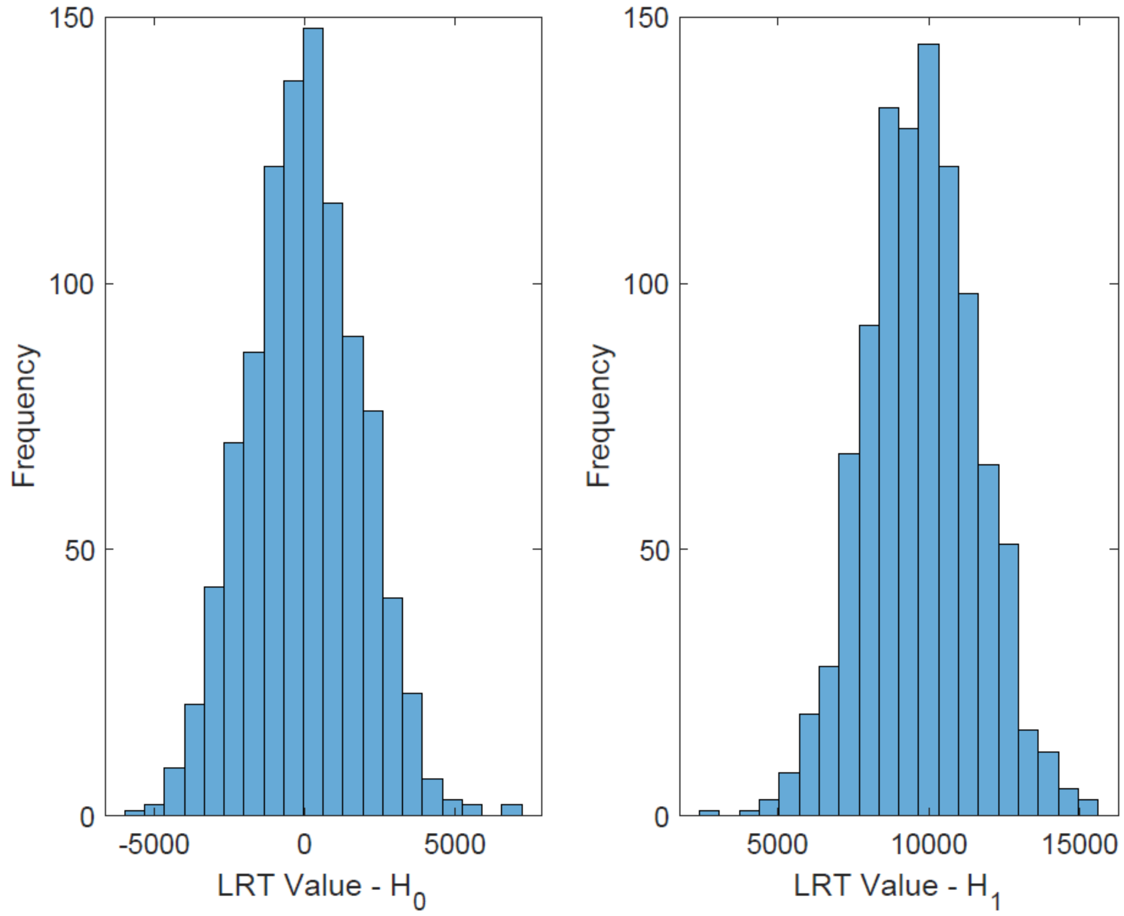

Figure 13. FPD algorithm histogram sample

The key takeaway from Figure 13 is that the data appears to follow a normal distribution. The histograms created from the outputs of every other algorithm and scenario were checked for Gaussian validity as well, although they are not shown due to conciseness.

A Lilliefors test was also conducted in a nighttime scenario to verify the normality assumption of both the FPD algorithm and the spatial correlator algorithm outputs. Each test was performed based on a total of 10,000 output data points. The results are very conclusive, indicating that each the $H_0$ and $H_1$ data follows a Gaussian distribution – the calculated p-values are shown in Table 5.

Table 5. Lilliefors normality test results for FPD and spatial correlator described in Chapter III

| **Algorithm** | **$H_0$ p-value** | **$H_1$ p-value** |
|---|---|---|
| FPD | >.5 | .350 |
| Spatial Correlator | .214 | .221 |

## 3.5 Results

The resulting LROC curves from the experiment outlined in Section 3.4 are presented in Section 3.5.1, along with concise performance analysis of the algorithms with respect to each other. Additionally, a brief explanation of the results from the original implementation of the FPD algorithm and a commentary as to whether this new research confirms the results is included in Section 3.5.2.

### 3.5.1 Simulated Data LROC Curve Analysis

This subsection offers the results of the experiment in the form of LROC curves of each test scenario. These findings are further divided into three sections: night, dusk or dawn, and day, denoting the simulated operation time of the receiving ground-based telescope. Each divided section consists of a brief explanation of some of the specific parameters used in each scenario, figures to portray the results from the respective portion of the experiment, and a succinct statistical comparative analysis of each algorithm.

#### *Night*

The results for each algorithm in a nighttime scenario are shown in Figure 14, Figure 15, and Figure 16. For these tests, the selected $r_0$ values are 3cm and 6cm, which are the lowest and highest seeing parameters for the night setting from the ranges shown in Table 2. The left side of each figure depicts the higher $r_0$ value, and the right side the lower $r_0$ value, with all other parameters held constant.

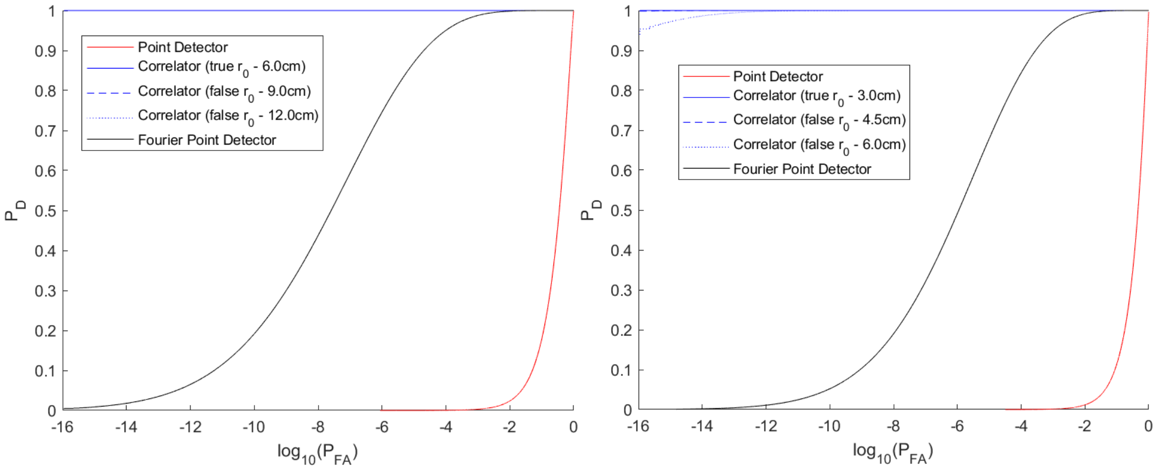

Figure 14. LROC curve comparison – Night scenario, object PD SNR 0.4 with (left) $r_0$ = 6cm and (right) $r_0$ = 3cm

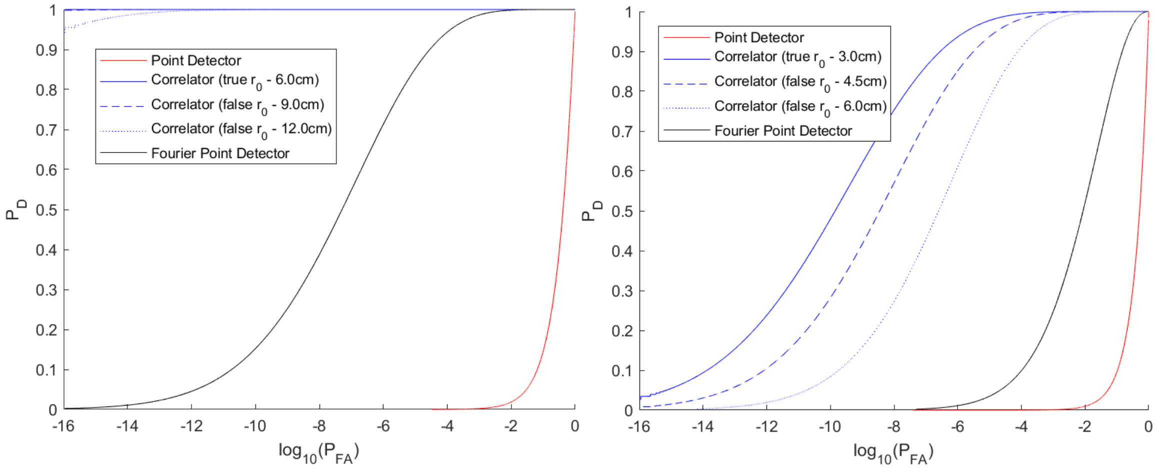

Figure 15. LROC curve comparison – Night scenario, object PD SNR 0.2 with (left) $r_0$ = 6cm and (right) $r_0$ = 3cm

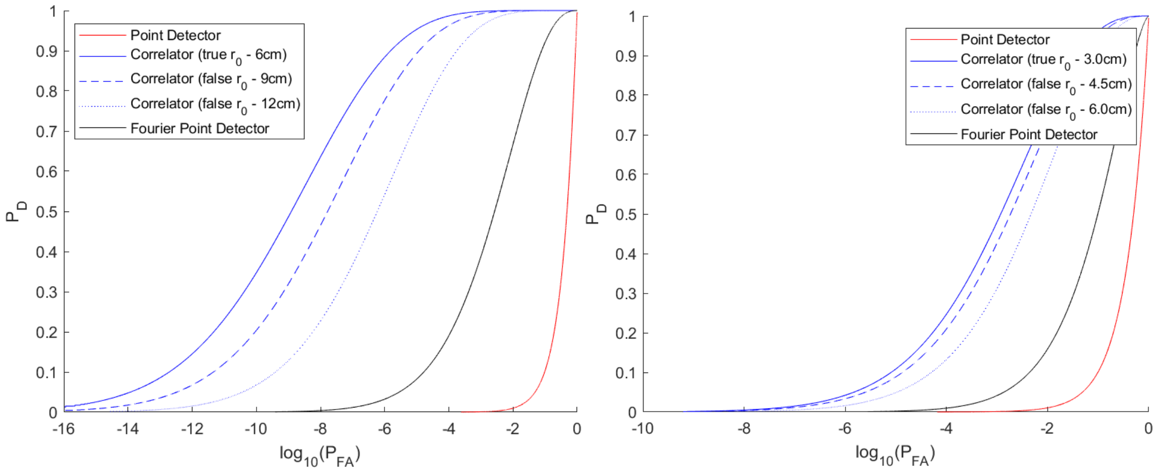

Figure 16. LROC curve comparison – Night scenario, object PD SNR 0.1 with (left) $r_0$ = 6cm and (right) $r_0$ = 3cm

From these figures, the reasonable conclusion is that in a nighttime, low-SNR object detection scenario, the correlator significantly outperforms the FPD algorithm. For the 0.4 SNR object in Figure 14, the correlator exhibits a 75-90% increase in $P_D$ at a fixed $P_{FA}$ of $10^{-9}$, varying by $r_0$ value. The issues with supplying the incorrect PSF manifest in the results from the 0.2 SNR object in Figure 15, but even with these prevalent effects included, the correlator boasts $P_D$ increases of 15-75% over the FPD at the same $P_{FA}$. Similar results can be seen in Figure 16 in the case with the very dim object with SNR 0.1. In this case the performance gap is large, showing a 15-60% $P_D$ increase at a $P_{FA}$ of $10^{-9}$ for the 6cm seeing parameter case, and a 30-50% $P_D$ increase at a $P_{FA}$ of $10^{-3}$ for the 3cm seeing parameter case, varying by the incorrectness of the supplied PSF.

Similar deductions can be drawn for the differences between the FPD and the spatial point detector. Overall, the FPD algorithm performs significantly better than the point detector, but worse than the spatial correlator despite the inaccuracy of the supplied PSF under these conditions.

### *Dusk/Dawn*

The results for each algorithm in a dusk or dawn scenario are shown in Figure 17, Figure 18, and Figure 19. For these tests, the selected $r_0$ values are 2cm and 5cm, which are the lowest and highest seeing parameters for the dusk and dawn setting from the ranges shown in Table 2. The left side of each figure depicts the higher $r_0$ value, and the right side the lower $r_0$ value, with all other parameters held constant.

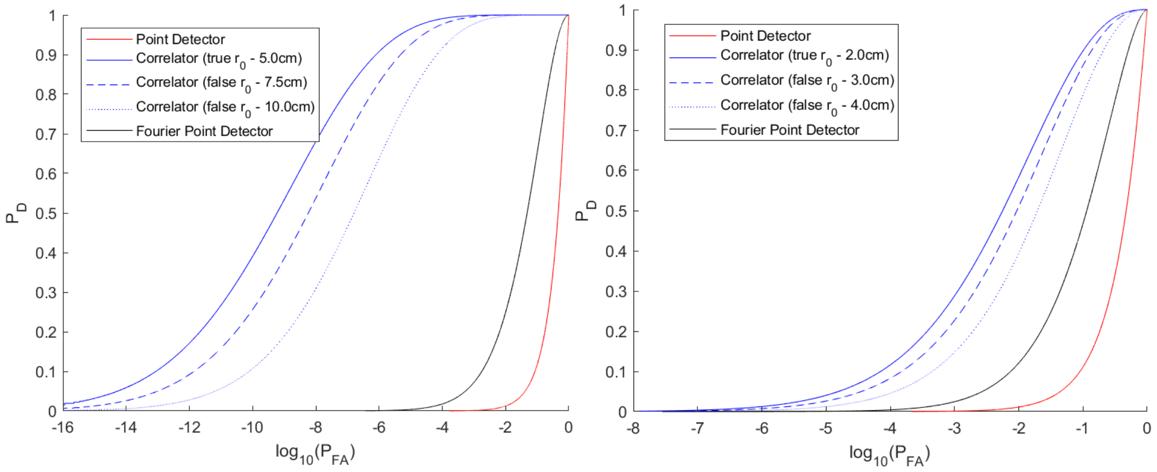

Figure 17. LROC curve comparison – Dusk/dawn scenario, object PD SNR 0.4 with (left) $r_0$ = 5cm and (right) $r_0$ = 2cm

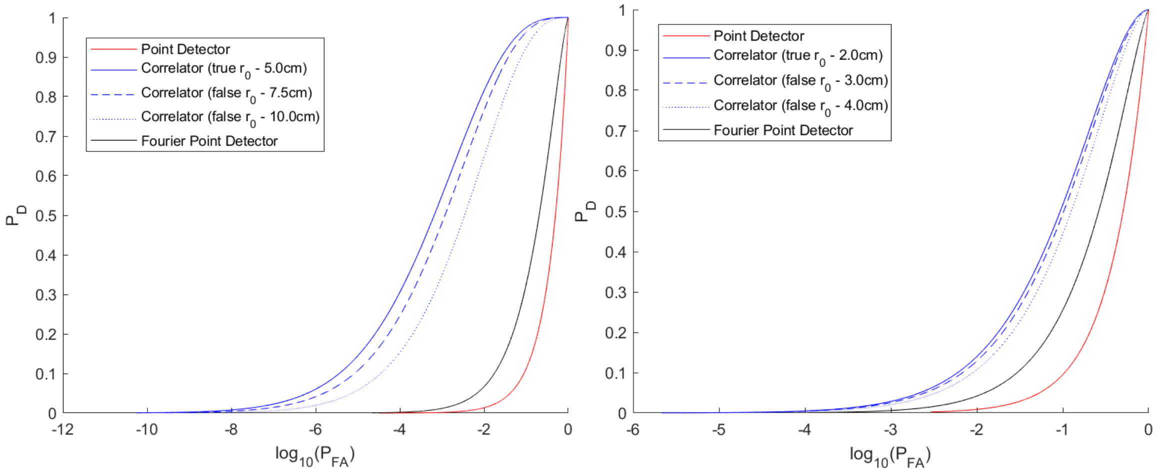

Figure 18. LROC curve comparison – Dusk/dawn scenario, object PD SNR 0.2 with (left) $r_0$ = 5cm and (right) $r_0$ = 2cm

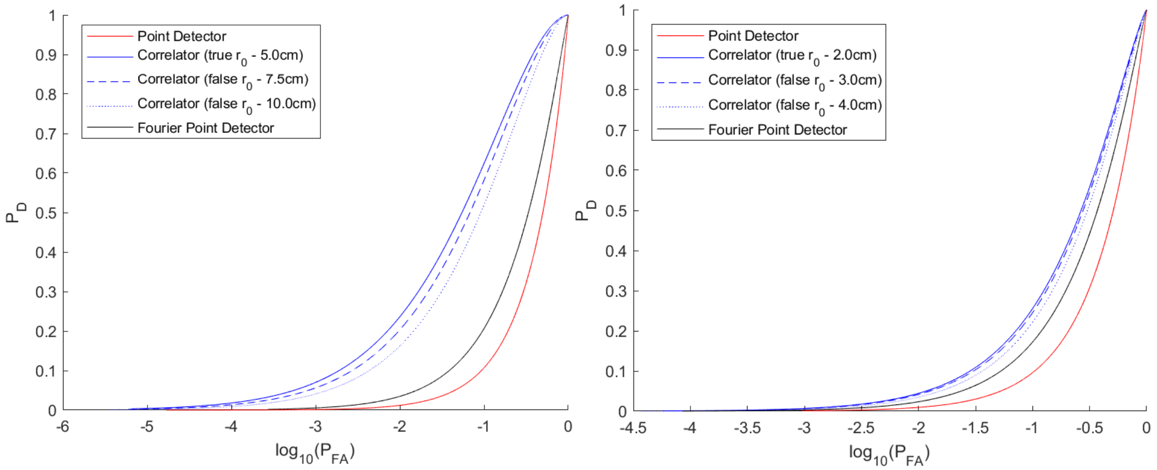

Figure 19. LROC curve comparison – Dusk/dawn scenario, object PD SNR 0.1 with (left) $r_0$ = 5cm and (right) $r_0$ = 2cm

These figures show that in a dusk or dawn, low-SNR object detection scenario, the correlator again outperforms the FPD algorithm, and the FPD outperforms the spatial point detector, although by a smaller margin. The $P_{FA}$ rates are relatively higher, indicating the algorithms are not necessarily suited for dim object detection during higher background light imaging. Similar statistics can be extracted like the previous subsection, but the end conclusion is that the correlator, even with an estimated PSF a factor of 2 away from the true PSF performs magnitudes better than the FPD.

### *Day*

The results for each algorithm in a daytime scenario are shown in Figure 20, Figure 21, Figure 22. For these tests, the selected $r_0$ values are 1cm and 4cm, which are the lowest and highest seeing parameters for the day setting from the ranges shown in Table 2. The left side of each figure depicts the higher $r_0$ value, and the right side the lower $r_0$ value, with all other parameters held constant.

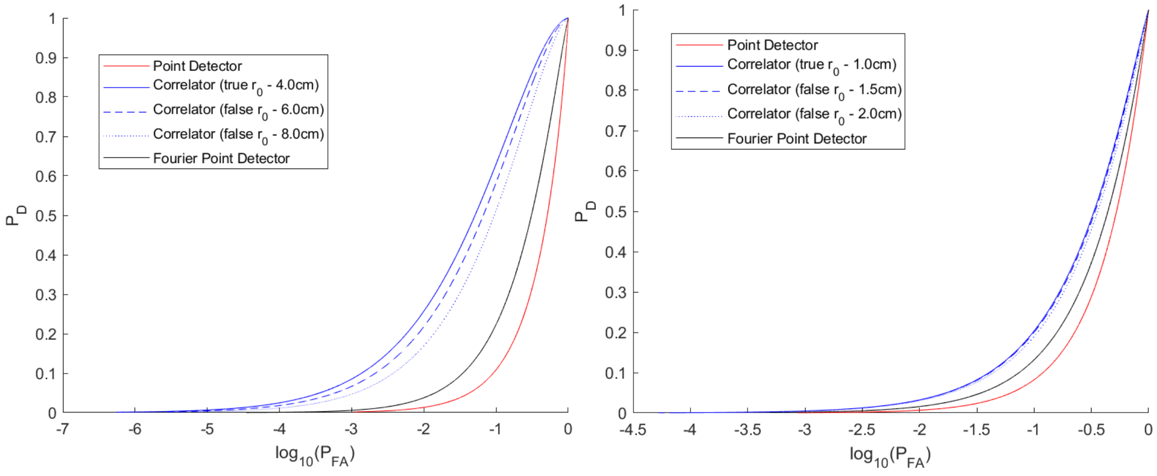

Figure 20. LROC curve comparison – Day scenario, object PD SNR 0.4 with (left) $r_0$ = 4cm and (right) $r_0$ = 1cm

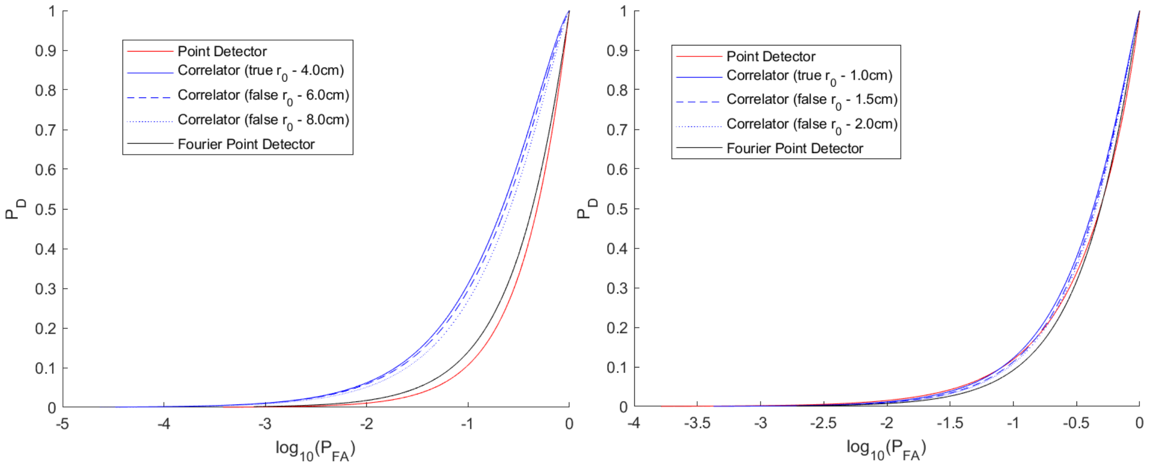

Figure 21. LROC curve comparison – Day scenario, object PD SNR 0.2 with (left) $r_0$ = 4cm and (right) $r_0$ = 1cm

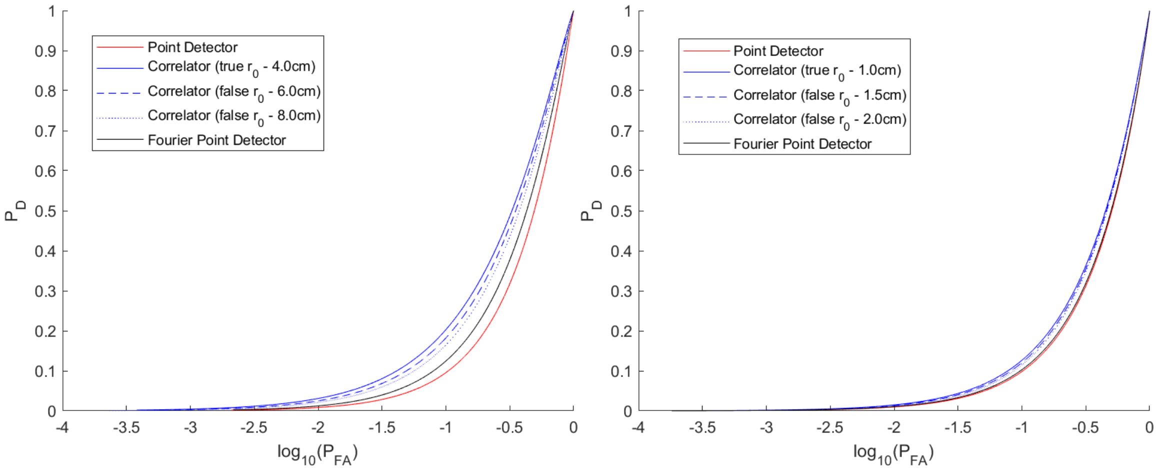

Figure 22. LROC curve comparison – Day scenario, object PD SNR 0.1 with (left) $r_0$ = 4cm and (right) $r_0$ = 1cm

These figures show the general inadequacy of low-SNR object detection during a daylight scenario with these algorithms in question. However, to exhaustively test the algorithms against each other and ensure there are no strange artifacts present, all times of day were taken into consideration. Still, from each of these figures, the slim margins of difference between the LROC curves of the algorithms still indicate that the spatial correlator outperforms the FPD, and the FPD beats the spatial point detector across all the different tests.

### 3.5.2 Prior Results Comparison

In the original implementation of the FPD algorithm, the simulated results from the LROC curve suggests that the FPD "significantly outperform[s] a spatial point detector" [11]. The LROC curve analysis shows a 40-50% increase in the $P_D$ at a $P_{FA}$ of $10^{-9}$ between the two algorithms. The tests in this work solely tested a nighttime scenario and attempted detection of brighter space objects, but comparison to the results in this chapter show that for all simulation environments, the FPD did outperform the point detector algorithm with the same information. The difference in performance is much less defined in the dusk/dawn and daylight tests, but the $P_D$ at each fixed $P_{FA}$ is undeniably greater for the FPD algorithm. Therefore, the initial assertion that the FPD outperforms the point detector algorithm is supported by this new research.

However, the secondary claim made in the original publication that the FPD "provides the same performance as the spatial correlator but with less information required to operate it" is not corroborated. The first research additionally boasts that the FPD yields a 34% increase in performance over the spatial correlator using an incorrect PSF. In the simulated experiment performed in this chapter, the spatial correlator outperformed the FPD across every different test scenario, including when incorrect PSFs that were a factor of 1.5 and 2 away from the true PSF were supplied to the algorithm.

## 3.6 Chapter Conclusion

This chapter reinvestigated a Fourier point detection algorithm that uses the real component of the Fourier transform of the spatial data to make detection decisions. The algorithm relies on long exposure statistics to develop a LRT based on the conditional probabilities that an object will or will not be present in the scene. The FPD algorithm, along with the spatial correlator and point detector algorithms were implemented in MATLAB and compared through the analysis of LROC curves across the various test scenarios.

The research in this chapter focused on testing the previously published results of the FPD to see if the algorithm is truly viable when compared against a spatial correlator. While the FPD algorithm did outperform the spatial point detector, as expected, the results from the LROC curves show that the spatial correlator outperforms the FPD in every test conducted. The simulated data to test this hypothesis was varied with different object SNR levels, seeing parameters, and background light conditions. The definitive conclusion is that the $P_D$ of the spatial correlator is significantly greater than that of the FPD at the same $P_{FA}$, with the performance gap wider at lower background light levels.

Therefore, although the FPD is a relatively simple algorithm and requires no knowledge of the exact PSF shape, the algorithm is not viable as an improvement to the spatial correlator. Even when supplied an incorrect PSF that was a factor of 2 away from the true PSF, which would be a significant estimation error, the spatial correlator beat the FPD decisively. For this reason, the FPD was not analyzed further.

# IV. Short Exposure Frame Selection Algorithm

## 4.1 Chapter Overview

A major limiting factor of the space object detection mission is the insufficient telescope time for data collection. Poor weather, maintenance, and upgrades all detract from the total time telescope operators have available to gather images. Aside from these unavoidable issues, the current greatest obstacle is likely the amount of prime night sky available. Imaging in daylight conditions is possible with smaller aperture telescopes, although the current focus is primarily on imaging objects whose existence is already known [22, 32]. The higher level of background light present inhibits long exposure imaging since the limited well-depth of currently used camera CCDs will result in near-instant pixel saturation. Short exposure imaging combined with proper sun avoidance measures effectively circumvents these issues, and the shorter integration times can allow for thousands of images to be taken in the same amount of time as a single long exposure image. Existing processing of short exposure images is primarily accomplished with traditional long exposure techniques such as the point detector or matched filter [27, 29, 35]. Unfortunately, due to their long exposure-founded derivations, these methods do not provide optimal detection performance.

Notable research in the short exposure imaging domain has yielded near diffraction-limited observations on ground-based telescopes with diameters up to 2.5m. This research relies on image registration and combination, both of which necessitate the existence of a guide star to determine image quality for retention [36, 37, 41]. Because of this requirement, this process is ideally used for high-resolution imaging of previously detected objects, like the speckle or lucky imaging techniques discussed in Section 2.3.7.

Furthermore, despite the challenges, interest in daylight imaging and detection with large diameter telescopes has recently grown [20, 21, 23, 32]. In addition to the pixel well saturation and sun avoidance issues that encumber all current daylight imaging systems, large telescopes have a more serious heating and cooling hurdle than their smaller diameter counterparts. The large primary mirrors on these telescopes absorb more sunlight, which can result in temperature fluctuations on the exposed glass surfaces, equating to random optical fluctuations that are complicated to resolve.

The research in this chapter focuses on improving the detection performance of small and dim space objects in short exposure data retrieved from current ground-based telescope systems. Specifically, a new post-processing detection algorithm is developed based on averaging a subset of selected frames taken from a larger total set of short exposure images obtained from a small aperture telescope. This concept stems from a previously employed frame selection algorithm, whose results were skewed by a faulty data distribution assumption [11]. The improved algorithm in this chapter remedies the issue and reveals the true detection performance increases from this style of algorithm. The frame selection procedure follows a two-pass approach to process the images based on correlation between the resulting data and the expected PSF. Multiple short exposure images are first combined, then individually and recursively removed to determine which frames have the most impact on maximizing this correlation. The process has similarities to the standard matched filter algorithm, but the fundamental difference is in the averaging of the short exposure frames. The traditional matched filter would simply combine all available image frames and perform correlation based on the summation, but the frame selection approach discards especially turbulent or outlier frames that do not contribute to improving the image. Lucky imaging also has resemblances, but the frame ranking that occurs in the frame selection algorithm is performed as a comparison between all total frames versus the individual metric that lucky imaging utilizes.

The proposed algorithm is analyzed in both daylight and traditional nighttime imaging scenarios. Increasing space object detection capabilities during daylight conditions maximizes the time that ground-based telescopes can be operated effectively, therefore benefitting the SDA detection mission. Testing is conducted in the nighttime scenario to potentially further improve the capabilities of existing telescopes by using a short exposure method to seek undiscovered objects that have previously escaped detection.

The results of the novel frame selection algorithm are compared to those of the initial iteration of the algorithm with the faulty assumption fixed, as well as a spatial correlator or matched filter algorithm, as is commonly used in the SDA community. The models behind the simulated and experimental data are outlined in Section 4.2, followed by the development of the old and new frame selection algorithms in Section 4.3. The experiment setup and subsequent detection performance results across each algorithm are deliberated in Sections 4.4 and 4.5, respectively, with the probability of detection and false alarm displayed using LROC curves similarly to Chapter III.

## 4.2 Data Modeling

This section includes the means behind modeling the various data sets used in this chapter. There are many similarities to the models used in Chapter III, and some sections heavily reference the explanations used in the previous chapter. However, because the research in this chapter uses a short exposure model with short integration times, there are some distinct differences.

### 4.2.1 Simulated Data

The image data formulated in this chapter is based on the imaging system model described by Equation (15) in Section 2.4.1. In the research performed in Chapter III, a model is derived for the expected signal received from a detector CCD based on this imaging system model. An input to this model is the system's PSF, which means it applies to both short and long exposure data scenarios. The research in this chapter uses a series of short exposure PSFs. The simulated data follows directly from the model proposed in Section 3.2.1, with the sole exception of utilizing a short exposure PSF versus a long exposure PSF. For brevity, this derivation is not reiterated in this chapter. Combining the model for the data and those for the telescope, atmosphere, and noise, the simulated data is generated in MATLAB for both the $H_1$ and $H_0$ hypotheses. Signal background and space object SNR are varied according to the desired experiment setup.

### 4.2.2 Experimental Data

The available relevant experimental data is limited. For this reason, its purpose in this research is to corroborate the results found from the simulated data. In order to collect short exposure data of dim space objects, a small aperture telescope was used, with an integration time of 10ms. Image gathering was performed during low-light dusk hours. The telescope model described in Section 4.2.3 fits both data sets, since the simulated data was designed to replicate the environment existing during the experimental data collection. Furthermore, the atmospheric data collection encompassed a larger 100 by 100-pixel area of the sky which contained a variety of bright and dim space objects, including Polaris A and Polaris B. This scene is depicted in Figure 23. The acquired data was windowed to capture two dim objects: Polaris B, and another nearby indistinct star. For each set, 1,000 32 by 32-pixel short exposure image frames were captured for testing. This data is further explored in Section 4.4.2.

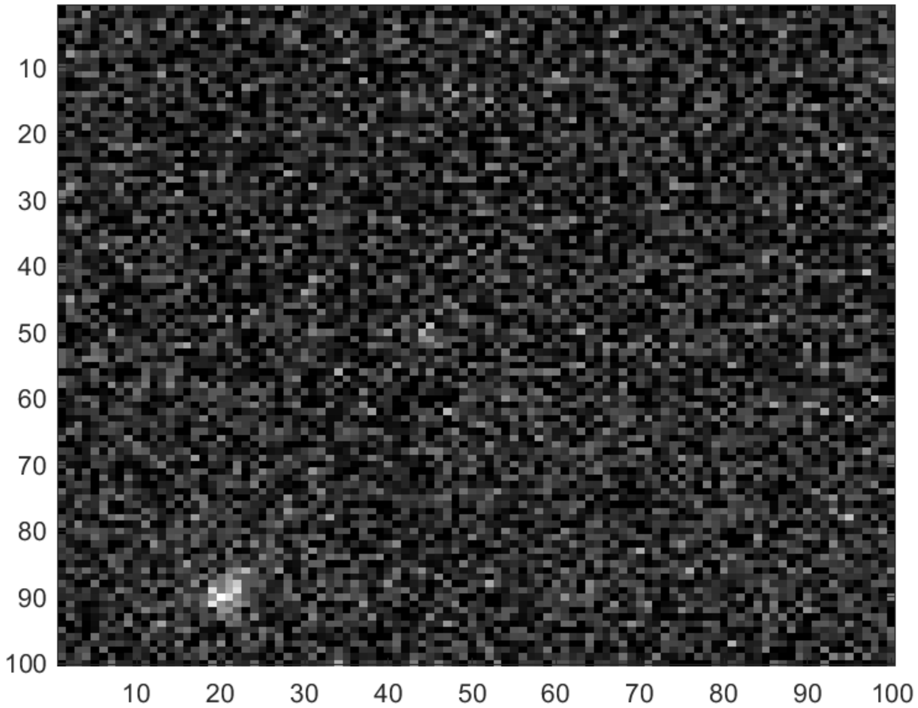

Figure 23. Full captured sky scene used to create windowed data sets

### 4.2.3 Telescope Model

The parameters behind the small aperture telescope utilized in this chapter are found in Table 1 in Chapter II. This optical telescope is designed to be nearly aberration free, which is not impossible for a small system. Aberrations from the optics themselves are therefore assumed to be insignificant and are ignored for this research. As discussed in Section 2.4.2, this is realized as equivalence between the system's aperture and pupil functions. The aperture/pupil functions of the different telescopes used in Chapter III and Chapter IV are illustrated as a side-by-side comparison in Figure 8.

### 4.2.4 Atmospheric Effects

Understanding the effects of atmosphere on imaging is a vastly important field and can be effectively modeled. For a more complete discussion on the premise of atmospheric modeling, reference Section 2.4.3. The specifics behind simulating or estimating the atmosphere in the simulated and experimental data used in this research is divided into the following subsections.

#### ***Simulated***

For the research in this chapter, the accuracy of generated telescope images is reliant on the simulated atmosphere imitating long exposure statistics. Previous research has demonstrated that the statistics of the atmosphere will contain correlation between consecutive time instances, assuming the absence of extreme turbulence [38, 40]. Furthermore, long exposure images can be approximated as a summation of multiple short exposure images with a total integration time exceeding 100ms. This research utilizes consecutive short exposure frames to make detection decisions, so to manufacture realistic data, the supposition that atmospheric statistics are correlated and evolve temporally over time is used. As outlined in Section 2.4.3, Putnam's research creates a model for the atmosphere by employing Zernike polynomials along with Taylor's frozen flow hypothesis [38, 39]. This allows for the creation of numerous correlated atmospheric PSFs with accurate seeing conditions and wind speeds in MATLAB.

The PSFs used with each detection algorithm is generated based on a seeing parameter, $r_0$ and an integration time of 10ms to match the experimental data collection. Like Chapter III, the $r_0$ values in this research are constants, which, as discussed in Section 3.2.4, is a necessary assumption. Additionally, for consistency across experiments, the same $r_0$ ranges for each time of telescope operation is used, as shown in Table 2. A single short exposure PSF instance with an $r_0$ value of 3cm, along with a long exposure PSF, or the summation of 10 short exposure PSFs, are shown in Figure 24. These images are shown on a windowed 32 by 32-pixel frame. The long exposure PSF is an example of the input that would be used with the spatial correlator algorithm, while the frame selection algorithms use combinations of the individual short exposure frames, depending on the number of frames they keep for detection.

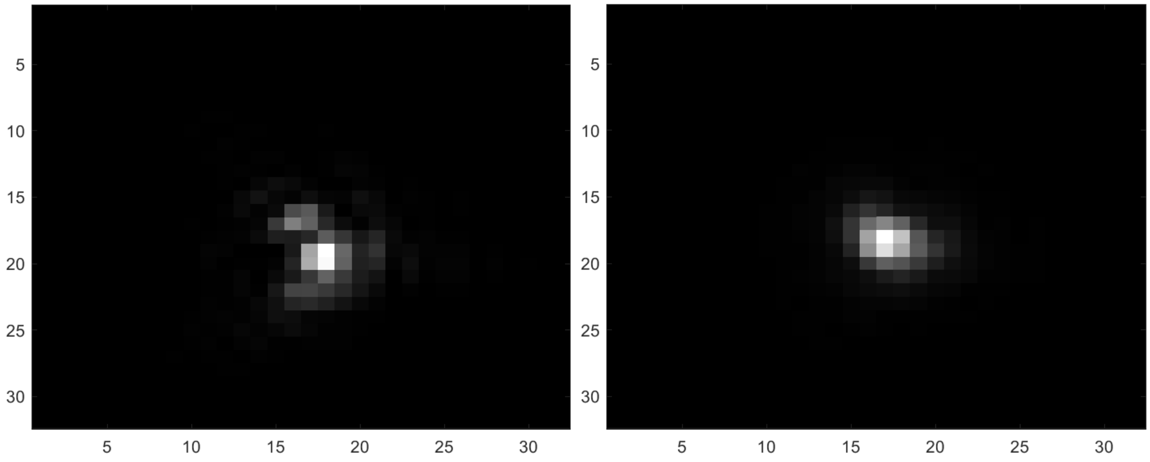

Figure 24. PSF iterations with $r_0$ = 3cm for: (left) single short exposure PSF and (right) long exposure PSF as the summation of 10 short exposure PSFs

### *Experimental*

The experimental data, whose collection was described in 4.2.2, was analyzed to determine the atmospheric seeing conditions present during observation. The existing optical and atmospheric aberrations were correlated with various $r_0$ values to most determine the average seeing parameter that most accurately described the scene at the time of collection. Figure 25 shows a slice of the estimated PSF from viewing Polaris A in comparison to a PSF with a constant $r_0$ value of 2.5cm.

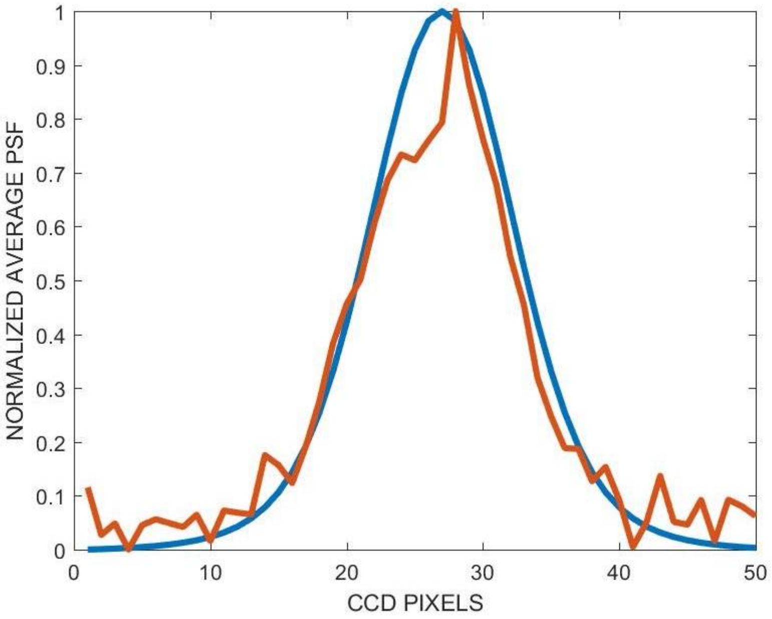

Figure 25. Estimated PSF obtained from Polaris A in red versus the calculated curve from a seeing parameter $r_0$ = 2.5cm in blue [31]

Although this seeing parameter estimation is calculated based on the surroundings of Polaris A, the brightest star imaged by the small aperture telescope during collection, both Polaris B and the other dim space object used to create the data sets used in this research are assumed to have the same atmosphere. The physical optics and the telescope operation time are both held constant, so this is a based assumption.

The actual PSF gathered from the scene, which again has been determined to approximately follow a constant $r_0$ value of 2.5cm, is shown in Figure 26 in a windowed 32 by 32-pixel frame.

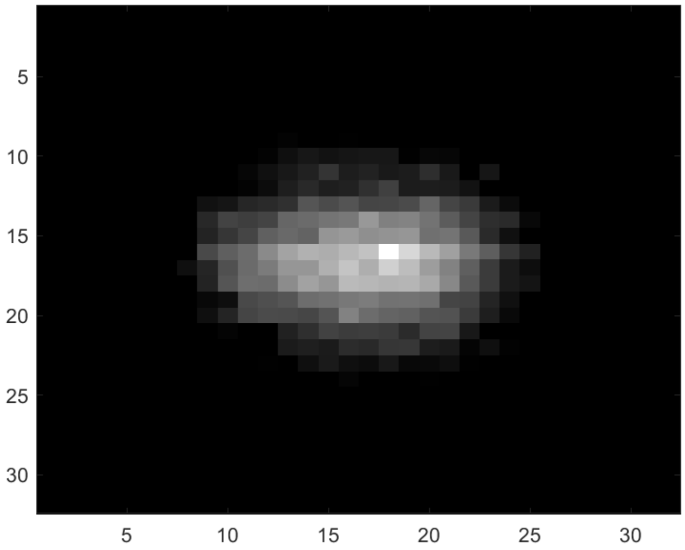

Figure 26. PSF estimated from observation of Polaris A

Finally, the measured mean backgrounds present in both experimental data sets are included in Table 6. The differing backgrounds can be attributed to their differing proximities to the brightest source in the image, Polaris A. The higher background present in the data set of the dim star indicates that it is closer to Polaris A, and because of this, harder to detect.

Table 6. Experimental data sets average measured backgrounds

| **Data Set** | **$H_0$ Background** | **$H_1$ Background** |
|---|---|---|
| Polaris B | 107.0260 | 114.8860 |
| Dim Star | 444.7630 | 458.3970 |

### 4.2.5 Noise Sources

Photon counting noise and background noise, two of the prominent sources of noise in this research, are accounted for in this chapter as they were in Chapter III. The discussion of their relevance and implementation is included in Section 3.2.5. The new relevant noise in this chapter is detector readout noise. Unlike the long exposure study in the previous chapter, this research uses data collected in a short exposure regime. Readout noise is present in collected image frames, so the summation of multiple short exposure frames results in accumulation of this noise source. Equation (24) denotes the effect of readout noise on the overall variance of the collected data.

As deliberated in Section 2.4.4, the effects of readout noise in short exposure daylight imaging scenarios are driven to inconsequential levels by the high photon counts. However, in short exposure night imaging situations, the readout noise does pose an issue, since the levels may be on par to the intensity of the objects being imaged.

Fortunately, the summation of many short exposure frames does not significantly skew the other statistics in the images. The Poisson photon noise statistics of the resulting frame is theoretically comparable since the sum of multiple Poisson random variables is also a Poisson random variable with a rate parameter equal to the sum of the individual rate parameters [24, 31].

## 4.3 Frame Selection Algorithm Development

Space object detection algorithms utilize single or multiple images gathered from a telescope, depending on the system setup. Commonly, SDA programs have a search process beginning with detection in a single image frame, using multiple frames solely for validating the detection decision or reducing the false alarm rate to satisfy mission requirements. The algorithm proposed in this chapter focuses on improving the detection of dim space objects in a single long exposure data frame, with the intention of relaying the detection decision to follow-up analysis techniques. Each long exposure frame is subdivided into ten assumed short exposure frames whose integration times range from 10-25ms, so that the algorithm can take advantage of the characteristics of short exposure atmospheric turbulence to improve detection performance. The selected camera imaging rates are not arbitrary, but rather selected to signify the limited time periods that ground-based telescopes have available to survey each section of the sky in searching for new objects. Unlike a traditional algorithm like the matched filter, which would use the original long exposure image as the input, the frame selection process eliminates the short exposure frames that decrease the overall image SNR and resulting detection performance. The following subsections describe the original frame selection algorithm, as explored by Becker, as well as the erroneous data distribution assumption resulting in misreported detection performance [11]. Additionally, the details of the new frame selection algorithm are discussed, specifically the means by which it rectifies the original algorithm’s key distribution issue.

### 4.3.1 Original Algorithm

The foundation of the original frame selection algorithm starts with an altered rendering of the matched filter detection algorithm, traditionally used with long exposure data. As a preprocessing step, the estimated background, $B$, is calculated as the median intensity value of all the pixels in the windowed image frame, as shown in Equation (6). This background estimate is removed from the data to create a normalized image frame.

As mentioned in the introduction of this section, each individual long exposure image frame is divided into 10 frames of short exposure data during every iteration. After these preparatory transformations are conducted, the algorithm's two-part process of frame ranking, and selection begins. These methods are outlined in the subsections below, followed by an analysis of the erroneous distribution assumption used to report the original algorithm's detection performance in the latter subsection.

### *Frame Ordering*

In order to select the ideal frames for summation and subsequent detection attempts, each frame must first be ranked. This processing phase involves removing a single frame at a time and convolving the summation of the remaining frames, $d_k$, against the expected PSF, $h(x,y)$. The convolution is calculated in the Fourier domain as a multiplication between the background-subtracted Fourier transformed data and the long exposure OTF, $H_L$, which is the Fourier domain representation of the system's PSF, as discussed in Chapter II. This procedure continues by iteratively removing each individual frame to determine SNR values for the data with the $n^{th}$ frame removed, which is denoted by $SNR_{FS}(n)$ in Equation (34). After each SNR values are calculated, they are ranked in descending order, which corresponds to which frames negatively affect the SNR the most upon removal.

$$SNR_{FS}(n) = \sum_{k=1, k\neq n}^{n} \left(d_k(x,y) - B\right) * h(x,y) \tag{34}$$

After each SNR values are calculated, they are ranked in descending order, which corresponds to which frames negatively affect the SNR the most upon removal. A visual representation of this first processing step is also shown in Figure 27.

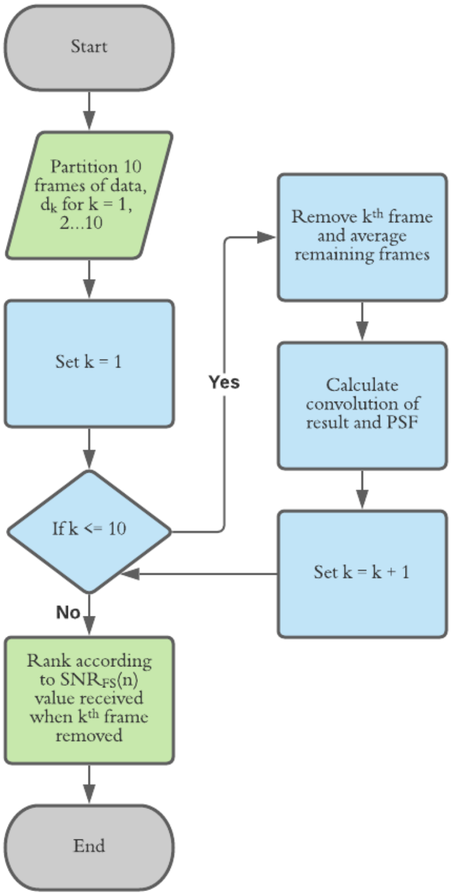

Figure 27. Flow chart of frame ordering process [11]

### *Frame Selection*

After all the short exposure frames are ordered according to the first processing step, the frame selection algorithm removes the individual frame whose elimination resulted in the highest SNR calculation from Equation (34). The remaining frames are combined through summation, and the new SNR baseline value is calculated using the correlation between these summed frames and the expected PSF. This SNR value is found using the same calculation as the matched filter SNR, as given in Equation (5).

With the first quality-reducing frame removed, the algorithm repeats, continually removing frames in descending ranked order until the new computed SNR does not increase when compared to the previous iteration. At this point, the highest SNR value is saved, and the algorithm stops processing and removing frames for the given test run.

It should be mentioned that the initial frame ordering and selection processes do not utilize frame registration techniques based on the peak of correlation prior to averaging the frames together. In the $H_0$ case where no object is present, there would assumedly exist numerous noise fluctuations. Therefore, frame registration in this scenario would have adverse effects, since noise spikes would be shifted and combined to form a false object.

To reiterate, the central goal of the algorithm lies in maximizing the SNR of each image and focuses on removing the frames that do not support this goal. Although the process of frame removal may seem counterproductive to increase the detection potential, averaging excessively noisy or distorted image data can have a negative effect on the SNR of the image due to the randomness of lower order atmospheric aberrations in short exposure images [11].

### ***Outlier Constraints***

While the original frame selection algorithm does not use registration techniques to remove specific frames prior to averaging, it does track the peaks of the convolution between the unaltered summed frames images and the expected PSF. If these peaks are outside the predetermined image stray limit, then the frame selection algorithm instead reverts to a traditional matched filter algorithm.

Additionally, the implementation of the original frame selection algorithm involved removing a maximum of 8 of the 10 frames, leaving a minimum of 2 short exposure frames for combination and subsequent analysis.

### ***Erroneous Distribution Assumption***

The results found by Becker suggest that the original frame selector outperforms the traditional matched filter used on the same data set [11]. However, the detection performances received from each algorithm were calculated based on a Gaussian data distribution assumption. The methodology behind utilizing this assumption is found Section 2.4. Although this is a common assumption for space object detection algorithms to hold, and is generally accurate, the output data using the frame selection algorithm does not produce data that follows a normal distribution. A sample histogram of the data from the original frame selection algorithm is shown in Figure 28.

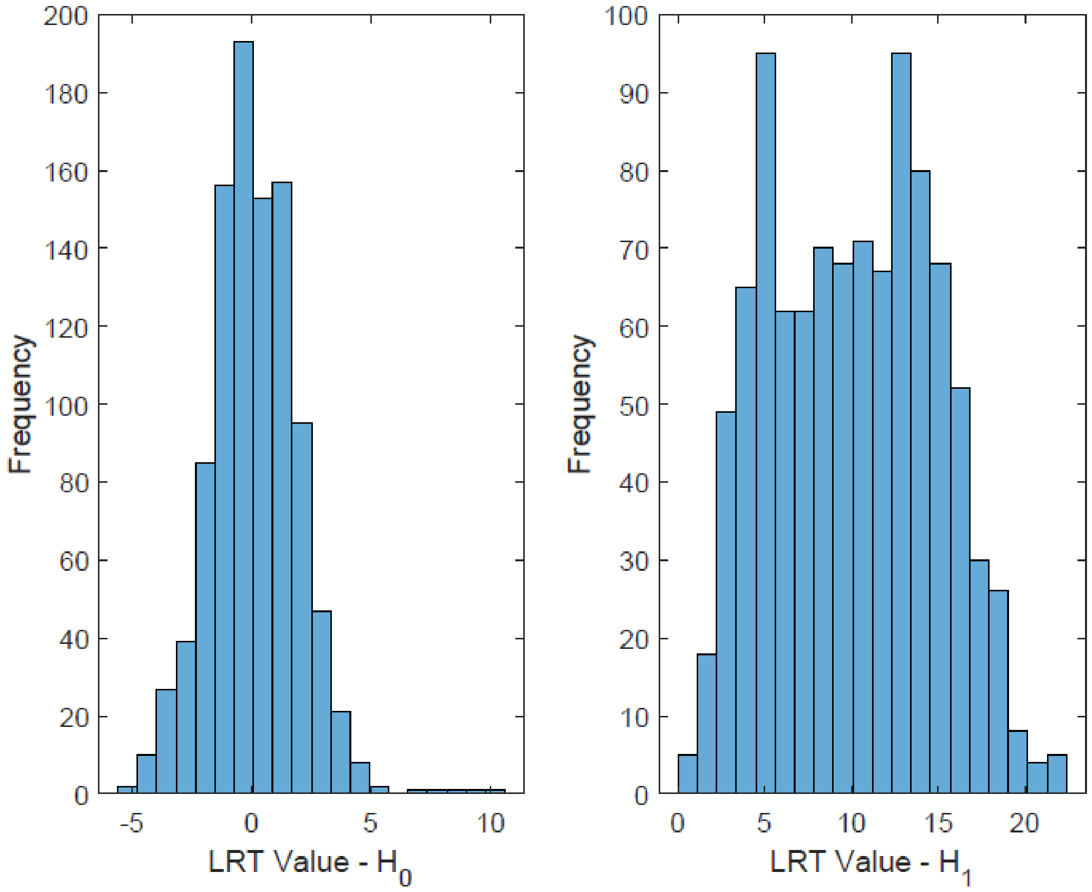

Figure 28. Original FSA histogram sample

In Figure 28, there are two maxima present in the histograms of the $H_1$ and $H_0$ output data, suggesting that the data may instead follow a variety of bimodal distribution. The displayed $H_0$ data does not show a second maxima, but the histogram's upper tail is present on all iterations, and sometimes results in a more defined second distribution. This invalidates the Gaussian distribution assumption and subsequently the reported detection performance results. The new frame selection algorithm discussed in the following section seeks to correct this issue.

### 4.3.2 New Algorithm

The newly proposed frame selection algorithm follows from the foundations established by the original algorithm. The preprocessing steps, as well as the frame selection and ordering techniques are identical, but the differences lie in the data distribution model and the additional incorporated  outlier constraints. In the following subsections, these two areas are explored in more detail.

#### ***Bimodal Gaussian Model***

As discussed in the latter part of Section 4.3.1, the original frame selector algorithm suffers from a faulty distribution assumption. Because the Gaussian assumption no longer holds, another method for generating LROC curves for analyzing the detection performance at low $P_{FA}$ rates must be determined. Crafting true ROC curves is still a valid option, but as mentioned in Section 2.3.6, with data sets of this size, limited processing power and subsequent long algorithm run times make calculating $P_{FA}$ rates of $10^{-4}$ or lower computationally impractical.

Utilizing a bimodal Gaussian distribution to calculate the $P_D$ and $P_{FA}$ rates across each threshold fixes the distribution assumption problem. The calculations for the new $P_D$ and $P_{FA}$ are like Equations (13) and (14) but use a summation of two different Gaussian distributions with differing SNR means and variances, instead of using simply a single Gaussian CDF combined with a single SNR mean and variance measurement. The two different distributions are determined by whether the algorithm used the frame selector algorithm result or reverted to the output of the matched filter, as mentioned in part of Section 4.3.1 and the following subsection. This new probability calculation method is shown in Equations (35) and (36), using the $H_1$ and $H_0$ data respectively. $N_1$ and $N_2$ are the number of frames that utilized either the frame selected value or the original summed frames correlator value, respectively, with the combined total number of frames equal to 1,000.

$$P_D = \frac{N_1}{N_1 + N_2} \int_{\tau}^{\infty} \frac{e^{\frac{-(\Lambda - \mu_{\Lambda_1})^2}{2\sigma_{\Lambda_1}^2}}}{\sqrt{2\pi\sigma_{\Lambda_1}^2}} d\Lambda + \frac{N_2}{N_1 + N_2} \int_{\tau}^{\infty} \frac{e^{\frac{-(\Lambda - \mu_{\Lambda_2})^2}{2\sigma_{\Lambda_2}^2}}}{\sqrt{2\pi\sigma_{\Lambda_2}^2}} d\Lambda \tag{35}$$

$$P_{FA} = \frac{N_1}{N_1 + N_2} \int_{\tau}^{\infty} \frac{e^{\frac{-(\Lambda - \mu_{\Lambda_1})^2}{2\sigma_{\Lambda_1}^2}}}{\sqrt{2\pi\sigma_{\Lambda_1}^2}} d\Lambda + \frac{N_2}{N_1 + N_2} \int_{\tau}^{\infty} \frac{e^{\frac{-(\Lambda - \mu_{\Lambda_2})^2}{2\sigma_{\Lambda_2}^2}}}{\sqrt{2\pi\sigma_{\Lambda_2}^2}} d\Lambda \tag{36}$$

In these equations, $\sigma_{\Lambda_1}^2$ and $\sigma_{\Lambda_2}^2$ represent the variance of the LRT outputs from the first and second distribution, respectively, while $\mu_{\Lambda_1}^2$ and $\mu_{\Lambda_2}^2$ denote the means. Aside from the new method of finding the probability arrays with the various threshold values, the rest of the process for constructing the new, accurate LROC curves is identical to the scheme used for the Gaussian model, described in Section 2.3.6.

### ***Additional Outlier Constraints***

In addition to the stray limit of the peak correlation of the summed frame images and the PSF that was used in the original frame selector, there are a few more added constraints imposed to increase the detection performance further. The intention of these additional constraints is to reduce the upper tail that appears in the histogram of the $H_0$ data. Because of the LRT formation of the algorithm, this upper tail interferes with the $H_1$ data, resulting in significant decreases in performance. These performance reductions were not seen in the original algorithm's published results because of the distribution assumption issue, but the negative effects are explored later in Section 4.5.3.

The first additional constraint imposes a limitation on the max number of frames that can be removed from the 10 total short exposure frames. Unrestricted frame removal without proper constraints was found to be a major source of the unwanted tail in the original $H_0$ data histogram. When no object is present, and solely noise spikes make up the peaks of the image, the algorithm had the tendency to make spurious detections on significantly distorted, noisy frames. Any frame limitation helps to reduce the $H_0$ histogram tail, but there is a balance, since this limit reduces $H_1$ histogram tails as well, which reduces the performance of the algorithm.

The other constraint enacted on the algorithm is another stray limit like the first one mentioned. However, instead of analyzing the peak correlation of the summed frame images, this stray limit is concerned with the correlation of the unselected, or removed frames with the PSF. This proves beneficial to outlier reduction because while a small number of frames may correlate well with the PSF in the $H_0$ case simply due to probability, but the remaining frames in the set will likely have zero correlation with the PSF. In the $H_1$ case, even the unselected frames will on average show some correlation with the PSF.

With the proper application of all these constraints, the upper tail in the $H_0$ histogram can effectively be removed. The implication of this is that there only exists an upper tail in the $H_1$ histogram, meaning that the new $P_{FA}$ calculation outlined in Equation (14) no longer is necessary, and can be reverted to Equation (36). Figure 29 denotes an example of the histograms that accompany the new algorithm. The settings of each of these constraints to empirically optimize the detection performance is discussed in the following subsection.

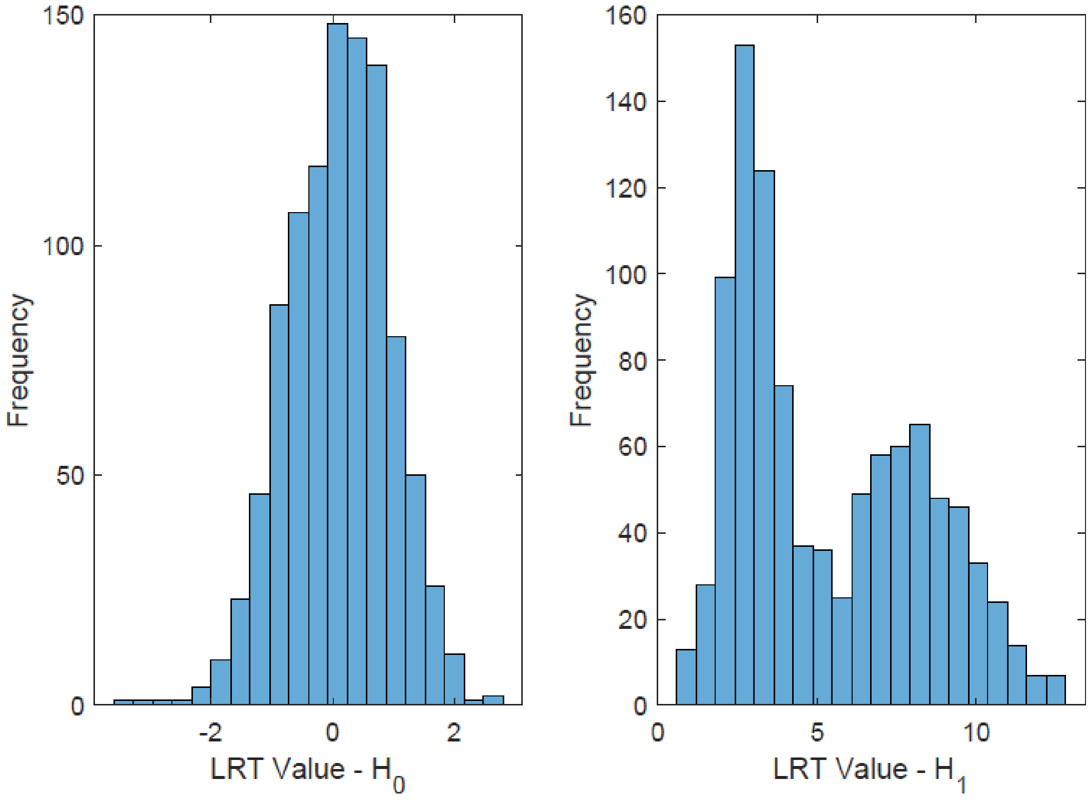

Figure 29. New FSA histogram sample

### *Optimal Settings*

To reiterate from the previous section, the three outlier constraints are the frame removal limit, the summed frame stray limit, and the unselected frames stray limit. To be beneficial to the performance of the frame selection algorithm, each of these constraints must be set to appropriate values. This subsection outlines the recommended values for each constraint, which are also the values used during the experiment portion of this chapter. To fully optimize these constraints, another study should be performed. The goal of this portion of the research is foremost to correct the distribution error from the original algorithm and show positive performance gains, but the settings may not be fully adjusted for peak performance.

The first constraint, the frame removal limit, was found to produce the best results when the limit left to 9. This means that in the most extreme cases, there is only a single short exposure frame for detection. This limit allows for the occasional “pristine” frame in the $H_1$ case to improve performance, while relying on the other constraints to keep the $H_0$ case from occasional spurious detections from noise spikes.

The summed frames and unselected frames stray limits were both limited to a value of 3, which means that the peak correlation of the frame with the PSF must remain within 3 pixels of centermost pixel. This limit includes both shifts in x and y-direction. If the max correlation value does not lie within this area, the frame selection algorithm results are reverted to the results of the standard summed frames correlator. This is again to protect against extreme outliers due to wind shift or poor instantaneous atmospheric conditions. The original algorithm implementation used a slightly different value for the summed frames stray limit that resulted in worse performance, but for the sake of comparison, this stray limit was kept constant across frame selection algorithms.

## 4.4 Experiment Description

Both simulated and experimental data sets are used to test the detection performance of the new frame selection algorithm against the spatial correlator and the original frame selection algorithm. Each data set is simulated or collected with the techniques and considerations discussed in Section 4.2. Specific descriptions of each data set, the experiment setup, and sample image frames are all included in Sections 4.4.1 and

4.4.2, for the simulated and experimental data, respectively. Finally, the foundations of algorithm implementation are reiterated in Section 4.4.3, followed by a concise summary of how the appropriate LROC curves were generated for each algorithm.

### 4.4.1 Simulated Image Data

The simulated data portion of the experiment is the primary method of comparing the new frame selection algorithm against the other two algorithms across a range of scenarios. There is a limited amount of available experimental image data that is usable in this research, so the data serves primarily as a validation method, while simulated data provides the means of testing. This section outlines specific parameters behind the creation of simulated data in this chapter, along with details about the experiment conducted to test the performance of each algorithm.

The objective of the simulated data is to achieve accurate modeling of the experimental data used in this chapter, which was obtained from a ground-based telescope performing object detection with short exposure integration times. Using the data modeling techniques in Section 4.2, 10,000 short exposure PSFs are created for each test iteration, which suffices to run 1,000 trials due to the input requirements of the frame selection algorithms. Each PSF is then used to generate a statistically accurate 32 by 32-pixel $H_1$ data frame, which contains a dim object in the center of the frame. The $H_0$ data frames are created using a random Poisson distribution at the predetermined level of background light.

The algorithms are analyzed in a series of test environments to exhaustively study the performance. Many of the parameters to create the test scenarios are shared with the experiment in Chapter III for consistency and clarity. The background light is varied across three separate levels to simulate night, day, and dusk or dawn conditions, and the average photon values match those used in Chapter III, as delineated in Table 3. Additionally, as mentioned in Section 4.2.4, the seeing parameter ranges based on the telescope operation time of day are shared across experiments. These values are outlined in Table 2. The distinctive parameter difference between the experiments lies in the simulated object PD SNRs used to test the algorithms [41]. Three separate object SNRs are explored for analysis, and the $\overline{K}$ values used to simulate these objects are calculated with Equation (33). The $\overline{K}$ values for each objects SNR are calculated using the parameters during a simulation with an $r_0$ equal to 6cm. Unlike Chapter III, however, the photon values are not held constant across each time of day. Another change is in the selected SNR values – the object SNRs used in this chapter, along with the $\overline{K}$ values associated with them are shown in Table 7.

Table 7. $\overline{K}$ values associated with each simulated object's point detector SNR across time of day

| **SNR** | **Night** | **Dusk/Dawn** | **Day** |
|---|---|---|---|
| **0.75** | 23 photons | 73 photons | 231 photons |
| **1** | 31 photons | 97 photons | 309 photons |
| **1.5** | 46 photons | 146 photons | 463 photons |

To summarize, 18 tests are conducted – arising from the three operation times, the three object SNRs, and the two different $r_0$ values, chosen as the lowest and highest values from the ranges provided in Table 2. Sample image frames from the test settings for each time of day with an object SNR of 1 and 1.5, and the higher seeing parameter are illustrated in Figure 30.

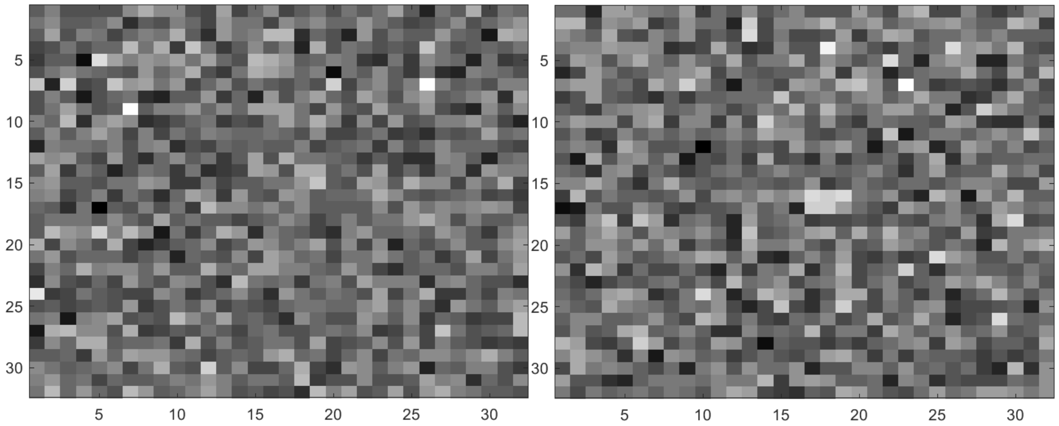

Figure 30. Night background light – simulated data frame with $r_0$ = 6cm, (left) SNR 1 and (right) SNR 1.5

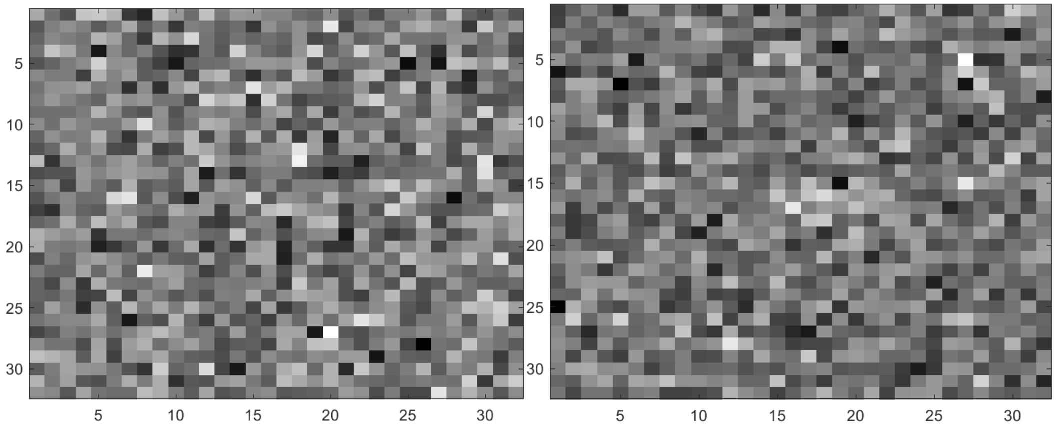

Figure 31. Dusk/Dawn background light – simulated data frame with $r_0$ = 5cm, (left) SNR 1 and (right) SNR 1.5

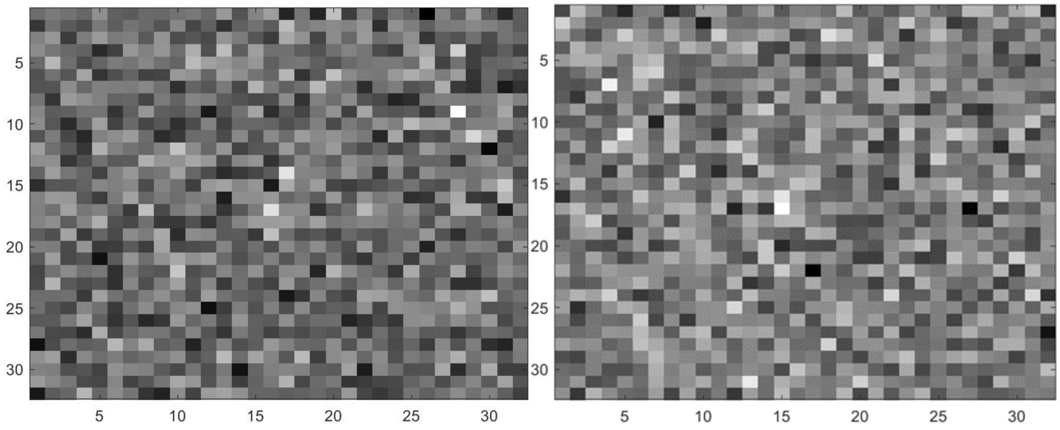

Figure 32. Day background light – simulated data frame with $r_0$ = 4cm, (left) SNR 1 and (right) SNR 1.5

Lastly, in addition to the traditional tests described in this section, a single series of 3 tests is conducted – one each for night, dusk/dawn, and day background light conditions. The point of these tests is to compare the algorithms with every parameter constant aside from simulated background light. The $\overline{K}$ value is held constant at 150 photons, and the $r_0$ value is simulated as 3cm, which is a reasonable seeing parameter for all the different backgrounds, as outlined by the ranges in Table 2.

### 4.4.2 Experimental Image Data

As mentioned in Section 4.4.1, simulated data provides the main means of testing the algorithms, while experimental image data serves as primarily a validation method. The experimental images that are accessible and relevant to this research include two data sets whose origination details are discussed in Section 4.2.2. These data sets are the result of a small aperture telescope capturing two different dim objects in relative proximity to each other. These objects are windowed from the original 100 by 100-pixel frame so that the centers of the objects are aligned with the centermost pixel of their own individual 32 by 32-pixel frame. Background data with no objects present are collected from nearby empty areas of the frame. There are 1,000 frames of the $H_1$ and $H_0$ case for each space object collected in this manner, which, based on the 10 frame input requirements of the frame selection algorithms, is enough for 100 trials.

Although statistical significance is hard to draw from a small sample of trials, the results are compared against those of the simulated data for validation. Sample individual image frames from both $H_1$ and $H_0$ hypotheses for each data set are included in Figure 33 and Figure 34 for visualization.

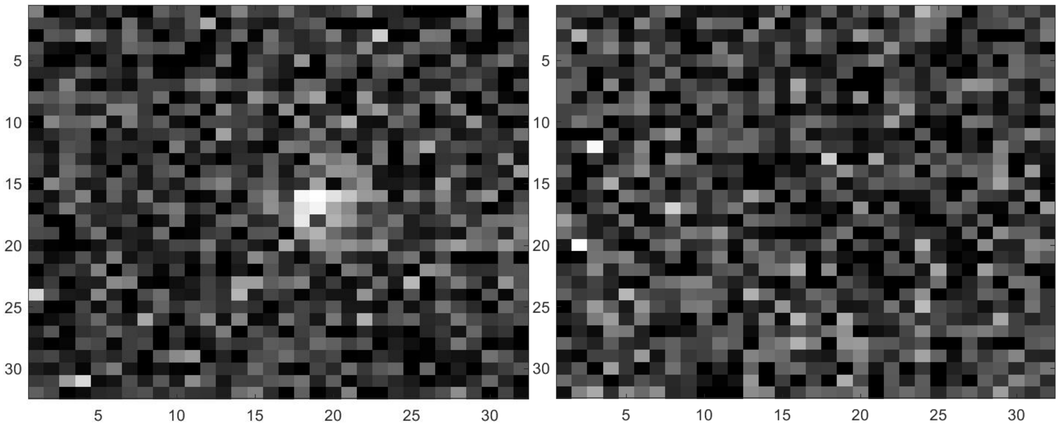

Figure 33. Individual frames for experimental data set of Polaris B with (left) $H_1$ and (right) $H_0$

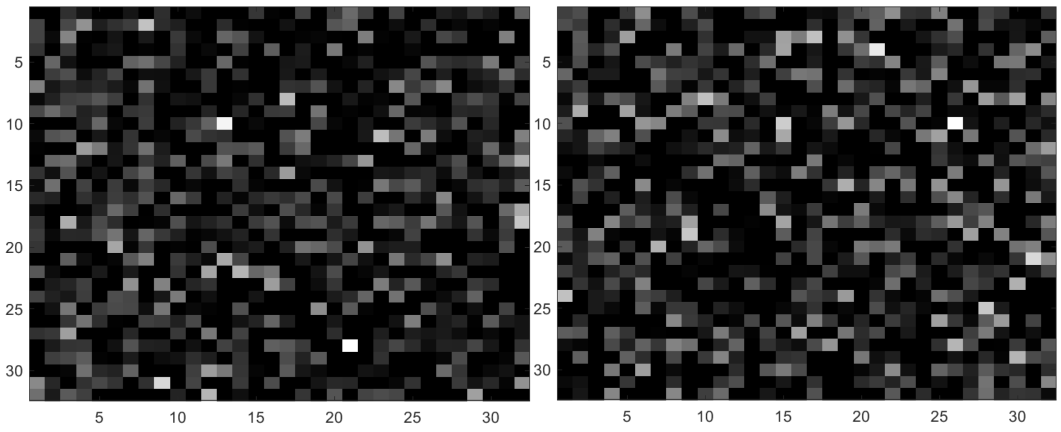

Figure 34. Individual frames for experimental data set of the dim star with (left) $H_1$ and (right) $H_0$

The $H_1$ data in Figure 33 is clearly visible, so the testing of this data set is trivial for the algorithms. The true importance of detection algorithms is in the testing of data sets such as the one shown in Figure 34 of the other dim star in relative proximity to Polaris B. To the human eye, neither the $H_0$ nor $H_1$ scenes appear to host any space object, but with further analysis, detection may be possible.

### 4.4.3 Algorithm Application

The three algorithms tested in this chapter are the spatial correlator and the old and new frame selection algorithms. The spatial correlator is implemented in MATLAB using Equation (5) and the frame selections algorithms are realized with the techniques and methods described in Section 4.3. Each algorithm utilizes the same data set, which for each trial is a set of 10 short exposure image frames. For the simulated portion of the experiment, data formulation, noise, atmospheric turbulence, and other optical models are employed according to Section 4.2. The simulated data models are closely aligned to those of the experimental data set by design, so that comparison between results has significance. Additionally, like the experiment in Chapter III, each detection method does not have prior knowledge about the existence of space objects in the image frames.

Aside from basic operation and modeling, a key difference between each algorithm is the method behind determining an accurate estimation of performance. All performance comparisons are shown through LROC curves, but the procedure behind generating the $P_D$ and $P_{FA}$ values for each threshold and creating these curves is unique. The spatial correlator data follows a normal distribution, so the commonly used Gaussian LROC curve outlined in Chapter II suffices for this algorithm. However, as outlined in Section 4.3.1, the original frame selection algorithm suffered from an erroneous distribution assumption. In order to rectify the results, both the $H_1$ and $H_0$ data sets are assumed to follow a bimodal Gaussian assumption, utilizing Equations (35) and (36) as substitutions for the original Equations (13) and (14) used to determine $P_D$ and $P_{FA}$. The new frame selector, also delineated in Section 4.3.2, utilizes multiple outlier constraints to mitigate the upper tail in the $H_0$ data set, allowing for the use of a simple Gaussian assumption under this hypothesis. The $H_1$ data still is assumed to follow a bimodal Gaussian, so the LROC curve is determined through a combination of Equations (35) and (14).

Lastly, a Lilliefors test was conducted in a dusk/dawn scenario with readout noise included to verify the distribution assumptions of each algorithm. Each test was performed based on data combined from 5 trials, with the p-values shown in Table 8. Generally, a p-value nearing 0.05 or greater indicates that the baseline hypothesis should not be rejected with strong certainty. Therefore, the selected distribution assumptions for the new frame selection algorithm and the summed frames correlator algorithm are shown to be accurate, while the p-values associated with the original frame selector indicate that the distribution may not be ideal, or that more data is needed.

Table 8. Lilliefors normality test results for the correlator and frame selectors described in Chapter IV

| **Algorithm** | **$H_0$ p-value** | **$H_1$ p-value** |
|---|---|---|
| Summed Frames Correlator | .2934 | .2227 |
| Original Frame Selector | .0083 | .001 |
| New Frame Selector | .0478 | .0444 |

### 4.5 Results

The LROC curves received from performing the simulated data experiment outlined in Section 4.4.1 are presented in Section 4.5.1, along with a performance analysis discussion between algorithms. Section 4.5.2 includes the LROC curves from the experimental data experiment described in Section 4.4.2. Lastly, Section 4.5.3 shows the performance results of the original frame selection algorithm with a Gaussian distribution versus with the bimodal Gaussian distribution to illustrate the issue of misreporting results because of faulty distributions.

### 4.5.1 Simulated Data LROC Curve Analysis

This subsection offers the results of the simulated data experiment in the form of LROC curves of each test scenario. These findings are further divided into four sections. Three of these are night, dusk or dawn, and day, designating the simulated operation time of the receiving ground-based telescope, and the fourth section consists of the experiment described in the latter part of Section 4.4.1 related to keeping a constant photon value for comparison across background light levels. Each divided section consists of an explanation of specific parameters used in each test, LROC curves to show the results, and a relative analysis of each algorithm.

#### ***Night***

The results for each algorithm in a nighttime scenario are shown in Figure 35, Figure 36, and Figure 37. For these tests, the selected $r_0$ values are 3cm and 6cm, which are the lowest and highest seeing parameters for the night setting from the ranges shown in Table 2. The left side of each figure depicts the higher $r_0$ value, and the right side the lower $r_0$ value, with all other parameters held constant.

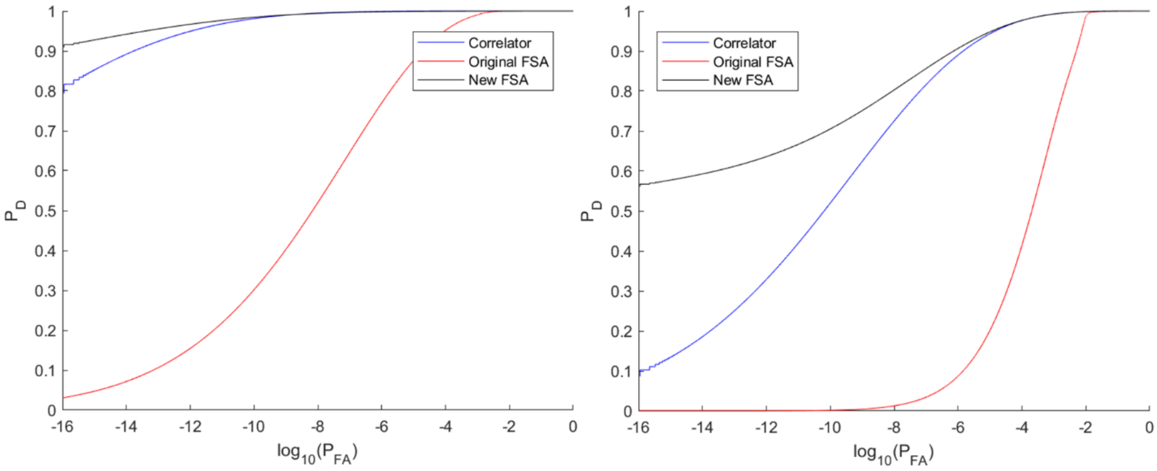

Figure 35. LROC curve comparison – Night scenario, object PD SNR 1.5 with (left) $r_0$ = 6cm and (right) $r_0$ = 3cm

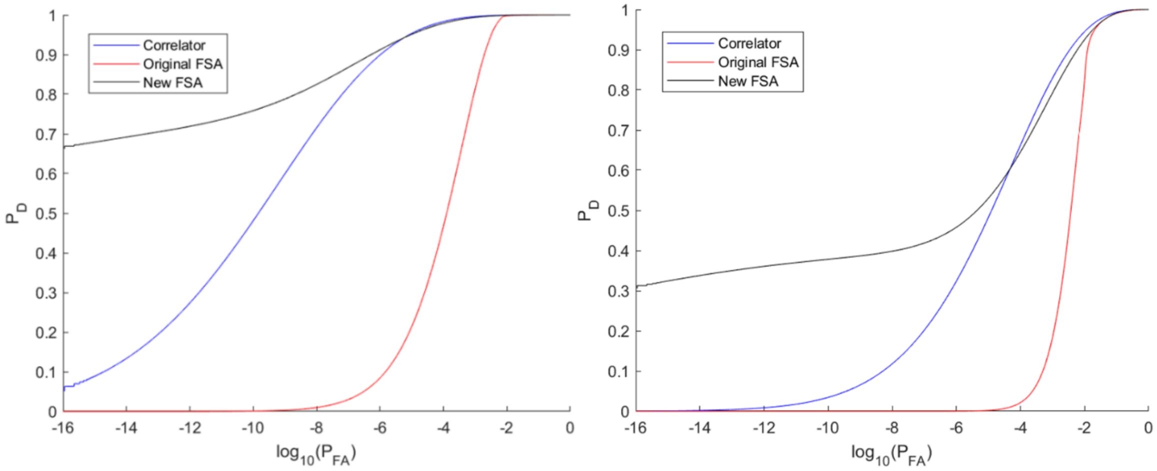

Figure 36. LROC curve comparison – Night scenario, object PD SNR 1 with (left) $r_0$ = 6cm and (right) $r_0$ = 3cm

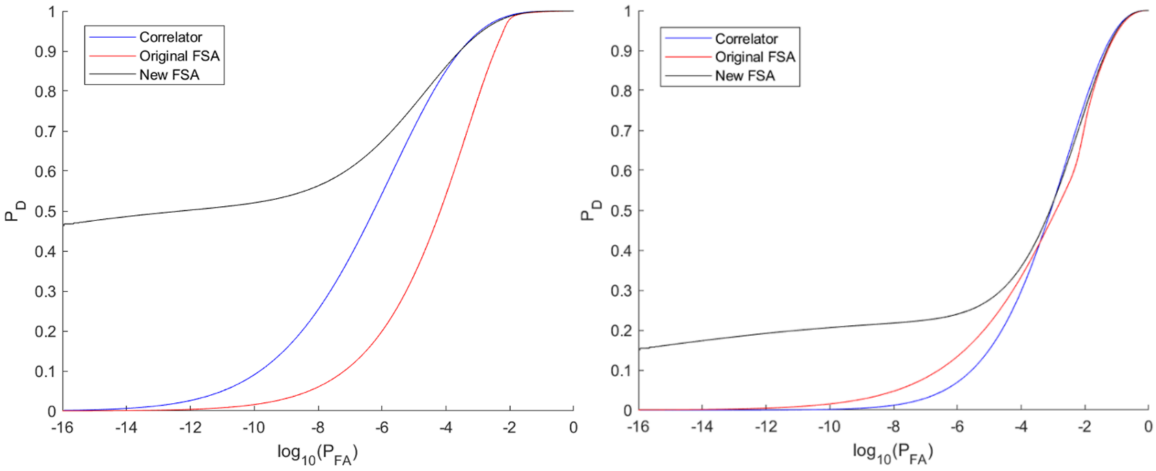

Figure 37. LROC curve comparison – Night scenario, object PD SNR 0.75 with (left) $r_0$ = 6cm and (right) $r_0$ = 3cm

From these figures, the reasonable conclusion is that in a nighttime, low-SNR object detection scenario, the new frame selection algorithm outperforms both the spatial correlator and original frame selection algorithms at low $P_{FA}$ rates. For the 1.5 SNR object in Figure 35, the new frame selection algorithm shows a 0.5-12% increase in $P_D$ over the spatial correlator and a 60-75% increase over the original frame selection algorithm at a fixed $P_{FA}$ of $10^{-9}$, varying by $r_0$ value. The gap in performance widens at lower $P_{FA}$ thresholds for every test iteration, but for the purpose of uniform comparisons, a $P_{FA}$ of $10^{-9}$ will be the standard used for analysis.

As the SNRs of the objects decrease, the performance of the new frame selection algorithm appears to drop off much slower than that of the other algorithms, as well. In Figure 36 with the object SNR of 1, the new frame selection algorithm boasts an 18-28% increase in $P_D$ over the spatial correlator and a 37-78% increase over the original frame selection algorithm at a $P_{FA}$ of $10^{-9}$. When the object SNR is decreased to 0.75, the $P_D$ increase over the spatial correlator rises to 20-33%, and the increase over the original frame selection algorithm decreases to 18-47%. The new frame selection algorithm does exhibit some interest characteristics at high $P_{FA}$ rates, with the occasional crossing of the LROC curves between the other algorithms. However, at low $P_{FA}$ rates, the algorithm appears to always outperform the other two algorithms.

### *Dusk/Dawn*

The results for each algorithm in a dusk or dawn scenario are shown in Figure 38, Figure 39, and Figure 40. For these tests, the selected $r_0$ values are 2cm and 5cm, which are the lowest and highest seeing parameters for the dusk and dawn setting from the ranges shown in Table 2. Again, the left side of each figure depicts the higher $r_0$ value, and the right side the lower $r_0$ value, with all other parameters held constant.

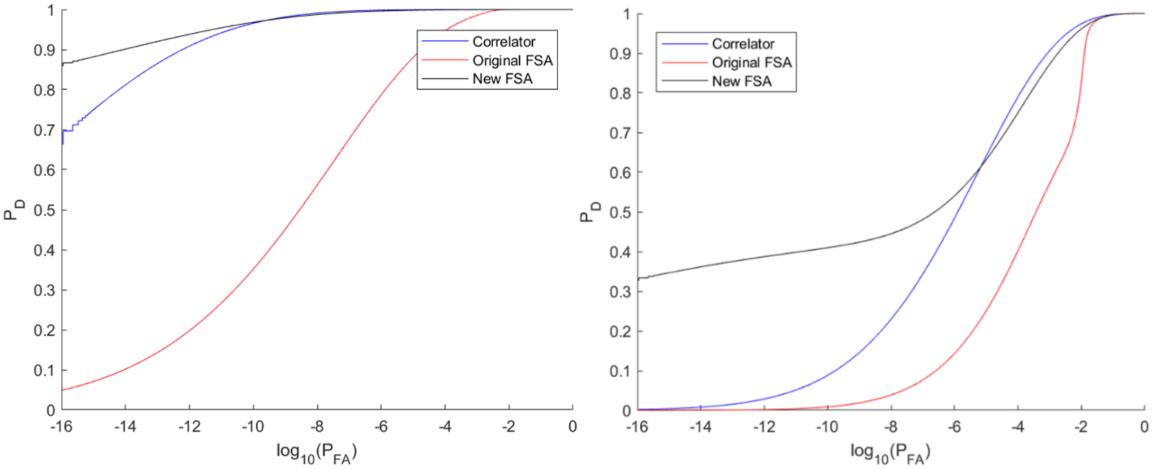

Figure 38. LROC curve comparison – Dusk/dawn scenario, object PD SNR 1.5 with (left) $r_0$ = 5cm and (right) $r_0$ = 2cm

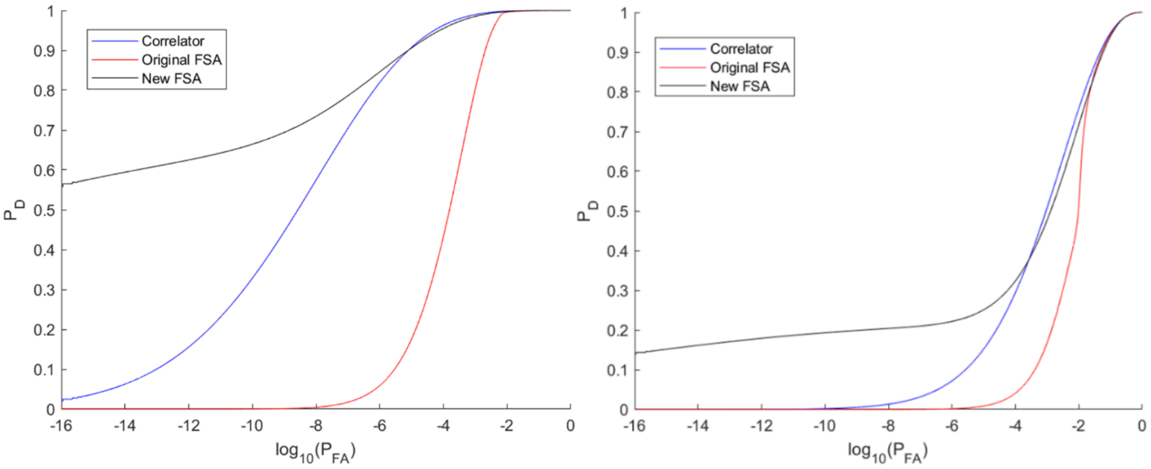

Figure 39. LROC curve comparison – Dusk/dawn scenario, object PD SNR 1 with (left) $r_0$ = 5cm and (right) $r_0$ = 2cm

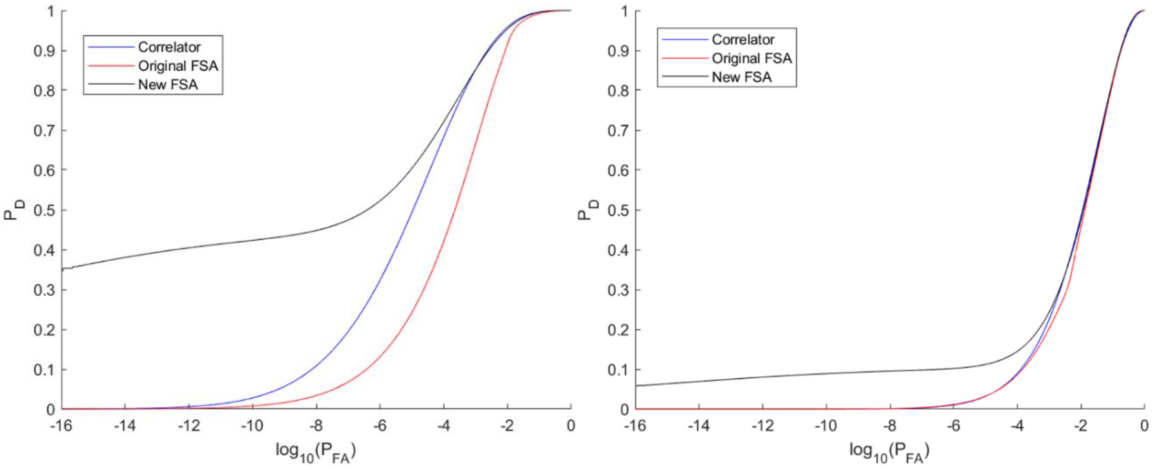

Figure 40. LROC curve comparison – Dusk/dawn scenario, object PD SNR 0.75 with (left) $r_0$ = 5cm and (right) $r_0$ = 2cm with

These figures show that in a dusk or dawn, low-SNR object detection scenario, the new frame selection algorithm again outperforms the spatial correlator and significantly beats the original frame selection algorithm at low $P_{FA}$ rates. For the 1.5 SNR object shown in Figure 38, the new frame selection algorithm shows a 0.5-25% increase in $P_D$ over the spatial correlator and a 38-60% increase over the original frame selection algorithm at a fixed $P_{FA}$ of $10^{-9}$, varying by $r_0$ value. In Figure 39 with the object SNR of 1, the new frame selection algorithm displays an 19-20% increase in $P_D$ over the spatial correlator and a 20-68% increase over the original frame selection algorithm at a $P_{FA}$ of $10^{-9}$. When the object SNR is decreased to 0.75 in Figure 40, the $P_D$ increase over the spatial correlator changes to 10-32%, and the increase over the original frame selection algorithm decreases to 10-40%. Overall, these results are very comparable to the results from the nighttime scenario.

***Day***

The results for each algorithm in a daytime scenario are shown in Figure 41, Figure 42, and Figure 43. For these tests, the selected $r_0$ values are 1cm and 4cm, which are the lowest and highest seeing parameters for the day setting from the ranges shown in Table 2. The left side of each figure depicts the higher $r_0$ value, and the right side the lower $r_0$ value, with all other parameters held constant.

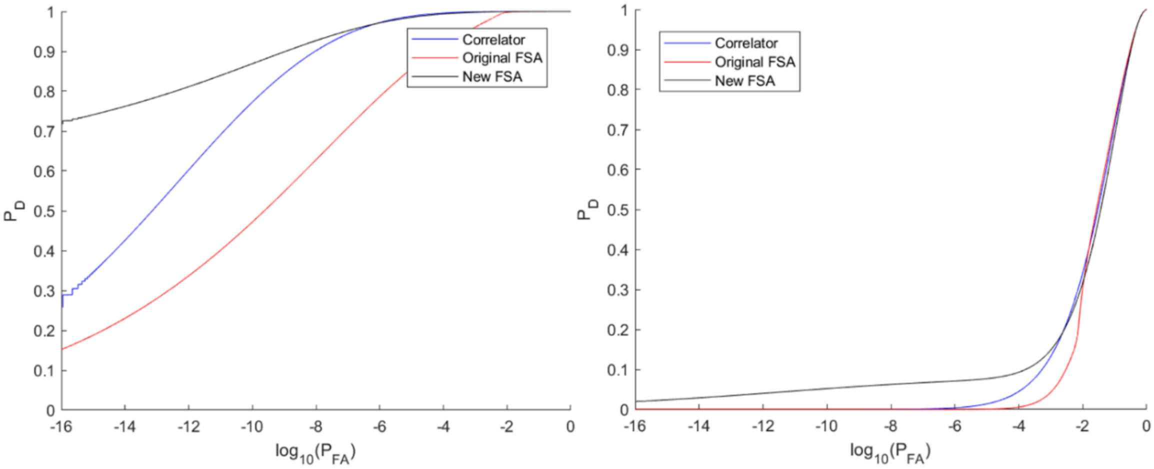

Figure 41. LROC curve comparison – Day scenario, object PD SNR 1.5 with (left) $r_0$ = 4cm and (right) $r_0$ = 1cm

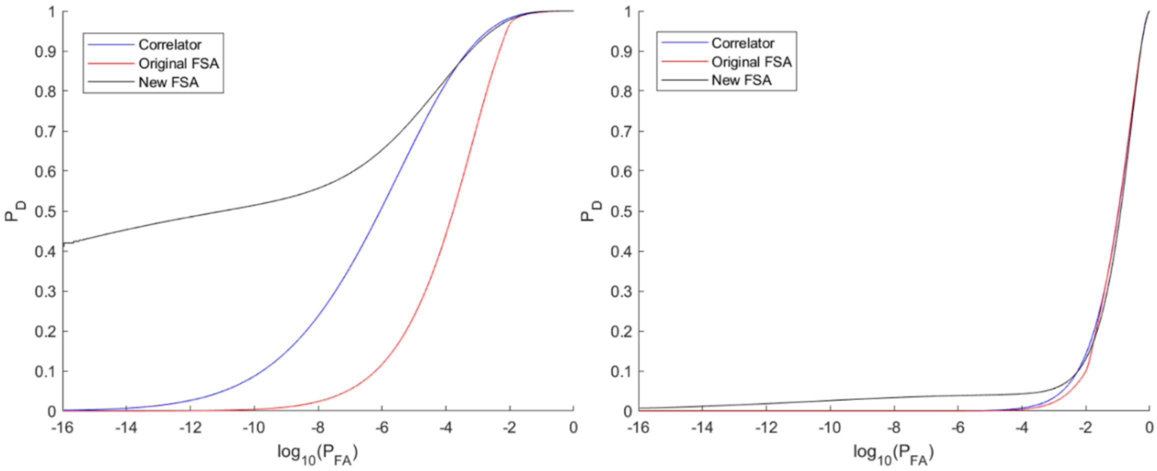

Figure 42. LROC curve comparison – Day scenario, object PD SNR 1 with (left) $r_0$ = 4cm and (right) $r_0$ = 1cm

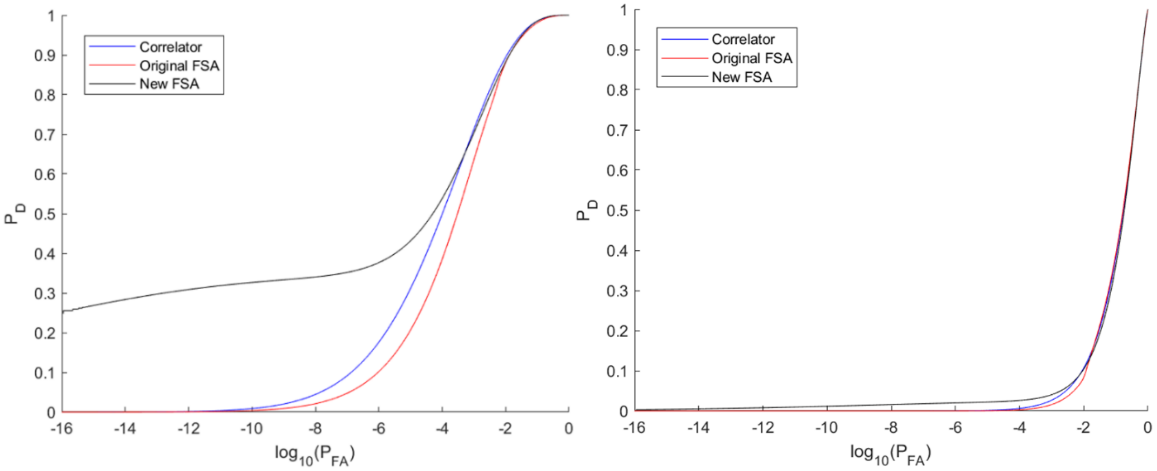

Figure 43. LROC curve comparison – Day scenario, object PD SNR 0.75 with (left) $r_0$ = 4cm and (right) $r_0$ = 1cm

These figures analyze the daytime time operation, demonstrating that in most conceivable low-SNR object detection scenarios, the new frame selection algorithm outperforms the spatial correlator and significantly beats the original frame selection algorithm at low $P_{FA}$ rates. For the 1.5 SNR object shown in Figure 41, the new frame selection algorithm shows a 5-6% increase in $P_D$ over the spatial correlator and a 6-35%

increase over the original frame selection algorithm at a fixed $P_{FA}$ of $10^{-9}$, varying by $r_0$ value. In Figure 42 with the object SNR of 1, the new frame selection algorithm displays an 3-34% increase in $P_D$ over the spatial correlator and a 3-50% increase over the original frame selection algorithm at a $P_{FA}$ of $10^{-9}$. Finally, when the object SNR is decreased to 0.75 in Figure 43, the $P_D$ increase over the spatial correlator changes to 1-29%, and the increase over the original frame selection algorithm decreases to 1-30%.

### *Background Light Comparison*

The purpose of this subsection is to compare the performance of the algorithms with all parameters held constant except for the background light. The seeing parameter is held constant at 3cm, and the $\overline{K}$ value is held constant at 150 photons – the only change is the background is changed according to the light level differences between day, dusk/dawn, and night, as outlined in Table 3. The results of the three tests are shown in Figure 44.

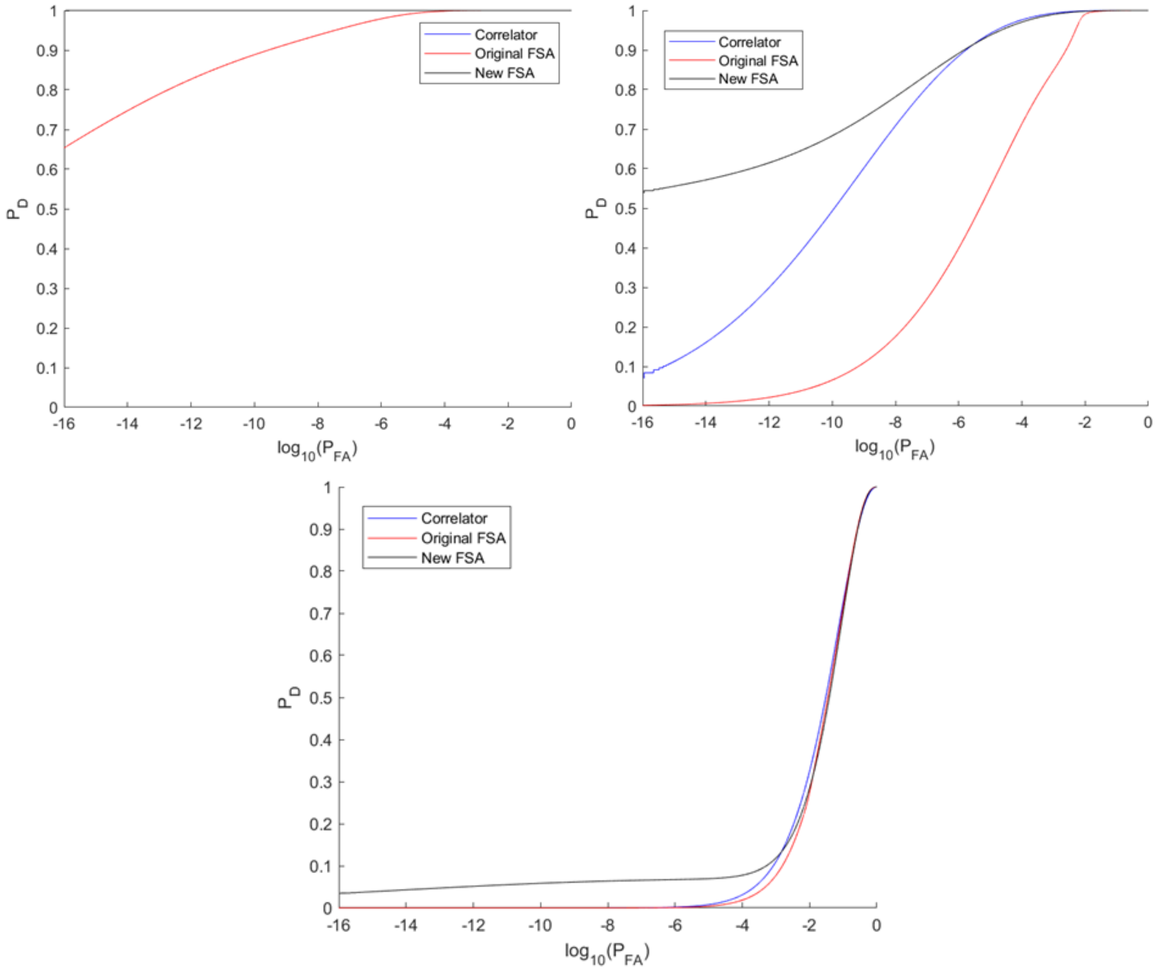

Figure 44. LROC curve comparison – Constant photon count of $\overline{K}$ = 150, $r_0$ = 3cm with differing background light: (top left) Night (top right) Dusk/Dawn and (bottom) Day

As expected, the lower the background light present in the data formation of the algorithm, the better the algorithms perform. Keeping the photon level constant results in significantly better performance during the night, and much harder detection during the daytime. However, the $P_D$ of the dusk/dawn iteration still demonstrates a relatively high detection capability of 74% at a $P_{FA}$ of $10^{-9}$, which may lend to the possibility of extending the hours of telescope detection time to include some lower light hours of the day.

### 4.5.2 Experimental Data LROC Curve Analysis

This subsection displays the results of the experimental data experiment described in Section 4.4.2 in the form of LROC curves of the two data sets. A brief analysis of the results is also included. The results from using the detection algorithms to analyze the Polaris B data set is shown in Figure 45.

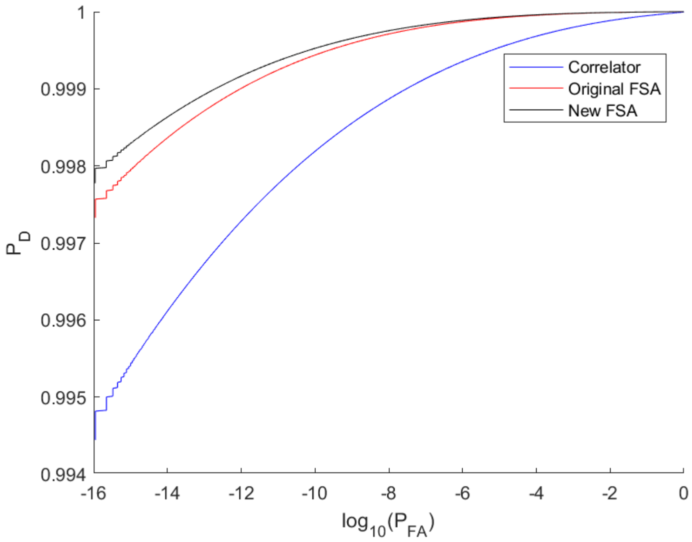

Figure 45. LROC curve comparison from experimental data set – Polaris B

As mentioned in Section 4.4.2, the relative SNR of Polaris B compared to the background makes detection trivial for developed algorithms such as the ones used in this chapter of the research. Unsurprisingly, each algorithm, including the standard spatial correlator, reached nearly 100% $P_D$ across all $P_{FA}$ thresholds.

The second data set, created from the dim star near Polaris B, proved to be much more useful in determining the algorithms' relative performance. The results from this data set are shown in Figure 46.

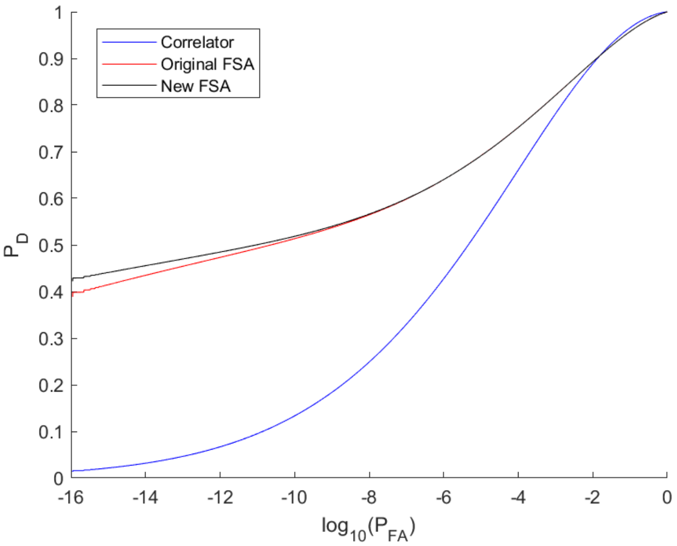

Figure 46. LROC curve comparison from experimental data set – dim star

From Figure 46, both frame selection algorithms show a 33% increase in $P_D$ over the spatial correlator at a fixed $P_{FA}$ of $10^{-9}$. The difference in performance becomes more pronounced at even lower $P_{FA}$ rates, as well. At a $P_{FA}$ of $10^{-16}$, the spatial correlator has a $P_D$ of only 2%, while the original FSA and new FSA have a reported $P_D$ of 40% and 44%, respectively.

Unfortunately, because of the limited amount of experimental data available, the significant detrimental effects of the occasional outlier frame were not captured. Therefore, the original and new FSAs appear to perform nearly the same, which was not reported by the simulated data results.

From 18 separate simulated data trials that included readout noise to mimic the experimental data as accuracy as possible, the average number of frames per 1,000 that made up an upper tail in the $H_0$ histogram of the basic frame selector was 11.778, with a standard deviation of 2.84. Therefore, receiving zero spurious detections in a sample size of only 100 frames is statistically plausible. If there had been more than 100 trials for each data set, the results from the simulated data lead to the assertion that a more distinguishable difference would have been seen in the experimental data results, as well.

### 4.5.3 Erroneous Gaussian Assumption Impact

The perceived performance of the algorithm can be drastically changed under a faulty assumption for the data. As mentioned in Section 4.3.1, the original frame selection algorithm assumed the output data followed a normal distribution, while it actually appears to adhere to a bimodal distribution. LROC curves are created based on this assumption, so to illustrate the potential effects of using different assumptions, both curves are plotted in Figure 47 using the same data.

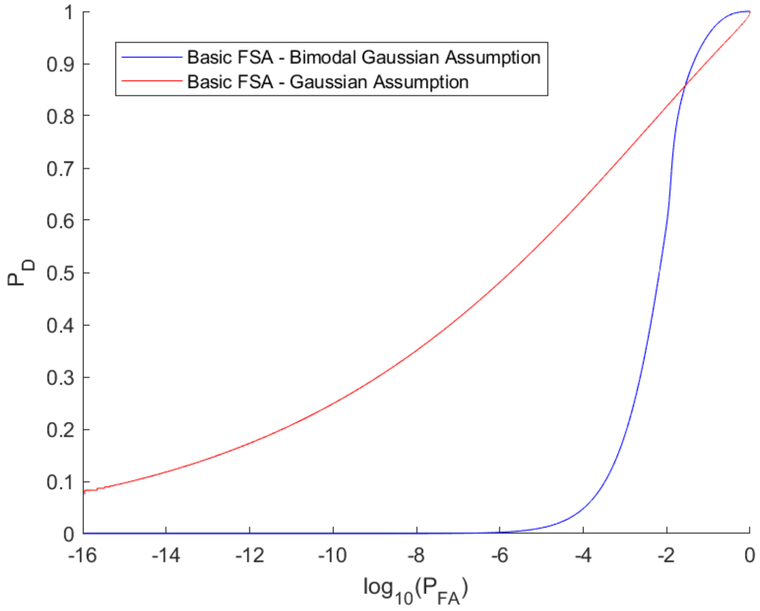

Figure 47. LROC Curves with data assumed Gaussian versus bimodal Gaussian

At a $P_{FA}$ of $10^{-9}$, utilizing the Gaussian assumption yields a $P_D$ that is 29% greater than when the bimodal Gaussian assumption is used. Unfortunately, these gains are false, since the data follows a bimodal distribution.

### 4.6 Chapter Conclusion

This chapter focuses on improving the detection performance of ground-based telescopes for small or dim space objects in short exposure data. The new algorithm proposed is a post-processing algorithm based on frame selection of a given number of frames obtained from a small aperture telescope operating under short exposure integration times. The concept stems from a previously employed frame selection algorithm, and the results of the new algorithm are compared against both the original algorithms results and those of a spatial correlator. Each algorithm is implemented in MATLAB and compared using LROC curves.

The research in this chapter focused on analyzing the $P_D$ of the algorithms at a low $P_{FA}$ rate of $10^{-9}$, since producing a high number of spurious detections is not efficient. The new frame selection algorithm at this low $P_{FA}$ threshold outperformed both the spatial correlator and the original frame selection algorithms across every test conducted. The performance increases in the simulated data appeared much more defined than the experimental data results and indicated that the spatial correlator beat the original frame selector for most tests.

However, the experimental data showed the original frame selector beat the spatial correlator and performed nearly identically to the new frame selection algorithm. It is expected that this is due to the lack of repetitions and limited amount of data. The simulated data results project that if more than 100 trials of experimental data were available, outlier frames would have been present, which are the reason the performance of the original frame selection algorithm suffered. Overall, the conclusion is that the new frame selection algorithm attained higher $P_D$ than both the original frame selection algorithm and the spatial correlator at a $P_{FA}$ rate of $10^{-9}$ across all test scenarios and operation times.

# V. Conclusion

## 5.1 Chapter Overview

This chapter recapitulates the research results of this thesis obtained from the experiments performed in Chapter III and Chapter IV, and addresses the work completed to satisfy the overarching research goals proposed in Chapter I. Prospective continuation research to develop each topic covered is also included.

## 5.2 Research Goals and Conclusions

The predominant goal of the research in this thesis was to enhance the capabilities of existing ground-based telescopes to detect dim or small objects through the development and analysis of various space object detection algorithms. The purpose of these advancements is to further the achievable performance of the SDA detection mission, with the possibility of future implementation within the DoD and other astronomical communities. Chapter I raised three research questions related to the specific detection performance areas pursued. The work completed and experiments conducted in this thesis all aimed to sufficiently answer the questions posed. This section provides a detailed understanding of the extent to which each research goal was accomplished, along with a review of the key results.

*1. Will a Fourier domain point detector, as opposed to a traditional spatial point detector, yield detection performance advantages when compared to correlation-based algorithms?*

This research question was pursued exclusively in Chapter III. This chapter delved into an object detection algorithm that was developed in a previous dissertation that utilizes the real component of the Fourier transform of long exposure spatial images retrieved from a ground-based telescope. The algorithm was formed through determining statistical models for the data under both the $H_0$ and $H_1$ hypotheses, and crafting a LRT based on a Gaussian data distribution. The performance of this FPD algorithm is compared against a spatial point detector algorithm and a spatial correlator or matched filter algorithm using a simulated large aperture telescope and surrounding environment in MATLAB.

The work completed in the dissertation that conceived the FPD algorithm investigated the performance against spatial point detector, finding a 40% improvement in the $P_D$ at a $P_{FA}$ of $10^{-9}$. Furthermore, the original work compared the FPD algorithm against a spatial correlator that was supplied either a true PSF or an incorrect PSF, finding that the performance comparisons were very similar, or resulted in a $P_D$ increase of 34%, respectively. However, during the initial stages of the research in this thesis, these results, specifically those between the FPD and the spatial correlator, were found to be overstated, and it was determined that new testing should be performed to rectify these published conclusions.

The experiment conducted in Chapter III analyzed three different space object SNRs, across three different times of day, with two different seeing parameters for each combination. The spatial correlator was analyzed with three different PSFs supplied: the true PSF, the incorrect PSF with an $r_0$ off by a factor of 1.5, and the incorrect PSF with an $r_0$ off by a factor of 2. The shape of the PSF is commonly unknown and must be estimated based on a telescope's optics and the measured atmospheric turbulence. In the tests conducted, the PSF incorrect by a factor of 1.5 was considered conceivable error, while the PSF wrong by a factor of 2 was deemed the worst-case estimation with current PSF estimation techniques. The overall determination was that the FPD beat the spatial point detector, as expected, but the spatial correlator significantly outperformed the FPD across all test combinations, even when supplied the worst-case PSF. Therefore, although the FPD has the advantage over the spatial correlator of requiring no PSF knowledge to function, further development of the current algorithm to attempt to beat a correlation-based scheme was determined to be futile.

*2. In detection scenarios where short exposure imaging is used, will frame selection increase the ability of detecting objects over a simple summation of multiple frames?*

There exists an interest in the SDA community to develop the ability to image from ground-based telescopes during daylight. Because of the bright backgrounds inherent in these scenarios and the limited depth of modern CCD pixels, short exposure imaging becomes necessary. Many of the other engineering challenges associated with this endeavor are outside the scope of this research, but the work completed in Chapter IV aims to develop a short exposure object detection algorithm that can be used to process this type of collected data. Chapter II outlines other current short exposure imaging techniques, but these are primarily used for image reconstruction or enhanced resolution and are not designed for broad area detection. Many detection techniques utilize the summation of a series of short exposure images to create a single long exposure image which can be correlated with the measured PSF of the optical system. The algorithm developed in Chapter IV, however, analyzes potential performance gains from only combining select frames from a larger set.

The new frame selection algorithm explored in this chapter stems from an earlier iteration of the algorithm developed as part of a published dissertation [11]. A key distribution error was found in the original algorithm's published results, which led to the need for rectification and additional development. Each algorithm stems from the same foundational concepts, with additional constraints and fixed assumptions being the main differences between the old and new versions. Both frame selection algorithms utilize a set of 10 short exposure frames, following a recursive approach that removes frames in a descending order based on which most positively affect the SNR of the image. Additionally, the two algorithms also correlate the remaining frames with the system's PSF to retrieve the output data which is analyzed with a LRT. The performances of the original and new frame selection approaches are compared against those of a spatial correlator to determine the viability of frame selection in this context.

Simulated and experimental data were both analyzed in separate experiments. The experimental data used was collected with a small aperture telescope during dusk and consisted of two data sets windowed from a larger frame, each with a known star at the center of the image: one brighter star, Polaris B, and another proximate dimmer star. The simulated data was created in MATLAB and designed to mimic the physical setup present during the collection of the experimental data, while also creating statistically accurate atmosphere and noise effects. This data was tested under day, dusk/dawn, and night conditions by varying the average background level. Multiple seeing parameters and space object SNRs were chosen to exhaustively test the algorithms.

In the simulated data experiment, the performance of the new frame selection algorithm achieved superior $P_D$ at low $P_{FA}$ rates across all test scenarios compared to both the original frame selector and the summed frames spatial correlator. The original frame selector suffers from occasional spurious detections in the $H_0$ case. Because the frame selectors are LRT-based algorithms, an upper tail in the histogram of the $H_0$ data results in significant performance decreases. Therefore, the results from the simulated data tests show that the original frame selector performed magnitudes worse than both other algorithms. With the additional constraints imposed by the new frame selector, the upper tail in the $H_0$ case was mitigated, and the algorithm was able to outperform the spatial correlator. Overall, these results show that when short exposure images are selectively combined and the data is appropriately protected against outliers, substantial improvements to the detection performance is achieved.

The available experimental data was limited to 1,000 $H_1$ and $H_0$ image frames for each data set, which is only enough for 100 trials. The simulated data, in comparison, created data for 1,000 trials per run. The spurious detections that occasionally occurred in the $H_0$ simulated data due to noise spikes and resulted in significantly lowered performance were not present in the obtained experimental data. Because of this the new frame selection algorithm only performed slightly better than the original frame selection algorithm.  However, the results did show unequivocally that the new frame selection algorithm significantly outperformed the spatial correlator.

*3. What variables or constraints should be explored to optimize this frame selection algorithm?*

The final constraints decided on to achieve the best performance in the new frame selection were discussed during the algorithm’s development in Chapter IV. The main goal of the modifications or additions of constraints in this chapter was to mitigate the upper tail present in the histogram of the $H_0$ data, while maximizing the upper tail in the histogram of the $H_1$ data. An upper tail in the $H_0$ case results in overlap between each case when the LRT is implemented, resulting in a significant decrease in performance. As mentioned, this is the key issue that the original frame selection algorithm suffered from.

Numerous ideas were attempted in the early stages of this research to increase performance, including frame selection based on power in the frequency domain, and a stray limit imposed by the selected frames. However, the concluding determination was that frame ranking based on SNR, along with a slight modification of the frame removal limit and the addition of a stray limit based on the unselected frames produced empirically superior results.

The execution of the original frame selection algorithm allowed for a maximum of 8 frames of the total set of 10 frames to be removed. The new frame selection algorithm modified this to allow for up to 9 frames to be removed. This process actually increased the upper tails in both the $H_1$ and $H_0$ output data histograms, but coupled with the stray limits of both the total summed frames and the unselected frames correlated with the system's PSF, the spurious detections previously made in the $H_0$ case were eliminated.

## 5.3 Future Work

In the effort to detect smaller and dimmer space objects, improvements in many subject areas will need to be made, including object detection algorithms, the focus of this research. Continued advancements in computing power will facilitate the employment of more complex algorithms. However, even assuming current processing capabilities, it is unlikely that the currently pursued approaches are ideal. In the research performed in Chapter III and Chapter IV in this thesis, there are many future research opportunities that have the potential to further the detection mission. Some of these ideas are detailed in this section.

The research in Chapter III, which again consisted of the implementation of the FPD algorithm, ultimately showed that correlation-based algorithms outperform point detection algorithms. However, the FPD produced significantly better results than the standard point detector, possibly indicating that analysis in the frequency domain could aid detection performance with other algorithms. A Fourier correlation algorithm has already been explored in earlier research [11] and a frame selection method based on the power present in the imaginary component of the Fourier transformed image data was briefly investigated for this work, but there are likely other variations of utilizing frequency information that have not been discovered yet that can further current detection algorithms.

The new frame selection algorithm developed in Chapter IV has a few research opportunities to verify and further improve its detection performance over a standard correlator. As outlined in this chapter, only a very limited amount of experimental data was available for testing. Because of the lack of collected image frames, the theoretical performance differences between the original and new frame selection algorithms seen in the simulated experiment were hardly observed in the experimental data tests. Both experiments substantiated evidence that the new frame selection algorithm outperformed the standard spatial correlator, but to confirm the performance difference between the new and original frame selection algorithms, more experimental data across different operation times and object SNRs should be examined. Furthermore, analyzing an optical system with lower readout noise could allow for more than 10 frames of short exposure data to be used during frame selection with limited noise-induced effects, along with increased viability of the algorithm in a traditional night collection scenario.

# Bibliography

[1] "The National Space Policy of the United States of America", *Federal Register*, Volume 85. No. 242 (2020).

[2] 116th Congress, "National Defense Authorization ACT for Fiscal Year 2020," *Public Law*, 2020.

[3] 111th Congress, "National Aeronautics and Space Administration Authorization Act of 2010," 2010.

[4] Public Law, *National Aeronatics and Space Act of 1958*. United States, 1958.

[5] T. Greicius and D. Brian, "A Near-Earth Asteroid Census," *National Aeronautics and Space Administration*, 2011. [Online]. Available: https://www.nasa.gov/mission_pages/WISE/multimedia/gallery/neowise/pia14734.html. [Accessed: 07-Sep-2020].

[6] 109th Congress, "National Aeronautics and Space Administration Authorization Act of 2005," 2005.

[7] Center for Near Earth Object Studies, "Discovery Statistics." [Online]. Available: https://cneos.jpl.nasa.gov/stats/totals.html. [Accessed: 10-Sep-2020].

[8] S. Hildreth A. and A. Arnold, "Threats to U.S. National Security Interests in Space: Orbital Debris Mitigation and Removal," 2014.

[9] National Aeronautics and Space Administration, "Orbital Debris Quarterly News," *Orbital Debris Q. News*, vol. 24, no. 2, p. 10, 2020.

[10] U.S. Air Force, "Ground-Based Electro-Optical Deep Space Surveillance," 2010. [Online]. Available: https://www.af.mil/About-Us/Fact-Sheets/Display/Article/104594/ground-based-electro-optical-deep-space-surveillance/. [Accessed: 10-Sep-2020].

[11] D. J. Becker, "Techniques for Improved Space Object Detection Performance from Ground-Based Telescope Systems Using Long and Short Exposure Images," *Def. Tech. Inf. Cent.*, 2018.

[12] N. Kaiser, "Pan-STARRS: a wide-field optical survey telescope array," in *Ground-based Telescopes*, 2004, doi: 10.1117/12.552472.

[13] The University of Arizona College of Science Lunar & Planetary Laboratory,

“Spacewatch.” [Online]. Available: https://spacewatch.lpl.arizona.edu/publications.

[14] “Orbital Debris Program Office.” [Online]. Available: https://orbitaldebris.jsc.nasa.gov/.

[15] B. Ianotta, “U.S. Satellite Destroyed in Space Collision,” 2009. [Online]. Available: https://www.space.com/5542-satellite-destroyed-space-collision.html.

[16] National Aeronautics and Space Administration, “Center for Near Earth Object Studies.” [Online]. Available: https://cneos.jpl.nasa.gov/.

[17] M. Hart, S. Jefferies, D. Hope, J. Nagy, and R. Swindle, “A Comprehensive Approach to High-Resolution Daylight Imaging for SSA,” in *Advanced Maui Optical and Space Surveillance Technologies Conference (AMOS)*, 2016.

[18] C. R. Michael and M. W. Byron, *Imaging Through Turbulence*. 2018.

[19] T. W. Lawrence, D. M. Goodman, E. M. Johansson, and J. P. Fitch, “Speckle imaging of satellites at the US Air Force Maui Optical Station,” *Appl. Opt.*, 1992, doi: 10.1364/ao.31.006307.

[20] S. Griffin, A. Whiting, S. Haar, and S. Williams, “Compliant Baffle for Large Telescope Daylight Imaging,” *Amostech*, pp. 1–5, 2014.

[21] R. Swindle, D. Hope, M. Hart, and S. Jefferies, “High resolution Imaging of Satellites in Daylight,” *AMOS Conf.*, 2018.

[22] N. Estell, D. Ma, and P. Seitzer, “Daylight imaging of LEO satellites using COTS hardware,” *AMOS Technol. Conf.*, no. September, pp. 17–20, 2019.

[23] M. Hart, D. A. Hope, J. Richey, and T. R. Swindle, “Image Restoration from Sodium Guide Star Observations in Daylight,” *AMOS Tech. Conf. 2019*, 2019.

[24] J. W. Goodman, “Introduction to Fourier Optics 3rd Edition,” *Roberts & Company Publishers*. 2005.

[25] T. J. Hardy, “Optical Theory Improvements to Space Domain Awareness,” 2016.

[26] J. C. Zingarelli, “Enhancing Ground Based Telescope Performance with Image Processing,” *Def. Tech. Inf. Cent.*, 2013.

[27] S. C. Pohlig, “An Algorithm for Detection of Moving Optical Targets,” *IEEE Trans. Aerosp. Electron. Syst.*, 1989, doi: 10.1109/7.18661.

[28] A. O’Dell, “Detecting Near-Earth Objects Using Cross-Correlation With A Point Spread Function,” Air Force Institute of Technology, 2009.

[29] H. E. M. Viggh, G. H. Stokes, F. C. Shelly, M. S. Blythe, and J. S. Stuart, “Applying electro-optical space surveillance technology to asteroid search and detection: The LINEAR program results,” in *Space 1998*, 1998, doi: 10.1061/40339(206)44.

[30] E. Bertinl, “SExtractor: Software for source extraction,” *Astron. Astrophys. Suppl. Ser.*, vol. 117, no. 2, pp. 393–404, 1996, doi: 10.1051/aas:1996164.

[31] J. W. Goodman, *Statistical Optics*, 1st ed. John Wiley & Sons, Inc., 1985.

[32] D. A. Hope, S. M. Jefferies, M. Hart, and J. G. Nagy, “High-Resolution Speckle Imaging through Strong Atmospheric Turbulence,” *Opt. Express*, 2016, doi: 10.1364/oe.24.012116.

[33] T. J. Hardy and S. C. Cain, “Characterizing Point Spread Function (PSF) fluctuations to improve Resident Space Object detection (RSO),” in *Sensors and Systems for Space Applications VIII*, 2015, doi: 10.1117/12.2177080.

[34] S. Cain, “Improved space object detection via scintillated short exposure image data,” in *Unconventional Imaging and Wavefront Sensing XII*, 2016, doi: 10.1117/12.2236963.

[35] J. Chris Zingarelli, E. Pearce, R. Lambour, T. Blake, C. J. R. Peterson, and S. Cain, “Improving the space surveillance telescope’s performance using multi-hypothesis testing,” *Astron. J.*, vol. 147, no. 5, 2014, doi: 10.1088/0004-6256/147/5/111.

[36] N. M. Law, C. D. Mackay, and J. E. Baldwin, “Lucky Imaging: High Angular Resolution Imaging in the Visible from the Ground,” *Astron. Astrophys.*, vol. 446, no. 2, pp. 739–745, 2005, doi: 10.1051/0004-6361:20053695.

[37] C. Mackay, “High-efficiency lucky imaging,” *Mon. Not. R. Astron. Soc.*, vol. 432, no. 1, pp. 702–710, 2013, doi: 10.1093/mnras/stt507.

[38] National Aeronautics and Space Administration, “Hubble Space Telescope.” [Online]. Available: https://www.nasa.gov/mission_pages/hubble/main/index.html.

[39] I. B. Putnam, “Atmospheric Impact on Long Pulse Laser Detection and Ranging (LADAR) Systems,” Air Force Institute of Technology, 2013.

[40] I. B. Putnam and S. C. Cain, “Modeling a Temporally Evolving Atmosphere with Zernike Polynomials,” *AMOS Tech. Conf.*, 2012.

[41] R. D. Richmond and S. C. Cain, *Direct-detection LADAR systems*. 2010.

[42] J. L. Nieto and E. Thouvenot, “Recentring and selection of short-exposure images with photon-counting detectors,” *Astonomy Astrophys.*, vol. 241, no. 2, pp. 663–672, 1991.

## REPORT DOCUMENTATION PAGE

*Form Approved*
*OMB No. 074-0188*

| | | |
|---|---|---|
| **1. REPORT DATE** *(DD-MM-YYYY)*<br>25-03-2021 | **2. REPORT TYPE**<br>Master's Thesis | **3. DATES COVERED** *(From – To)*<br>August 2019 – March 2021 |

| | |
|---|---|
| **TITLE AND SUBTITLE**<br>Supporting Space Domain Awareness Through the Development and Analysis of Space Object Detection Algorithms Employed by Ground-Based Telescopes | **5a. CONTRACT NUMBER** |
| | **5b. GRANT NUMBER** |
| | **5c. PROGRAM ELEMENT NUMBER** |
| **6. AUTHOR(S)**<br>Paw, Connor A., 2nd LT, USAF | **5d. PROJECT NUMBER** |
| | **5e. TASK NUMBER** |
| | **5f. WORK UNIT NUMBER** |

| | |
|---|---|
| **7. PERFORMING ORGANIZATION NAMES(S) AND ADDRESS(S)**<br>Air Force Institute of Technology<br>Graduate School of Engineering and Management (AFIT/ENG)<br>2950 Hobson Way, Building 640<br>WPAFB OH 45433-8865 | **8. PERFORMING ORGANIZATION REPORT NUMBER**<br>AFIT-ENG-MS-21-M-071 |
| **9. SPONSORING/MONITORING AGENCY NAME(S) AND ADDRESS(ES)**<br>Commander & Material Leader, Air Force Maui Optical and Supercomputing<br>Air Force Research Labs Det 15<br>Lt Col J. Chris Zingarelli, PhD<br>Telephone number (work): (808)-891-7701<br>Telephone number (cell): 571-386-8924<br>John.zingarelli@us.af.mil | **10. SPONSOR/MONITOR'S ACRONYM(S)**<br>**AFRL/RDSM**<br>**11. SPONSOR/MONITOR'S REPORT NUMBER(S)** |

**12. DISTRIBUTION/AVAILABILITY STATEMENT**
**DISTRUBTION STATEMENT A.** APPROVED FOR PUBLIC RELEASE; DISTRIBUTION UNLIMITED.

**13. SUPPLEMENTARY NOTES**

**14. ABSTRACT**
Detection algorithms are instrumental in maintaining space domain awareness, specifically in the observation, monitoring, and categorization of unknown space objects. State of the art detection algorithms utilize a matched filter or a spatial correlator on long exposure image data to make pixel-wise detection decisions. This thesis investigates the advantages and practical potential of two different post-processing detection algorithms that can be employed by ground-based telescopes. The first algorithm explored is based on a long exposure Fourier domain processing technique, while the second is centered around frame selection from a series of short exposure images. The results of the experiments performed in this thesis ultimately showed that the Fourier point detector algorithm did outperform a traditional point detector algorithm but had significantly lower probability of detection across all false alarm rates when compared to a spatial correlator algorithm over a series of test scenarios. The novel frame selection algorithm was found in the simulated experiment to outperform both the old frame selection algorithm and the spatial correlator in all testing environments at low false alarm rates. The experimental data results confirmed the increased performance of the new frame selection algorithm against its' counterparts.

**15. SUBJECT TERMS**
Space Domain Awareness, Object Detection, Ground-Based Telescope, Optics, Image Processing

| | | | | | |
|---|---|---|---|---|---|
| **16. SECURITY CLASSIFICATION OF:** | | | **17. LIMITATION OF ABSTRACT** | **18. NUMBER OF PAGES** | **19a. NAME OF RESPONSIBLE PERSON**<br>Dr. Stephen Cain, AFIT/ENG |
| **a. REPORT**<br>U | **b. ABSTRACT**<br>U | **c. THIS PAGE**<br>U | UU | 134 | **19b. TELEPHONE NUMBER** *(Include area code)*<br>(312)785-3636 Stephen.Cain@afit.edu |

**Standard Form 298 (Rev. 8-98)**
Prescribed by ANSI Std. Z39-18